UNIVERSITÀ DEGLI STUDI DI PADOVA

UNIVERSITY OF PADOVA

Department of Industrial Engineering DII

Master's Degree in Materials Engineering

Production and characterization of bainitic steels through additive manufacturing techniques

Supervisor: Prof. Dabalà Manuele

Co-supervisor: Ing. Franceschi Mattia

Co-supervisor: Ing. Yazdanpanah Arshad

Leone Davide 1241758

Academic year 2021/2022

CONTENTS

Abstract

Additive manufacturing is a relatively recent technology, developed in the last years of the last century, which has completely revolutionized the world of component design and manufacturing. Through the use of this production process, it has been possible to create products with much more complex geometries, allowing the achievement of very high performance. The products obtained are complex, light, and customized, ranging in different fields of application including automotive, aerospace, and biomedical. One of the best-known technologies used in additive manufacturing is Laser-Powder Bed Fusion (L-PBF), a process that uses a laser beam to precisely melt a bed of powder deposited in the melting chamber layer by layer. This technology allows the creation of complex geometries in a single production step and relatively quickly. Additive manufacturing, therefore, offers countless advantages from a design and performance point of view, accompanied however by some difficulties from the point of view of porosity and both internal and surface defects. The porosity, and consequently the final density of the piece, is considered one of the main issues on which to focus as it will affect the mechanical properties of materials made with the AM technique. It is, therefore, necessary to be able to optimize as much as possible the printing parameters used in the molding process, in such a way as to obtain a piece density similar to that obtained through a classic production process. In addition, AM can lead to the formation of defects due to differences in cooling during molding, differences in heat transfer, possible inhomogeneities in the composition due to decarburization, shrinkage, and formation as well as pores and internal cracks. Currently, even the surface quality of the components printed using L-PBF is not high enough to guarantee their use without finishing operations through final processing. The purpose of this work is precisely to characterize the printed samples and to optimize the printing parameters as much as possible, in order to obtain a final product as similar as possible to the bulk produced traditionally or to be able to improve its final performance, paving the way for future new applications for TRIP bainitic steel.

The first phase of work concerns the preparation of the samples made with the first set of parameters. The procedure can be summarized in polishing of 3 surface faces; photos at different magnifications using the optical microscope; cutting a slice of each sample 3 mm thick; incorporating and polishing with subsequent photos with the optical microscope. The images are then used to evaluate porosity using ImageJ and analysis of the data obtained with Origin.

Subsequently, micro-hardness tests were carried out, analyzing 66 cross-patterned impressions (33 vertical and 33 horizontal) on the cut face of each sample. The mean and the median were then obtained from the Vickers hardness values, to obtain a reference value for comparisons with bulk. During the measurement of the micro-hardnesses, variability was found in the measurements in different positions on the sample, due to the presence of pores and defects.

To complete the characterization of the samples, XRD analyzes were also performed; evaluation of the Melt Pools; SEM microstructural analysis of as-printed samples, and EDS and EBSD maps. The results obtained are consistent with the bibliography regarding the L-PBF process and with microstructure comparable to that found in traditional bulk with the same alloy composition.

Having obtained all the data regarding the printed samples, an austempering heat treatment was subsequently carried out at the isothermal transformation temperature of 325 ° C for 3 hours, in order to obtain bainite and verify its effective success. The results obtained are also consistent, showing a microstructural morphology comparable to that obtained on the bulk. Only randomly distributed areas with irregular shapes of untransformed ferrite islands were found, due to the decarburization that occurs during the laser molding phase.

The last phase of the work concerns the analysis of the printed samples with the new set of optimized parameters. The new parameters were chosen based on all the results and data obtained, making theoretical evaluations and mainly exploiting the trend that has been found between porosity and print energy density. The energy range between samples 1 and 7 was taken as a reference. Sample 7 has the highest density, but the surface was melted by excessive laser power. On the other hand, sample 1 has the highest density among those without a molten surface.

Riassunto

L'additive manufacturing è una tecnologia relativamente recente, sviluppatasi negli ultimi anni dello scorso secolo, la quale ha rivoluzionato completamente il mondo della progettazione e della realizzazione di componenti. Tramite l'utilizzo di questo processo produttivo è stato possibile realizzare prodotti con geometrie molto più complesse, permettendo il raggiungimento di prestazioni molto elevate. I prodotti ottenuti sono complessi, leggeri e personalizzati, spaziando su diversi campi di applicazione tra cui automotive, aerospaziale e biomedicale. Una delle più note tecnologie utilizzate nell'additive manufacturing è il Laser-Powder Bed Fusion (L-PBF), un processo che sfrutta un fascio laser per fondere con precisione un letto di polvere depositato nella camera di fusione strato per strato. Questa tecnologia permette la realizzazione di geometrie complesse in un unico step produttivo e in tempi relativamente rapidi. L'additive manufacturing perciò offre innumerevoli vantaggi dal punto di vista progettuale e prestazionale, accompagnati però da alcune difficoltà dal punto di vista di porosità e difetti sia interni che superficiali. La porosità, e di conseguenza la densità finale del pezzo, è considerata una delle principali questioni su cui porre l'attenzione in quanto andrà ad influenzare le proprietà meccaniche dei materiali realizzati con tecnica AM. È necessario, perciò, riuscire ad ottimizzare il più possibile i parametri di stampa utilizzati nel processo di stampaggio, in modo tale da ottenere un densità di pezzo simile a quella ottenuta tramite processo di produzione classico. Inoltre, l'AM può portare alla formazione di difetti dovuti a differenze di raffreddamento durante lo stampaggio, a differenze di trasferimento di calore, possibili disomogeneità nella composizione dovuta a decarburazione, ritiri e formazione oltre che di pori anche di cricche interne. Attualmente anche la qualità superficiale dei componenti stampati tramite L-PBF non è sufficientemente elevata da garantirne l'utilizzo senza operazioni di finitura mediante lavorazioni finali. Lo scopo di questo lavoro è appunto quello di caratterizzare i campioni stampati e di ottimizzare il più possibile i parametri di stampa, in modo da ottenere un prodotto finale il più possibile simile al bulk prodotto in maniere tradizionale, o riuscire anche a migliorarne le prestazioni finali, aprendo la strada a future nuove applicazioni per l'acciaio bainitico TRIP.

La prima fase di lavoro riguarda la preparazione dei campioni realizzati con il primo set di parametri. Il procedimento può essere riassunto in: lucidatura di 3 facce superficiali ; foto a diversi ingrandimenti utilizzando il microscopio ottico; taglio di una fetta di ogni campione di spessore 3 mm; inglobatura e lucidatura con successive foto con microscopio ottico. Le immagini vengono poi utilizzate per valutare la porosità tramite ImageJ e analisi dei dati ottenuti con Origin.

In seguito sono state effettuate delle prove di micro-durezza, analizzando 66 impronte con schema a croce (33 verticali e 33 orizzontali) sulla faccia tagliata di ogni campione. Dai valori di durezza Vickers è stato poi ricavata la media e la mediana, in modo tale da ottenere un valore di riferimento per i confronti con il bulk. Durante la misurazione delle micro-durezze è stata riscontrata una variabilità nelle misurazioni in diverse posizioni sul campione, a causa della presenza di pori e difetti.

Per completare la caratterizzazione dei campioni sono state effettuate anche analisi XRD; valutazione delle Melt Pools; analisi microstrutturale al SEM dei campioni as-printed e mappe EDS e EBSD. I risultati ottenuti sono coerenti con la bibliografia rigurdante il processo L-PBF e con microstruttura paragonabile a quella riscontrata nel bulk tradizionale con stessa composizione di lega.

Ottenuti tutti i dati riguardanti i campioni stampati, è stato successivamente svolto un trattamento termico di austempering alla temperatura di trasformazione isoterma di 325°C per 3 ore, in modo tale da ottenere bainite e verificarne l'effettiva riuscita. I risultati ottenuti sono anch'essi coerenti, mostrando una morfologia microstrutturale paragonabile a quella ottenuta sul bulk. Sono state riscontrate solo zone distribuite in maniera random con forme irregolari di isole di ferrite non trasformata, per via della decarburazione che avviene in fase di stampaggio laser.

L'ultima fase del lavoro rigurda l'analisi dei campioni stampati con il nuovo set di parametri ottimizzati. I nuovi parametri sono stati scelti sulla base di tutti i risultati e dati ottenuti, facendo valutazioni teoriche e sfruttando principalmente il trend che si è riscontrato tra porosità e densità energetica di stampa. È stato preso come riferimento il range di energia compreso tra il campione 1 e il 7. Il campione 7 ha la densità più elevata, ma la superficie è stata fusa dall'eccessiva potenza del laser. Invece, il campione 1 ha la densità più elevata tra quelli senza superfice fusa.

1 INTRODUCTION

1.1 BAINITE

Bainite is a steel phase that forms under a particular condition of cooling from austenitization temperature [1]. It is used as an isothermal transformation that leads to the formation of a microstructure of bainitic ferrite plates α separated by retained austenite γ, in form of film or blocky, and a small part of transformed martensite [1].

1.1.1 Transformation

The bainitic transformation mechanism is displacive, in which the distance between the atoms does not change, but there is only a modification in the crystalline lattice [1–3]. Bainitic transformation takes place with a paraequilibrium nucleation, where only C atoms diffuse, and by a displacive diffusionless growth [1–3]. Other alloy elements do not move, which maintains the chemical composition unchanged [1]. On a thermodynamical level must be respected the conditions of free energy variation of the system [3]:

$$\Delta G^{\gamma \to \alpha} < -G_{SB} \qquad (1.1)$$

$$\Delta G_m < G_N \qquad (1.2)$$

where, $\Delta G^{\gamma \to \alpha}$ is the free energy variation of the austenite transformation without chemical composition variation, and G_{SB} is the stored energy of bainite. ΔG_m is the maximum free energy change accompanying the nucleation under paraequilibrium conditions, and G_N defines the minimum free energy change necessary, for bainite nucleation.

It derives that the maximum temperature at which both the condition are respected, and bainite can nucleate and grow, is the so-called "Bainite Start Temperature Bs" (Figure 1.1) [3].

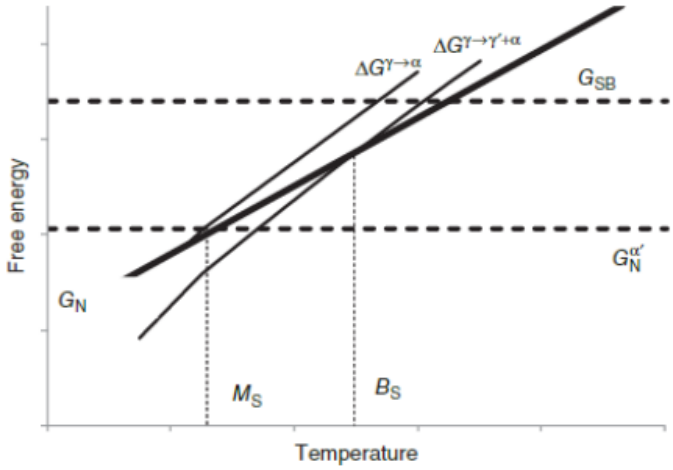

Figure 1.1 Thermodynamics-based graphical solution of B_s temperature [3].

Istantaneously, after the diffusionless growth of ferritic bainite subunits, carbon in excess, in the supersatured bainitic ferrite, is rejected, and it partition to enrich the surrounding austenite [3]. This behavior causes the reduction of martensite to start temperature (M_s) of the untransformed austenite, below the room temperature[3]. The growth process continues with the nucleation of successive subunits until the carbon content in the retained austenite reaches a value delimitated by T_0 curve ([C] = 0,5-1,5% wt), at which the free energy of bainitic ferrite and austenite becomes equal, therefore the reaction stops [3]. The transformation stops due to the thermodynamical impossibility for austenite to transform into bainite, and therefore bainitic transformation is called as "incomplete reaction phenomenon"[3]. This phenomenon is condensate into the concept of T_0 curve, which represents locus of points in a temperature vs [%C] graph, where austenite and ferrite with the same chemical composition have the same free energy [1–3]. Therefore, bainite should form at a temperature below this curve (Figure 1.2), at a fixed isothermal holding temperature, until austenite carbon content reach the level predicated by the curve [1].

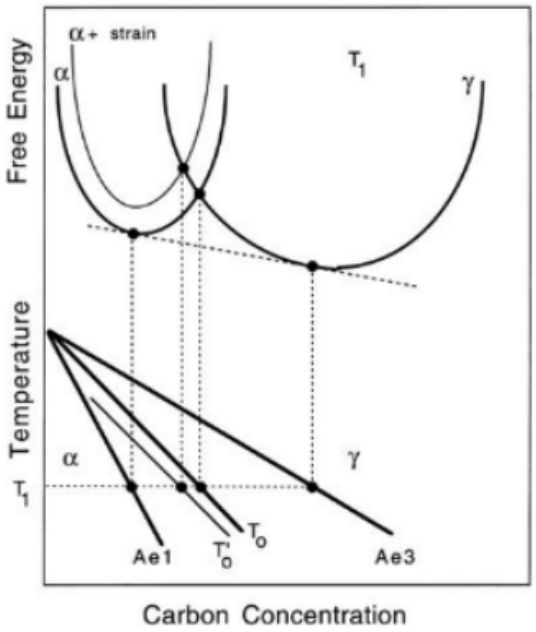

Figure 1.2 Illustration of the curve T_0 in a diagram Temperature vs [C%] [1].

Moreover, after the formation of a certain amount of bainitic ferrite, this will bind and stick the austenite, which will not be able to deform and transform [1]. There is no theoretical limit of temperature at which bainitic transformation could take place [1], therefore, the rate at which bainite forms, depends on free energy changes, meaning that transformation drastically slows down when the transformation temperature is decreased [1]. Hence, this explains why, for high carbon steel, at very low temperature the reaction took days in order to reach completion [4].

1.1.2 Bainitic Microstructure

Bainitic microstructure is characterized by a high level of complexity. It has unique forms due to the atomic mechanisms which lead the transformation itself. The structure has two predominant phases: the main phase, bainitic ferrite plates (αb), whose fraction increases with a decrease of transformation temperature; and a secondary phase, retained austenite (γ) [3]. It is also possible to find the third phase of martensite, forming when the carbon content enrichment is not sufficient to lower Ms below room temperature [3]. Austenite is divided into two different morphologies: a thin film (<100 nm) between ferritic plates, and a polygonal block (100-1000 nm) between the bainitic shaves (Figure 1.3) [5].

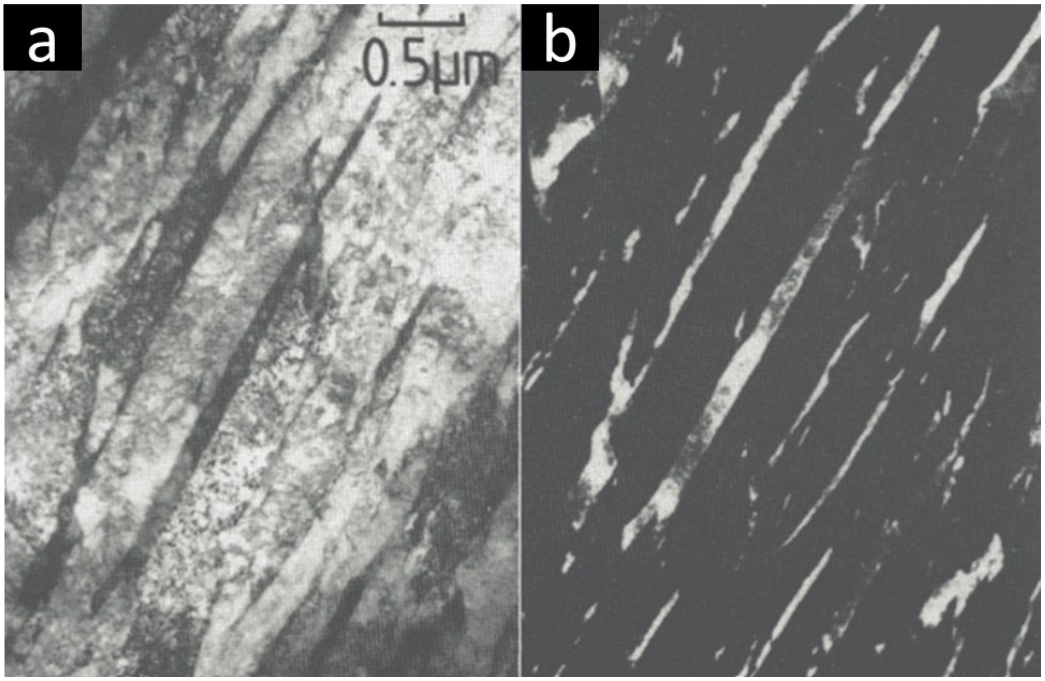

Figure 1.3 Fe-0,22C-3,00Mn-2,03Si; a) bainite dark phase, austenite bright phase; b) bainite bright phase, austenite dark phase; isothermal transformation at 340°C [4].

The nature of this transformation is displacive, causing shape deformation [3]. There is not only a variation in the crystal lattice but there is also a deformation [3]. The high magnitude of these deformations creates thin plates to minimize the deformation energy [1,3]. Other observation showed that there is a plastic relaxation of austenite surrounding the bainitic phase [3]. During this process, defected are introduced, and they can become obstacle to the austenite-ferritic interface movement [1,3]. Furthermore, another source of resistance to advancement is given by the austenite strength [1,3] that increases as the temperature decreases [6,7]. All of this can promote the formation of dislocations around the ferritic bainite during the growth, acting as a place in which cementite can precipitate from the enriched austenite [3]. The precipitation of carbides (cementite) from austenite to ferrite can determine the formation of two kinds of bainite: upper bainite and lower bainite [1,8]. In upper bainite, the cementite particles are oriented in the same way as the bainitic ferrite plates [1,8], and forms around the ferritic plates, and it is generally found at a high transformation temperature [1,8]. Instead, in lower bainite, there is a finer dispersion of thinner carbides [1,8], that are oriented with an angle of 55/60° respect to the growth direction of the bainitic plates, and they are formed at a lower transformation temperature [1,3,8]. Bainitic ferrite plate thickness depends on the resistance of austenite at the transformation temperature, free energy changes in the transformation, and dislocation density [3]. A high dislocated austenite with a high resistance or mortice force can create thinner structures (Figure 1.4) [3]. These variables, which can act on the ferrite dimension, are affected by transformation temperature, increasing if this decreases, creating a thinner structure [3].

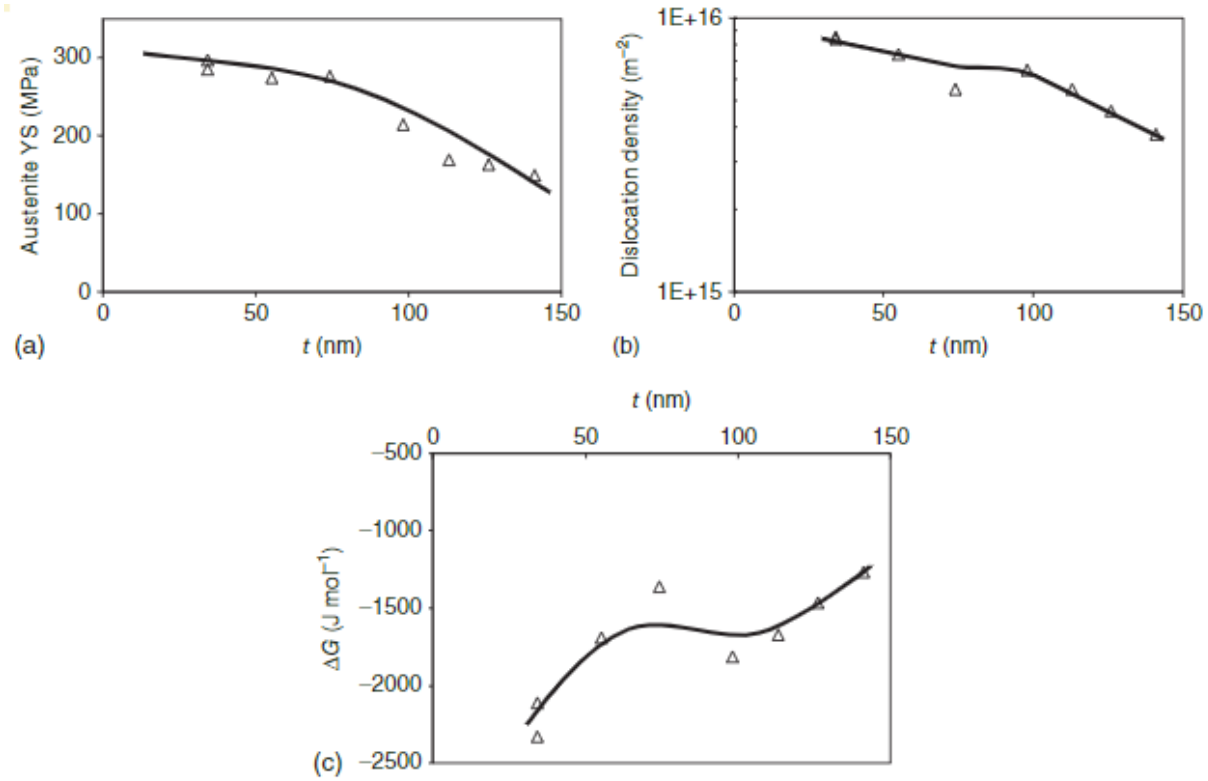

Figure 1.4 Relation between the bainitic ferrite plate thickness and a) YS of austenite, b) dislocation density, and c) free energy change for bainite nucleation [3].

Figure 1.5 shows the typical micrography of bainitic steel, in which it is possible to distinguish the two phases, bainitic ferrite and austenite [3].

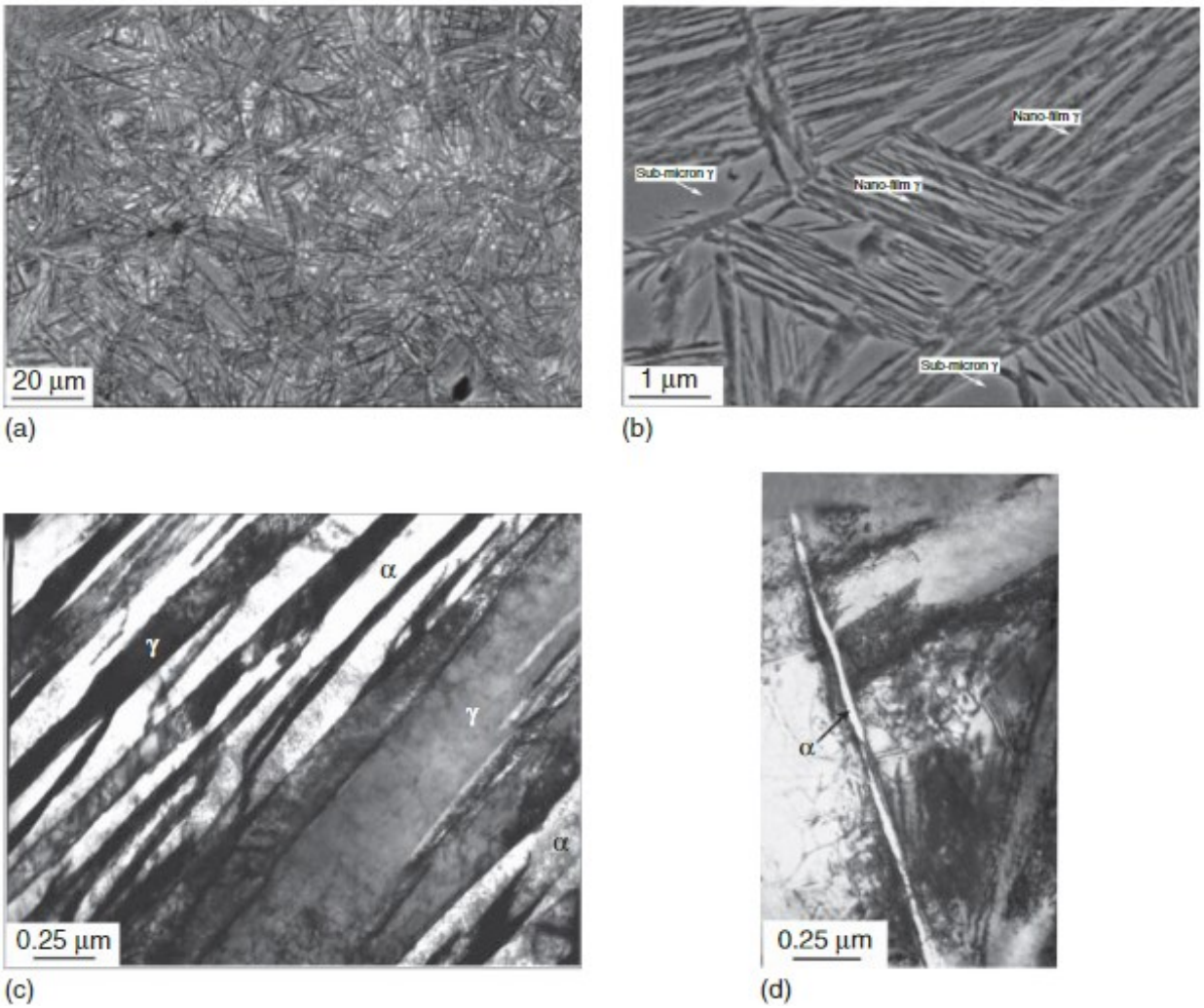

Figure 1.5 typical bainite microstructures at different magnifications [3].

Figure 1.5c, and b show a high number of dislocations in both ferrite and retained austenite [3]. Instead, very representative is the case in Figure 1.5d, which corresponds to the primary transformation stage, showing a single plate of ferritic bainite that grows into austenite [3]. There are plastic relaxations with the generation of austenite dislocation in contact with bainitic ferrite, and these increase as the temperature decreases[3]. Furthermore, it happens a progressive increase in dislocation density due to the plastic deformation in the area surrounding austenite to allow deformative transformation when the growth goes ahead [3].

The presence of defects and dislocations plays an important role in carbon redistribution during the transformation process [2]. The dislocations, which are formed during the plastic relaxation, can trap carbon atoms and hind the decarburization of supersaturated bainitic ferrite [2]. It is expected that carbon trapping at the crystal defects can bind, and so hind the carbon atoms diffusion out of ferrite lattice, changing the carbide precipitation sequence during low-temperature bainite formation [3,9]. It is also definitive proof that the excess carbon in bainitic ferrite (0,16-0,20% C) is found not only at

the defects but also in the solid solution [1,3,9]. A concrete explanation for this capability comes from the fact that it becomes tetragonal due to the presence of C [1,3,9]. The carbon causes a modification in the equilibrium between austenite and ferrite BCC (body-centered cubic)[3,9]. The carbon solubility in tetragonal ferrite in equilibrium with austenite is higher than that for cubic ferrite [3]. Therefore, it is possible that the ferrite symmetry change can explain this excess of carbon into ferritic bainite [3,9]. Instead, the carbon amount in austenite, distribution is heterogeneous, and it is highly correlated to the thickness of the austenite region: the smaller austenite, the bigger is carbon concentration [3,9].

1.1.3 Alloy elements

There are alloy elements that have a very precise role in the transformation dynamic of austenite in bainite.

- *Silicon (Si):* an amount bigger than 1,5% can hind cementite precipitation from austenite [10]. During bainitic transformation, usually, there is carbides precipitation from austenite to ferrite [10]. Silicon exhibits a low solubility, but it is trapped in the cementite lattice due to the displacive mechanism of cementite growth [10]. Its mobility is reduced drastically lowering the free energy change accompanying the reaction and hence retards precipitation [10]. Moreover, silicon added in a high amount can increase the austenite strength before the bainitic transformation, allowing the formation of a more refined microstructure [10]. The obtained microstructure is called "carbide-free bainite", which is a mix of ferritic bainite and enriched retained austenite [10,11], that will be studied in this manuscript.
- *Carbon (C):* carbon atoms stuck into austenite after transformation do not fall as cementite, and they stabilized the austenite at room temperature [11].
- *Manganese (Mn):* decreases free energy change of austenite-bainite transformation, increasing the reaction rate [11]. It also stabilizes austenite.
- *Chrome (Cr):* this element is adding to improve the corrosion resistance of the steel forming a strong oxide layer. In addition, chromium stabilizes the ferrite phase and improves the strength of the steel by forming carbides [12]. However, it retards and restrictis the temperature range for bainite formation.
- *Molibdenum (Mo):* expands the carbon region inside the austenite phase by increasing the diffusion activation energy of carbon, and this condition stops the carbon diffusion, delaying the transformation [12]. The bainite transformation is slowed down.

- *Boron (B):* increases the hardenability and alters the cooling conditions related to microstructural formation in steels [12].

1.1.4 Heat treatment

The heat treatments necessary to obtain a bainitic microstrucutre consists of 2 steps: *austenitization* at a temperature above A_{c3}, followed by rapid cooling at a temperature above M_s, and a subsequent *isothermal transformation*, where the material is held for a sufficient time to obtain the maximum value of volume fraction of bainite [1,5,13]. The treatment temperature has a big influence on the starting microstructural dimension and nature, affecting the volume fractions of the steel phases, as reported in Table 1.1 [5,13].

Alloy, wt-%	**Isothermal transformation temperature, °C**	V_b	V_γ	$V_{\gamma-f}$	$V_{\gamma-B}$	$V_{x'}$	X_γ, wt-%	**Hardness, HV**
Fe-0.43C-3.00Mn-2.02Si	295	0.68	0.22	0.11	0.11	0.10	0.92	447
Fe-0.43C-3.00Mn-2.02Si	360	0.42	0.27	0.06	0.21	0.31	0.79	430

Table 1.1 Volume fraction of different alloy steels related to the different isothermal transformation temperatures [5].

An increment of bainite transformation temperature leads to a coarser microstructure, decreasing the volume fraction of bainite, compared to a lower transformation temperature (Figure 1.6) [13].

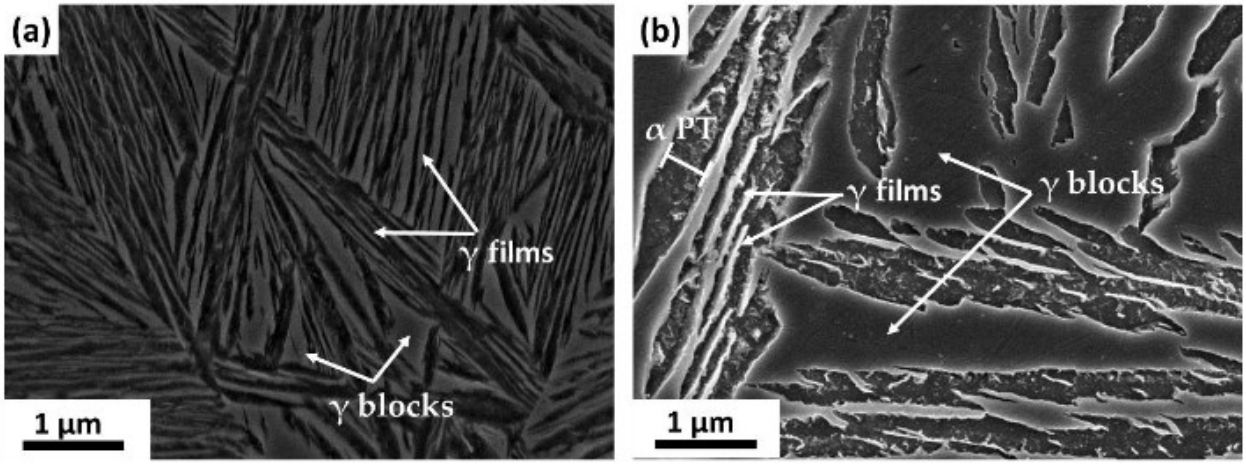

Figure 1.6 SE-SEM (secondary-electron scanning electron micrographs) of two nanostructured bainite of the same steel, treated at a) 250°C and b) 350°C. (γ) austenite and (α) ferrite [13].

The average value of volume-weight of ferritic bainite crystals dimension normally increases by several nanometres with the temperature increment, also decreasing defects density in the microstructure[13]. Instead, at lower temperatures, the microstructure becomes thinner and with a bigger dislocation number [13]. This should be proof of different amounts of carbon into ferrite at different transformation temperatures [13].

Increasing the bainitic transformation temperature it is possible to obtain a carbon content reduction in the solid solution of bainitic ferrite [13]. The ferrite tetragonality seems to be stronger with a decrease in temperature, with consequent rejection of C from ferrite, enriching the surrounding austenite [13]. Theoretically (T_0 curve) the carbon content in austenite should change with isothermal transformation temperature as well as before. Moreover, at the same time, temperature also affects the transformation rate, increasing it by a higher value. Therefore, following the previous consideration, the carbon amount in reteined austenite is higher with a higher temperature because, at the same transformation time (relatively short), the transformation goes ahead more rapidly, enriching the γ phase very fast [3,5,10].

At the beginning of the transformation bainite nucleates at the austenite grain boundaries[1]. An acceleration of transformation is allowed by the increment of nucleation sites, which is achieved with grain refinement[1,2,5]. This is possible by holding austenitization temperature at a lower value or introducing alloy elements that can act on austenite grain limiting their dimension through stable precipitates formation at high temperature [1,2,5]. However, depending on steel composition and on the isothermal transformation temperature the effect of different prior austenite grain size can differ of being dependent on the size of the grains itself [14–16]. Another approach to increase the density of nucleation sites for bainitic transformation is starting from deformed austenite [3]. In addition, the

generated defects such as dislocations can act as nucleation sites [3]. The problem is derived from the displacive transformation of bainite because the whole process can be delayed or stuck due to the phenomenon of mechanical stabilization[3]. In this mechanism, the growth of bainite is delayed by the deformation debris in the austenite [3]. Heterogeneous nucleation becomes more frequent as defects are introduced into austenite, so their growth through a displacive mechanism is blocked when the interface encounters dislocations [3]. Therefore, deformed austenite transforms into more refined bainite in a lower quantity compared to undeformed austenite [3]. Nevertheless, when the strain in the austenite is increased beyond an undefined critical value, the greater nucleation compensates for the hindrance to growth and the volume fraction of transformation achieves a similar level to that of undeformed austenite [3].

1.1.5 Mechanical properties

Strength

Considering the whole microstructure, the yield strength is mainly controlled by the amount and dimension of bainitic ferrite, and by the ratio between bainitic ferrite volume fraction and plate thickness (Figure 1.7) [13].

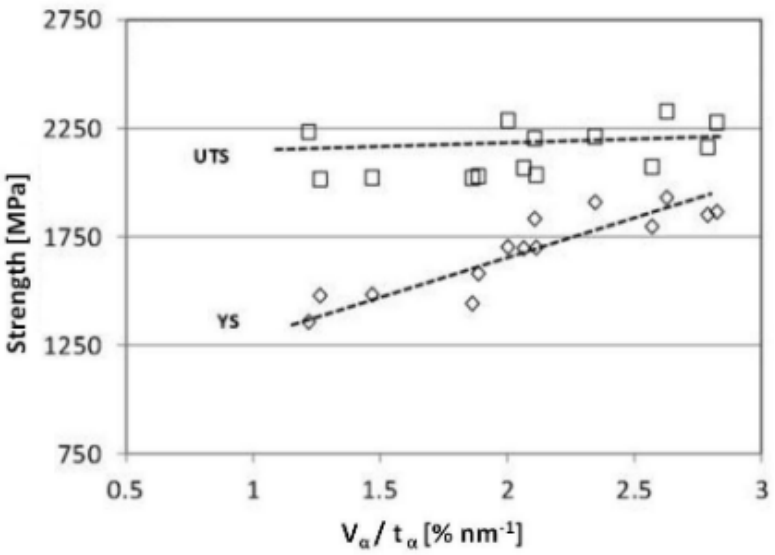

Figure 1.7 Yield strength of different nanostructured bainite vs ratio of volume fraction and thickness [9].

The higher the volume fraction of thinner bainitic ferrite, and higher the yield strength (YS) and the value of ultimate tensile strength (UTS), even if the last one does not change significantly. This suggests that bainitic ferrite is the hardest phase, while retained austenite is the softest one [13]. The parameter which mainly influences the direct and indirect strength in bainitic ferrite is the carbon amount. Higher is carbon content, and higher is the mechanical strength. Another important parameter

that acts on the strength is the dislocation density, from which there is a direct dependence on the carbon presence in ferrite (Figure 1.8)[17].

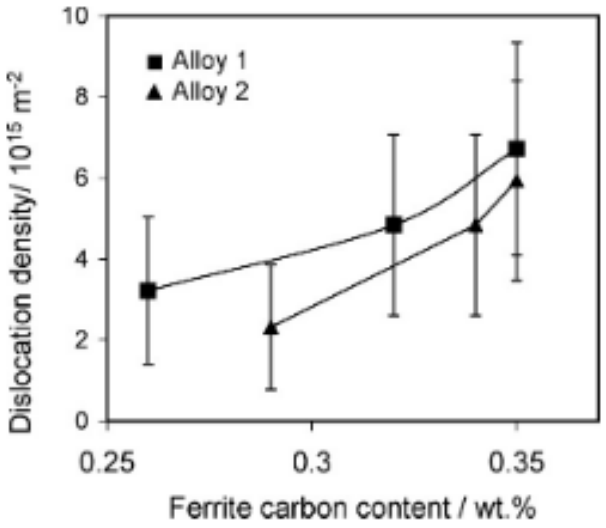

Figure 1.8 Relation between ferrite dislocation density and its carbon content [10].

All of this can lead to the observation that a bainitic ferrite microstructure obtained by heat treatment at low temperature, and so with thinner plates, higher dislocation, and higher carbon amount, can be the best in terms of strength (Table 1.2).

Heat treatment	**0,2% proof stress, MPa**
Isothermally transformed at 260°C for 60 min	1475
Isothermally transformed at 340°C for 60 min	1350

Table 1.2 correlation between different heat treatment temperatures and tensile test results [5].

The bainite stress-strain curve (figure 1.9) shows a continuous yield, as conceivable by a microstructure with unlocked dislocation introduced by the plastic accommodation of the shape change [3].

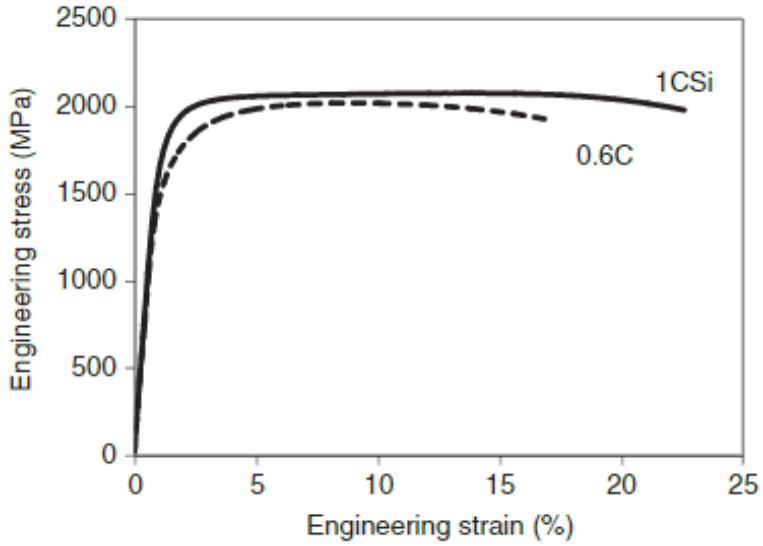

Figure 1.9 Engineering stress-strain curves at room temperature [3].

The amount of carbon in ferrite is in excess, but a major part of dislocation remains unlocked [3]. Although there are several obstacles to dislocation movement (solute atoms, boundaries, and thin film of retained austenite), which can block the plastic deformation, the biggest part of these is not uniformly distributed, so the dislocation can penetrate easily these obstacles [3]. Another reason that leads to continuous deformation, as shown in Figure 1.9, is due to the retained austenite, which is the softest phase in the microstructure [3]. Firstly, plastic deformation is concentrated in the softest phase, while the hardest phase starts to deform when the deformation is enough to transfer the load to the second phase [3].

Therefore, it is established that the main operative strengthening mechanisms contributing to the strength of carbide-free bainitic steels are: plate thickness, dislocation density, and carbon excess in solid solution [3]. Ferrite represents the strongest and dominant phase, giving the best contribution to the mechanical strength of the steel. Instead, austenite can affect the strength by transforming into martensite during the load action by the TRIP (Transformation Induced Plasticity) effect [3].

Ductility

Ductility and strength are rivalling properties because it is very difficult to increase the stress level brought by a material, without decreasing the strength to localize deformation [13]. The ductility is controlled by the volume fraction of retained austenite, which can increase this property thanks to transformation into martensite by the TRIP effect. The transformation must be controlled, controlling the microstructure, to maximize the effect. One important parameter is the amount of retained austenite which can affect the efficiency of the TRIP effect on the ductility of bainitic structure [11]. The retained austenite fraction evolution with the plastic deformation ε follows this law [13]:

$$Ln(VF^0{}_\gamma) - Ln(VF_\gamma) = K\varepsilon \quad (1.3)$$

Where $VF^0{}_\gamma$ is the volume fraction of austenite without deformation, while VF_γ is the volume fraction of austenite at deformation ε, and K is the parameter that depends on material and treatment temperature, which reflects the retained austenite stability: larger is the value and bigger is the destabilized austenite for a particular deformation [13].

The variation of elongation is based on the K parameter (Figure 1.10), which value depends on the treatment temperature (Figure 1.11) [13]. Higher temperatures slow down the martensite transformation.

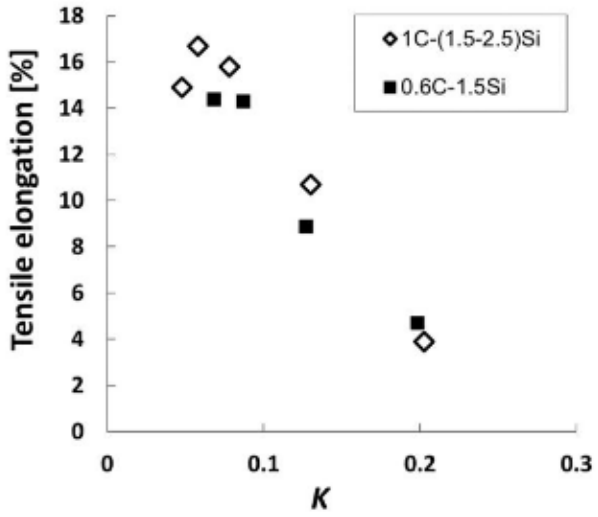

Figure 1.10 Variation of tensile elongation in comparison to K value [9].

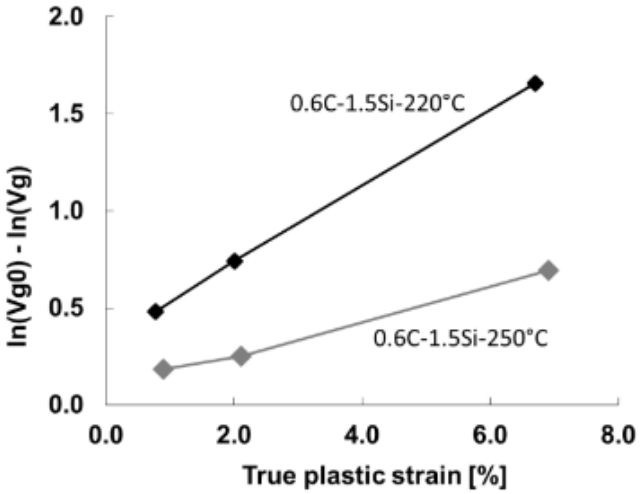

Figure 1.11 Influence of heat treatment temperature on the evolution of the content of transformed retained austenite. K is the slope of the lines [9].

The same behavior is in Figure 1.12 where the steel with higher heat treatment shows almost no martensitic transformation until 10% of elongation, while the sample treated at 200°C reached fracture at a deformation of 2% [13].

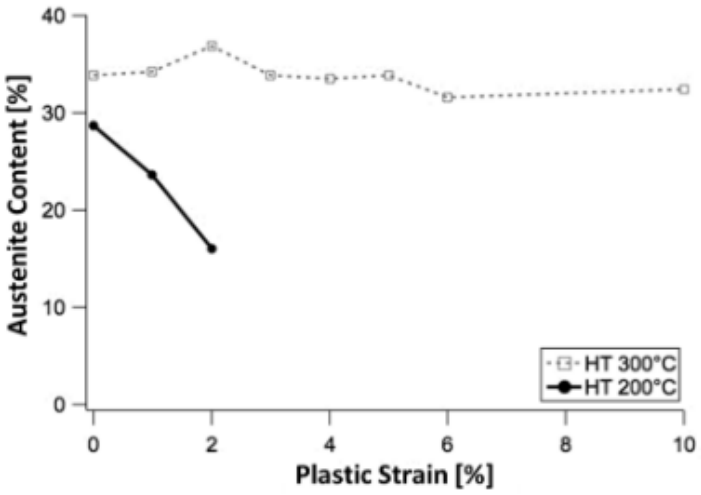

Figure 1.12 evolution of austenite content vs plastic strain of two steels treated at 200°C and 300°C [13].

Better performances in terms of ductility can be found in microstructures treated at higher temperatures, decreasing the initial work hardening process[13]. Instead, heat treatments at lower temperatures increase the work hardening rate, worsening the ductility[13]. Moreover, steels with high ductility show a higher damage resistance[13]. The film of retained austenite is one of the main reasons for this behavior. The nano-laminate morphology is perfect for blocking the cracks' movements, enhancing the material strength [13].

However, a large amount of unstable austenite without opportune carbon enrichment or morphology is not appropriate in terms of total elongation [13]. Higher is the stable austenite and lower is the mechanically induced martensitic transformation, leading to a more beneficial effect [13]. The reduction of the mechanical difference between austenite and bainitic ferrite seems to be the reason behind the better performance of samples treated at higher temperatures [13]. This phenomenon is because by increasing the temperature, there is a faster increase of the carbon content in austenite, increasing the strength, and minimizing the differences between the phases [13].

Hardness

The softer phase of the bainitic microstructure is the retained austenite, which controls the hardness of the alloy [3]. To improve the hardness of the bainitic microstructure, a reduction of the effective size of the grains, with the absence of a hard fragile phase such as the cementite and martensite with a high C content, is the most effective way to avoid degradation of hardness properties [3,5,13]. Stability must also be considered mechanics of austenite present in the microstructure because the

transformation into martensite would lead to a worsening of hardness [3]. The different morphologies of austenite, in a block and thin film, exhibit different stability, where the smaller region has a lower nucleation potential for transformation into martensite, requiring a greater activation force [3,13]. For these reasons the γ phase with block morphology is more willing to transform due to the TRIP effect, and its presence should be minimized (Table 1.1)[3].

Bainite is a microstructure composed of packages of parallel plates. The good hardness of this microstructure may be related to the high density of the high-angle boundaries that these microstructures present [3]. These boundaries act as obstacles to the propagation of flaking cracks, forcing the cracks to change the plane of propagation [3]. Low border angles between these packets would not guarantee an effective obstacle [3,13].

1.1.6 TRIP effect

The TRIP, "transformation induced plasticity", is a phenomenon that through a variety of shapes and volumes, induces the transformation of austenite into martensite, which generates local plasticity in the surrounding ferrite grains [1]. The efficiency of the martensitic transformation as a deformation mechanism plays a major role in the mechanical response of the alloy. Transformation involves the relaxation of local stress concentration and extra hardening through two sources: a progressive increase in the volume fraction of the hard phase (martensite) and additional plastic deformation due to the distortion of transformation [13]. To take full advantage of this effect, the mechanical stability of austenite, which is its ability to transform into martensite under deformation, must be moderate. In steels containing austenite with low mechanical stability, distortion-induced transformation occurs in the preliminary stages of deformation, generating little or almost no benefit from hardening [3]. If instead, austenite became mechanically more stable, transforming to a higher deformation, the associated hardening would greatly increase the resistance to necking and fracture [3,17]. However, if austenite were highly stable, the presence of high quantities of austenite during pinching would not guarantee a correct TRIP effect[17]. The transformation of austenite in martensite involves the coordinated movement of atoms, which would become impossible when the defect density reaches a sufficiently high value high, and dislocations in the microstructure can thus lead to stabilization mechanics of austenite preventing transformation [3,13,17].

1.2 MARTENSITE

Martensite in steels is a hard, brittle phase of steel at room temperature obtained after a process called martensitic transformation[8,18]. It is a solid solution enriched in carbon in an interstitial position in Fe (α) lattice, creating a body-centered tetragonal lattice (BCT)[8,18].

1.2.1 Transformation

The martensitic transformation happens almost instantly due to the a-diffusional phenomena of carbon and iron [8,18]. It is formed by rapid cooling from the austenite field and there is a coordinated movement of atoms without modifying the beginning austenite composition (paraequilibrium) [8]. The martensitic reaction begins during cooling when the alloy reaches the martensite start temperature (Ms) and the austenite becomes unstable Figure 1.13) [8,18].

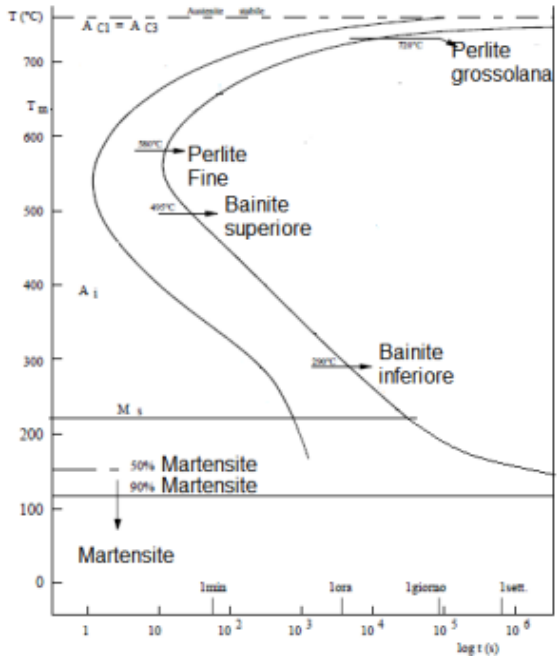

Figure 1.13 CCT diagram eutectoid steel.

As the phase diagram shows (Figure 1.14), the martensitic start temperature depends on the carbon content as expressed by the dotted line [18]. There is a decrease in the starting temperature when the carbon content is increased.

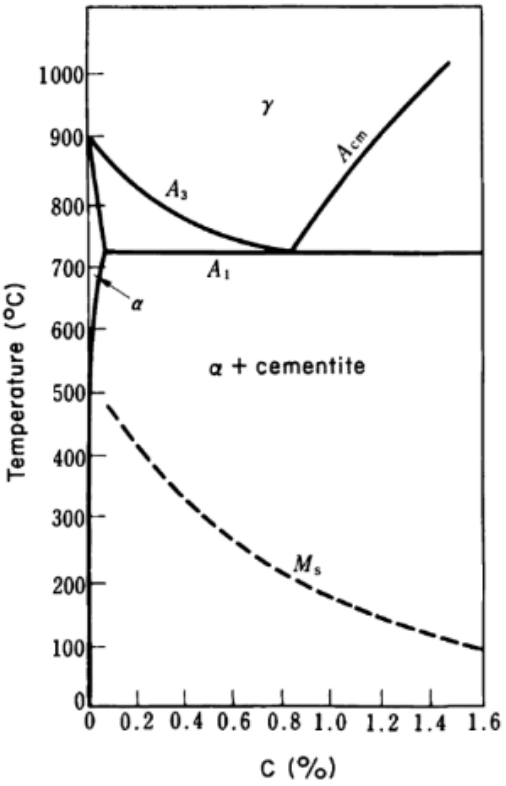

Figure 1.14 Fe-C diagram shows the correlation between M_s and carbon content

The solid solution of ferrite α has a BCC lattice where the carbon atoms occupying randomly the interstitial sites between the iron atoms (Figure 1.15) [18]. The α phase is an interstitial solid solution of iron and carbon [8,18]. The γ phase (austenite) is an interstitial solid solution of iron and carbon, but with an FCC lattice [8,18]. In addition, these two configurations have different carbon solubility [18].

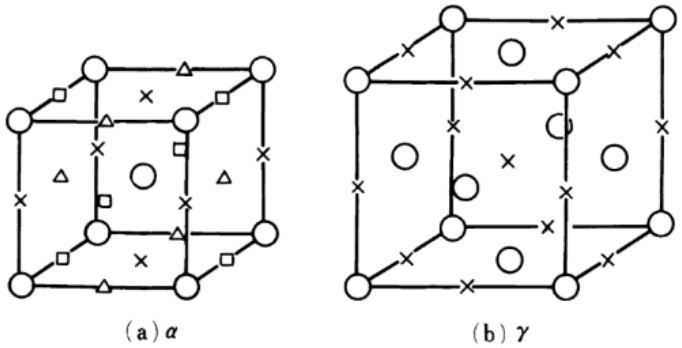

Figure 1.15 Units cell of: a) ferrite and b) austenite. O, Fe; Δ, X, □, avaible position for C atoms [18].

The crystal structure of martensite is obtained by quenching the γ phase, reaching a body-centered tetragonal (BCT) lattice, an α lattice with one of the cubic axes elongated as shown in Figure 1.16 [18]. The symbol α' is used to denote a martensitic structure derived from the α phase [18].

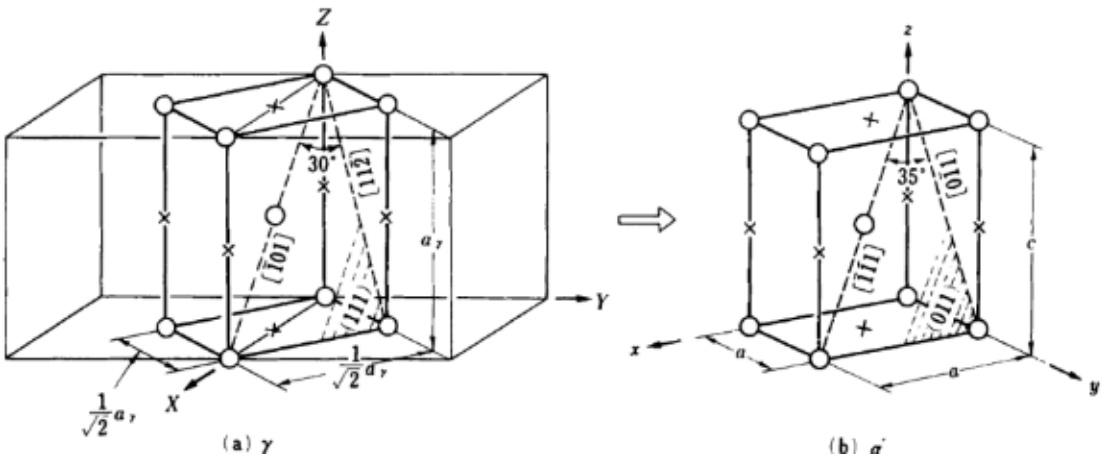

Figure 1.16 Transformation from γ to α′ [18].

The structure observed under the microscope shows only two phases: α' and retained γ[18]. Therefore, there is no chemical decomposition during the martensitic transformation, and most parts of austenite transform diffusionlessly to α', and the compositions are unchanged [18]. In addition, it is necessary to have a driving force for the transformation to take place[18]. This energy is given by the different free energies of α' and γ, where the free energy of martensite must be lower[18]. The transformation cannot take place until the temperature is not below T_0, which corresponds to a value of $\Delta E = 0$ between austenite and martensite of the same composition (Figure 1.17)[18].

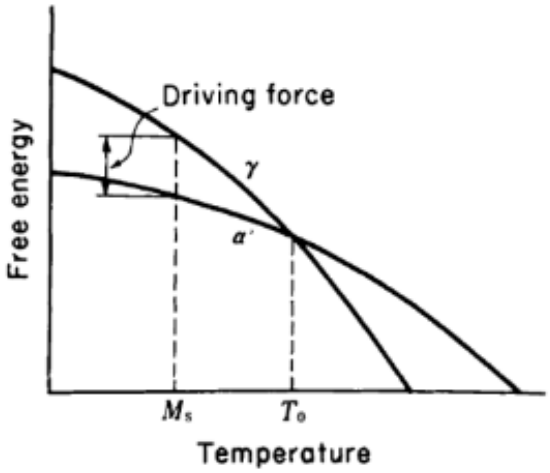

Figure 1.17 variation of free energy of austenite and martensite[18].

1.2.2 Microstructure

The martensite can have two different morphologies: lenticular or massive (Figure 1.18) [8]. These are addicted to the transformation temperature, where a lower temperature corresponds to a more lenticular structure [8]. This morphology is characteristic of steels with a high content of carbon ($C \geq 0.6\%$) because increasing the amount of C, decreases the M_s temperature [8]. Instead, massive

morphology does not exist above 1% of C, and in the range between 0.6 and 1% of carbon, it is possible to have both [8].

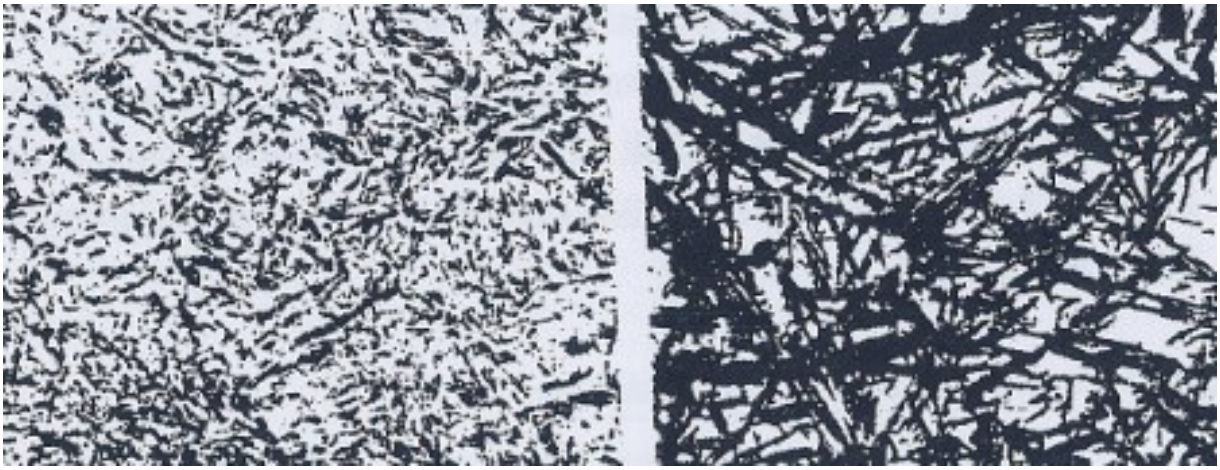

Figure 1.18 TEM pictures of martensite microstructure: on the left, massive; on the right, lenticular [8].

The massive martensite has a complex microstructure composed of plates of several sizes facing on the long face [8]. It has a higher dislocation density than the lenticular, creating fewer distortions and decreasing the fragility of the material [8]. The lenticular martensite has lamellae randomly oriented, giving an acicular aspect to the microstructure[8]. Moreover, between the martensite needles remain retained austenite[8].

1.3 L-PBF

Laser-Powder Bed Fusion is an AM technology in which thermal energy supplied by a laser is used to fuse materials by melting deposited on a platform [19–21]. The laser beam is directed on a bed of powder which is melted and subsequently dropped and recoated by a roller or blade distributing a new layer of material to do a new fusion of the next layer (Figure 1.19) [21].

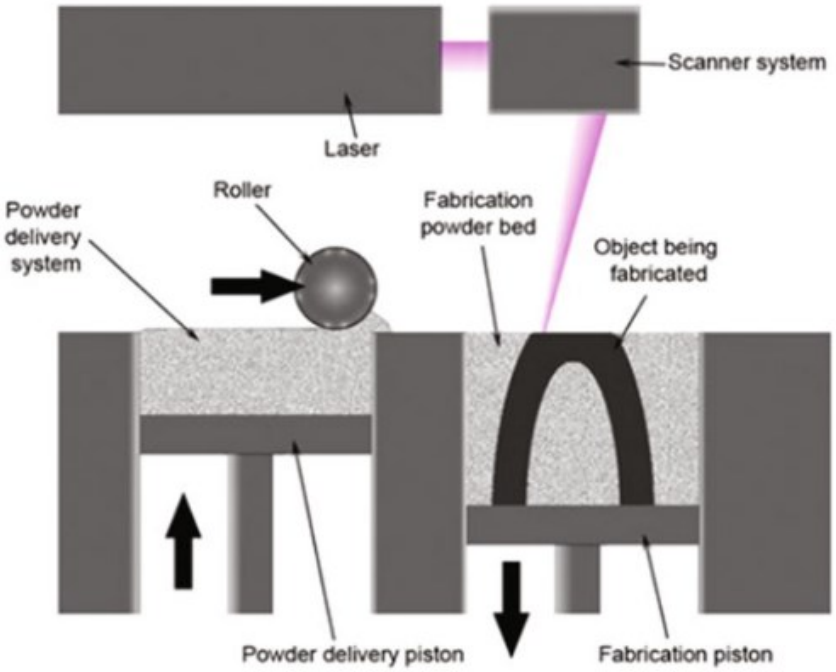

Figure 1.19 Laser Beam Powder Bad Fusion system [21].

PBF processes using laser beams (L-PBF) are widely referred to in the literature by different names based on the printing strategy [19,21]. Direct Metal Laser Sintering (DMLS), Selective Laser Melting (SLM), or Selective Laser Sintering (SLS). A PBF process that uses an electron beam, instead of a laser, is known as EBM (Electron Beam Melting) [19,21].

Selective Laser Melting is a technique in additive manufacturing that is different from the other methods and is based on the deposit and fusion way [21]. The powder is melted by thermal energy given by the laser, and the sequences of deposition and fusion happen in two different moments [19,21]. This is the explanation of the term "Selective". The system does not require a vacuum chamber, but it is used an inert gas to avoid powder and parts oxidations [19]. The laser direction is controlled by several optics, allowing rapid and precise control of the laser beam [19]. SLM system uses a finer powder distribution and a smaller thickness of the layers than the EBM system, therefore it results in a finer resolution of manufactured features [19].

1.3.1 Advantages / Disadvantages

The use of this technology has changed the way to realize a component and also the process in the primary stages. There are several advantages that the PBF process has brought to the engineering world:

- *STL file simplicity.* A wide range of CAD software can be used to generate STL files. It is possible to edit and easily fix the file for 3D printing [21]. The build volume can be improved efficiently by orienting and duplicating the STL file[21]. If it is required, it is possible to add a support structure design depending on the geometry of the piece to avoid warp or distortions [21].
- *Complex Structures.* This is a main advantage because there are no limitations on the design part of a component [21]. PBF can fabricate unique metal part shapes and more particular than the conventional process [21]. For example, it is possible to realize a rib structure inside a tool to reduce weight [21]. There is freedom from the constraints of conventional fabricated processes.
- *Limited material waste and consumption.* Complex geometry can minimize the use of metal, optimize mechanical performance, extend functionality and avoid the waste of material[21].
- *Multiple instances in one build cycle.* It is possible to produce a wide number of the same component in one build cycle, improving the process and saving time[21].
- *Rapid Prototype Time to market.* It allows for quick produce a prototype of a component[21].

These are the main advantages of a PBF process. However, in the AM methods, process complexity remains a critical issue. There are still several problems with the material and the production method that lead to complexity which influences a lot the use of PBF [21]. The main disadvantages are:

- *Distortion and Cracking.* During the cooling phase, the shrinkages can generate distortions and cracks due to the gradient of solidification [21].
- *Cost of Powder Material.* The costs of powder production are very high, especially powder with high purity, chemically clean, and consistent shapes and sizes [21].
- *Slow Deposition Rate.* This is a limitation due to the high time required to spread and recoat a layer of powder. This condition is addicted to the size of the part and the size of the build volume [21].
- *Porosity, voids, and defects.* These kinds of defects are due to unfused regions of powder formed by process disturbance or inadequate parameters or entrapped gas during fusion and solidification [21].
- *Part Size Limit.* It is due to the built volume available for printing [21].

1.3.2 Process Parameters

L-PBF is a technique that can find several problems due to a wide range of factors, which might modify the final results [21,22]. The melt pool size control, the thickness of the powder layer, the laser power, and the scan speed are just a part of the parameters that can affect fair powder fusion (Figure 1.20) [21]. The optimization of process parameters is necessary to achieve a fully dense part with a homogeneous microstructure to reach the best properties.

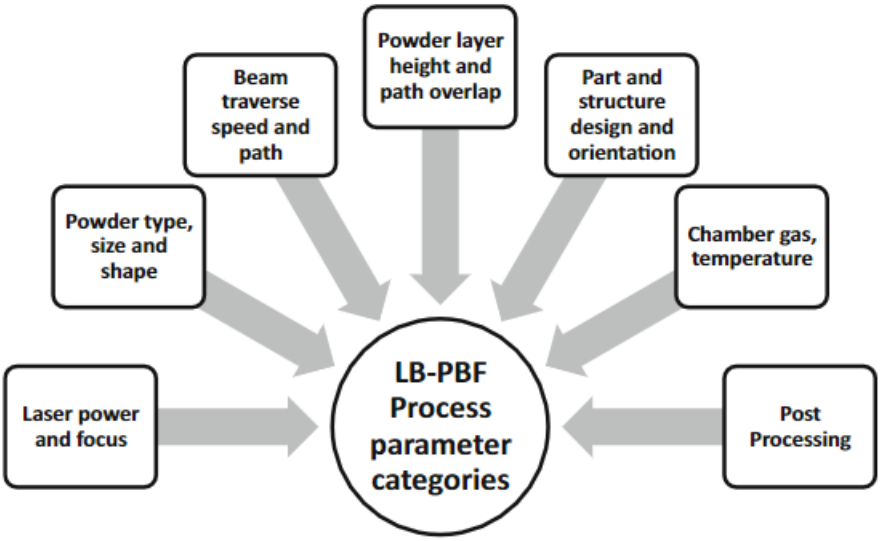

Figure 1.20 L-PBF process parameters [14].

The choice of a correct set of process parameters is fundamental not just for the final density or for the mechanical properties, but also for the quality, the geometries, and the operation times [21,22]. For every material, the process parameters are different because every element has different behavior from the others. Therefore, the optimization of the input parameters is necessary to achieve prefixed goals.

The most important are: *laser power P* [W], *laser speed v* [mm/s], *layer thickness t* [mm], and *hatch spacing h* [mm], which is the distance between each laser line. These are connected by the *energy density* E $\left[\frac{J}{mm^3}\right]$ [23].

$$E = \frac{P}{v*h*t} \qquad (1.4)$$

Energy density defines the energy input into the print process, and it has a huge impact on the final properties of the piece [23–26]. Energy input density can affect the presence and the kind of defects such as pores, lack of fusions or cracks, the high of the melt pools, and the final quality of the fabricated part [23–26].

1.3.3 Scan strategy

Another parameter that should be mentioned is the *deposition pattern.* In L-PBF there are four common deposition patterns: raster, bidirectional, offset, and fractal patterns [22]. The offset pattern is divided into offset-out and offset-in depending on the starting point of deposition (Figure 1.21) [22].

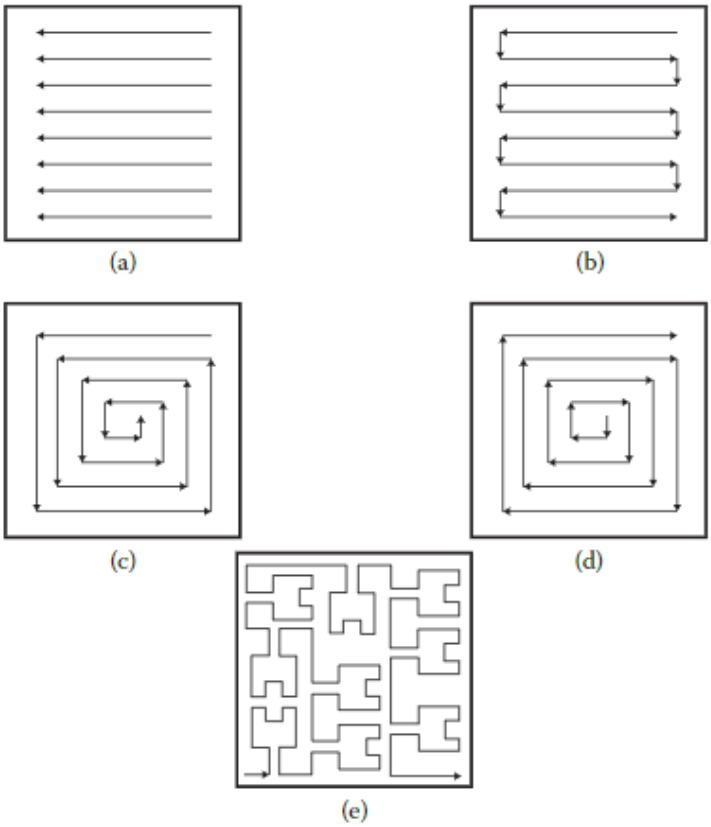

Figure 1.21 Deposition patterns: a) raster, b) bidirectional, c) offset-in, d) offset-out, and e) fractal pattern [15].

The different path strategies can significantly affect the geometry and the mechanical properties of the pieces because it is possible to reduce the residual stresses and the thermal distortions of the fabricated parts [22]. A correct scan strategy can improve smoothing and surface conditions, increasing the quality and properties of the pieces [21]. The laser scanning direction also affects the melt pool patterns, changing from face to face (Figure 1.22) [22]. In cross-section Y-Z it is possible to observe the classical melt pools with more definite shapes (fish-scale pattern); while in plane X-Z the melt pools are flatter.

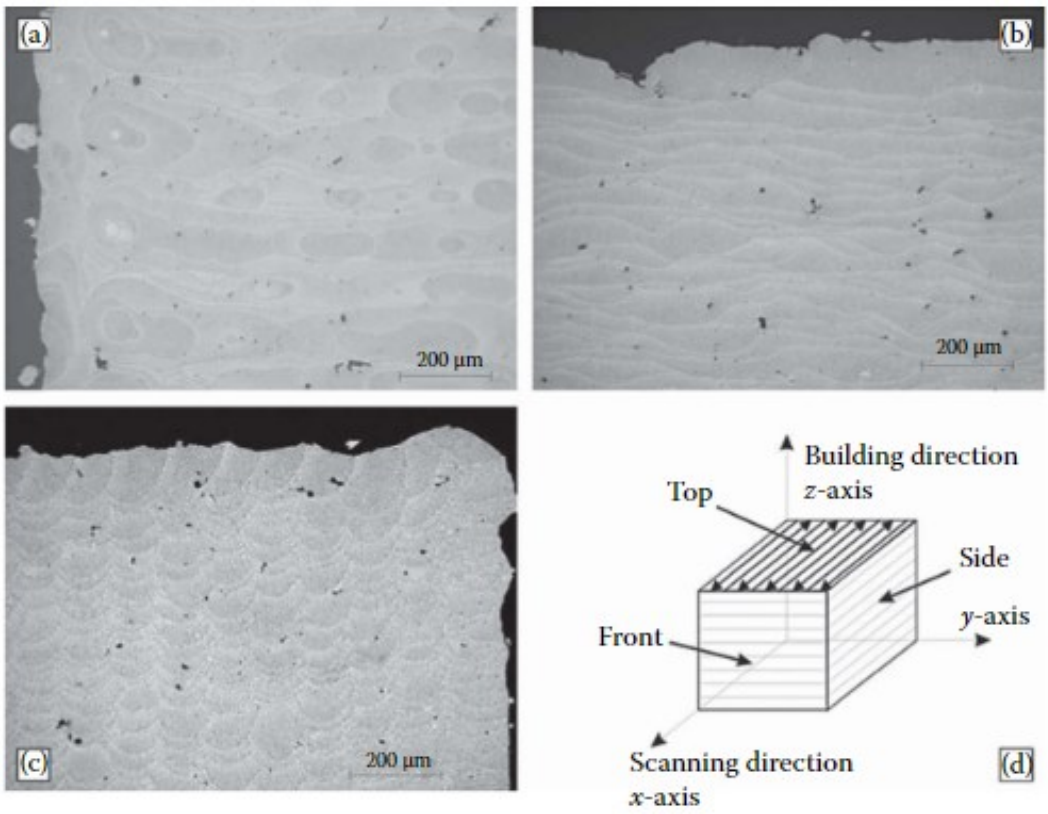

Figure 1.22 Influence of scan strategy on the melt pool structure: a) the top plane; b) the side plane; c) the front plane [22].

1.3.4 Defects

In the L-PBF there are four main defect categories [21]:

- *Porosity:* gas porosity, cluster porosity, and voids.
- *Flaws:* inclusion, lack of fusion, and contaminants.
- *Microstructure:* segregation.
- *Dimensional:* surface condition, distortion, and stair stepping.

Porosity

Porosity is a defect that forms in molten material or during the melting phase and solidification [21]. The formation of spherical or oblong voids occurs due to neither the presence of gas trapped, lack of fusions, or other issues (Figure 1.23) [21,22]. Gas porosity is different from other types of voids, differentiating both in the way of formation and in the form [21,22].

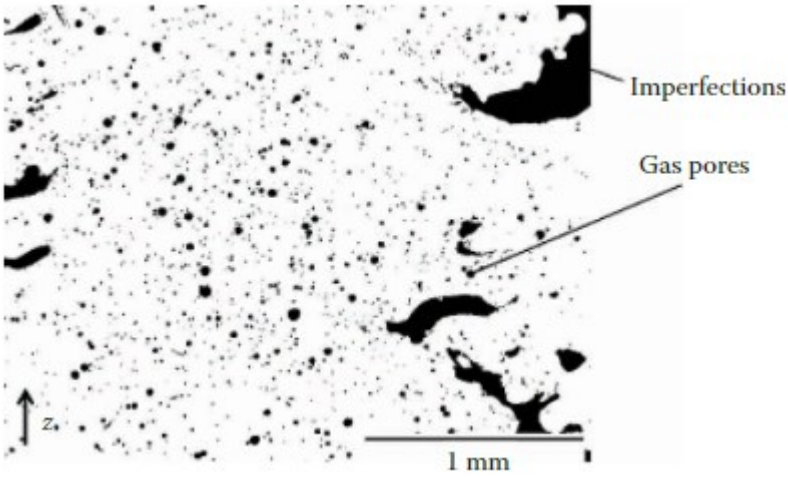

Figure 1.23 The optical micrograph shows regular pores and cavities in the material microstructure produced by L-PBF [22].

For example, a gas such as a hydrogen is readily absorbed into the molten metal and rejected during the solidification phase, thus creating bubbles or pores [21]. Argon is a gas that can get trapped in the dust during the atomization process, resulting in another source of micro-porosity [21].

Another cause of the formation of trapped gas is a consequence of the formation of keyholes (Figure 1.24), due to a too high laser power [22].

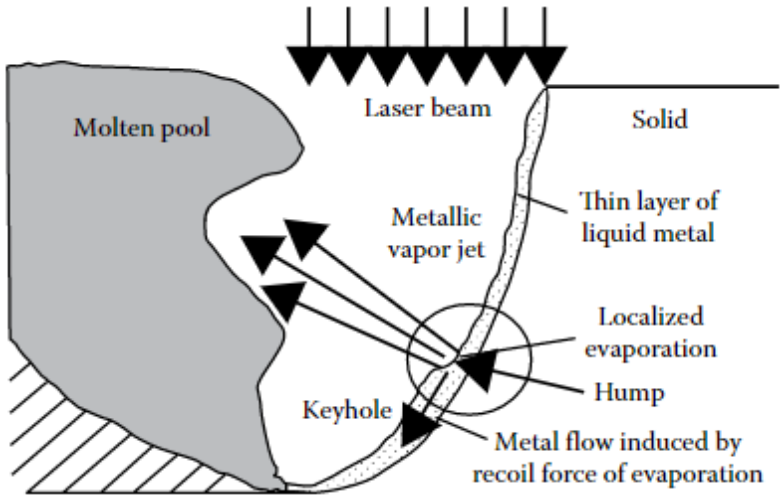

Figure 1.24 Illustration of keyhole [22].

A cloud of vaporized metal occurs and the superheated gas creates one depression in the melt pool [22]. This depression generates a vapor cavity in the metal melt, which can collapse and trap gas inside during solidification [22]. The gas trapped can also give rise to coalescence phenomena, generating, consequently, growth in porosity [22]. The typical form of porosity due to the presence of gas is spherical and can indicate contamination levels during the melting of the dust or storage [21,22].

The voids that do not arise from trapped gas can have different shapes (Figure 1.23) and can be due to shrinkage porosity [21,22]. This type of porosity occurs in the last stage of solidification in the mushy zone and is due to the expansion coefficient thermal and the volume of shrinkage during solidification, which leads to a drastic volume change [22]. Another type of void is due to common melt losses in L-PBF processes associated with powder packing density and incorrect deposit merger [21]. In this way, there will be the formation of non-fused or empty areas, which will contain inadequately melted powders or particles (balling effect) [22]. This type of defect does not have spherical geometric shapes, but they are more irregular [22].

Oxide defects can also lead to the formation of irregular porosity forms in the L-PBF technology [22]. Oxides can act as barriers limiting the passage of heat and melting, thus leading to defects (Figure 1.25) [22].

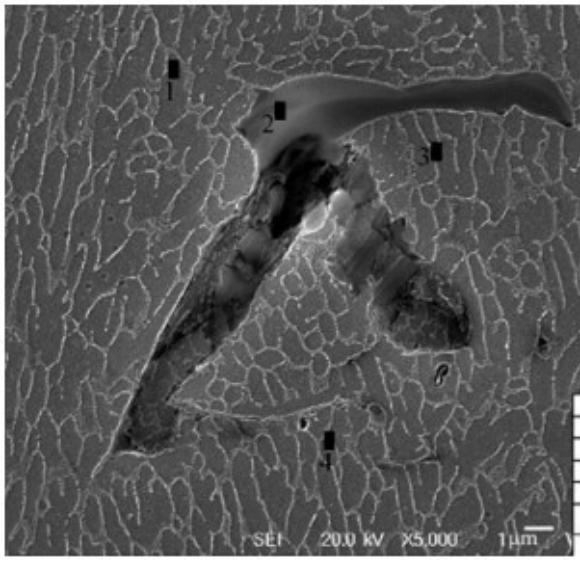

Point	1	2	3	4
Element	wt.%	wt.%	wt.%	wt.%
O	0.87	41.75	2.55	0.40
Mg	0.30	0.58	0.31	0.26
Al	88.57	56.42	86.96	88.17
Si	10.24	1.23	10.20	11.18
Total	100	100	100	100

Figure 1.25 Defect generated by oxide film [22].

Flaws

The lack of fusions, such as penetration losses, due to non-process parameters optimal, can lead to the formation of defects such as flaws (Figure 1.26) [21]. Incorrect depth of fusion, at each pass, can cause delamination of the part from the plane of construction or between layers in the deposited part [21]. Incorrectly fused particles can lead to the formation of cracks or defects in the internal structure (Figure 1.27) [21]. The presence of inclusions can lead to the formation of gaps or cracks in the piece [21]. Contaminants can vaporize during the melting process with enough force to be rejected by the molten puddle, thereby leading to the formation of internal defects [21].

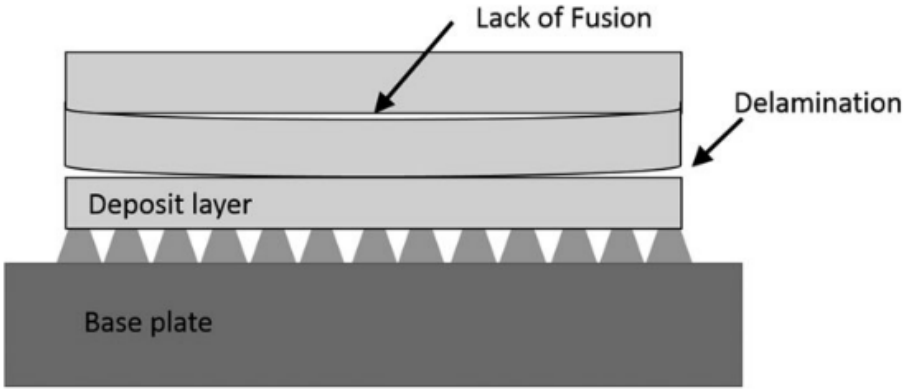

Figure 1.26 Defects of lamination or lack of fusion [21].

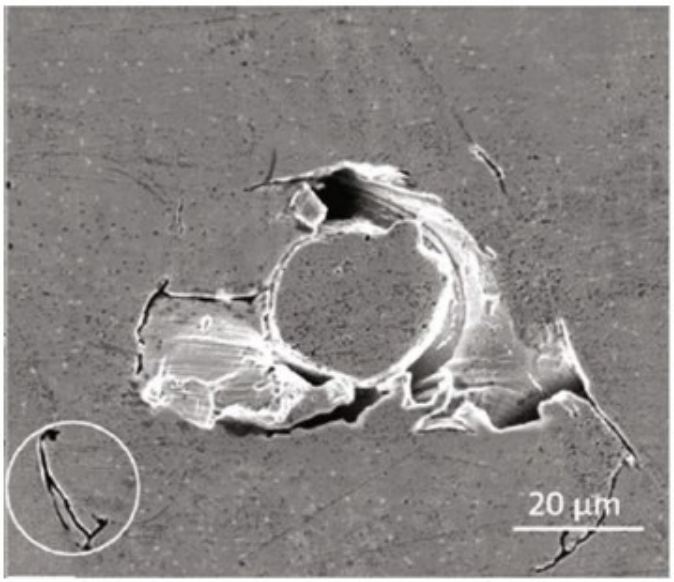

Figure 1.27 Unfused powder particle [21].

Microstructure

The microstructure in L-PBF is largely governed by the size of the laser, and by the speed of movement and power [21]. On a level microstructural, the melt pools due to the laser pass can be recognized (Figure 1.28) [21]. The border of these areas is associated with chemical segregation which makes the edge easily distinguishable, and this phenomenon can affect the properties of the deposit[21].

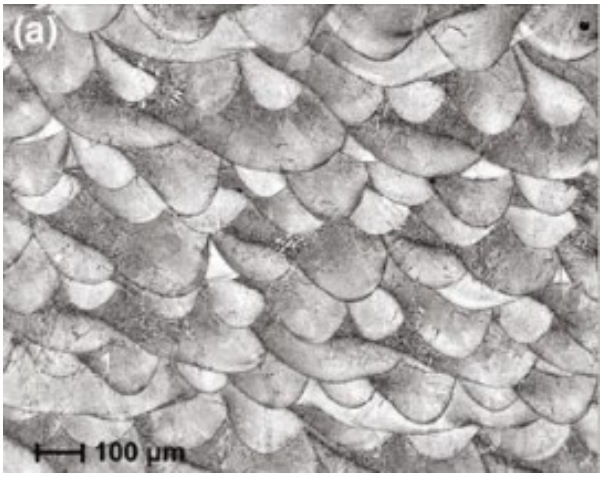

Figure 1.28 profiles of melt pools created by the laser [21].

Occur also situations of structural modification with loss of alloying elements, which vaporize during the heating and melting phase [21].

Dimensional

During the manufacturing phase of a piece and solidification can occur situations of distortion, which lead to geometric and surface defects [21]. "Slumping" is a dimensional defect that occurs in areas with insufficient structural support [21]. Can be associated with design defects, thin walls, downward surfaces, or protrusions [21]. There they can be surface tensions that generate rounded surfaces instead of edges alive, resulting in a loss of dimensional and geometric accuracy [21]. Incorrect process parameters can lead to splashes and droplets of molten or metal partially melted powder, thus worsening the surface and deposit quality [21]. The action gravity or surface tensions can act on the molten metal, generating empty areas, which become stress enhancers or crack propagators [21]. Distortions and shrinkages (Figure 1.26) can occur in localized regions during the solidification phase [21]. These factors generate a deterioration in the surface quality of the pieces, and conditions irregularities can reduce the resistance of the part, creating areas where the stress leads to fatigue failure of the component during service [21].

1.3.5 Microstructure

The one-piece microstructure produced using L-PBF technology is particular and characteristic, and it is strongly influenced by the printing process parameters [21,22]. The evolutions microstructural are strongly correlated to temperature peaks, exposure time, and the cooling rate [21,22]. A rapid cooling rate can produce a highly refined microstructure and form non-equilibrium phases [21,22]. This last parameter can therefore influence the properties of the whole piece, acting on the grain size,

the segregation of the alloy constituents, and the phase fractions that are formed [21,22]. The melt pool cools and solidifies quickly, and three main events are distinguished: nucleation heterogeneous, heat transfer to the "mushy zone" (the area between the melt pool and solid material), and microstructural evolution through heat treatment [22]. The phase-change heat transfer and momentum at the solid/liquid boundary of the melt pool is probably the most sophisticated physical process inherent to L-PBF [22]. During solidification take place a complex diffusion and heat transfer process, depending on the temperature [22]. Moreover, this temperature affects the evolution of the microstructure, which in turn depends on the type of material [22]. The microstructure is mainly governed by the process parameters of the laser, such as the spot size, scan speed, and power [22].

Analyzing the section in the X-Z plane (Z axis construction direction), a peculiar feature of the alloys printed using L-PBF technology is the directional columnar grain structure (Figure 1.29) due to the partial remelting of the grains at each pass of the laser, combined with the effect of heat dissipation of the previously deposited material [22].

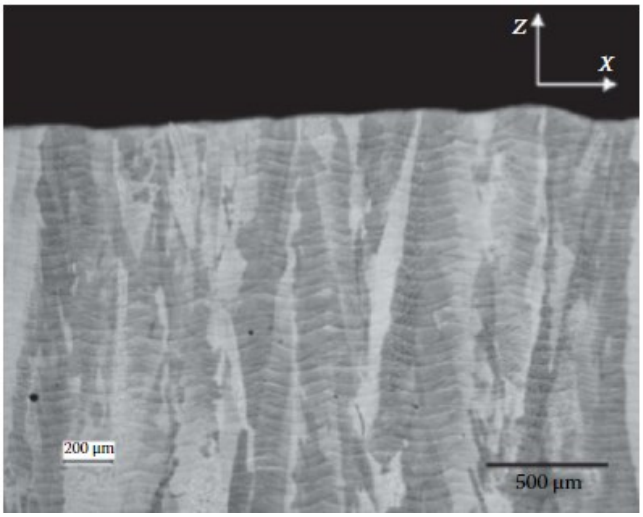

Figure 1.29 SEM image with visible columnar grains and melt pools pattern[22].

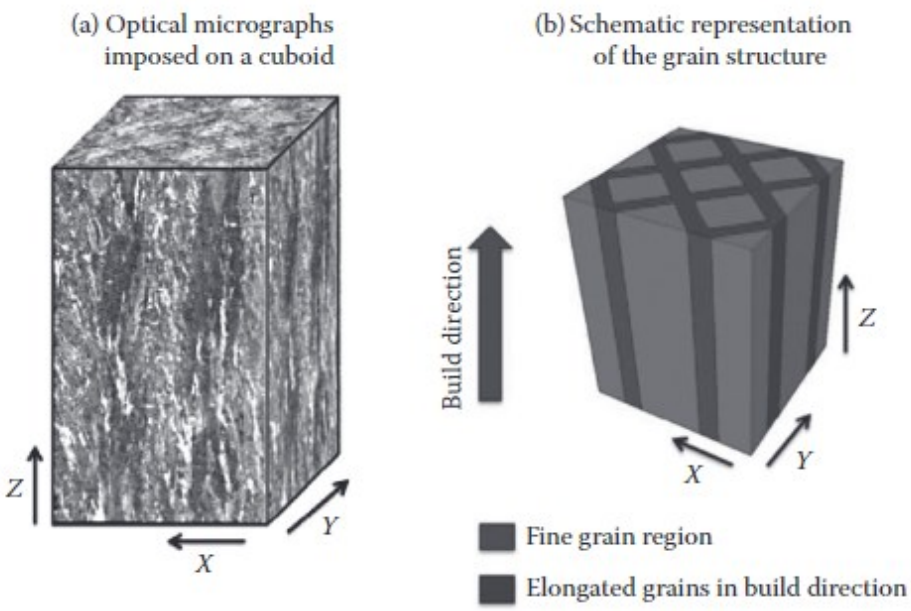

Figure 1.30 Grain structures in different planes X-Y and X-Z connect to the built direction [22].

This dissipation generates highly directional thermal gradients, with the heat flowing in a parallel direction to the construction axis (Figure 1.30), and therefore there will be a directional grain growth [22]. Analyzing the structure you can also recognize the "fishbone" pattern (Figure 1.29) generated by each pass of the laser [22]. In addition, the laser scanning strategy can affect the pattern of the grains on surfaces X-Y [22]. In AM processes there is mainly a directional growth of the grains, leading to conditions of both advantage and disadvantage. Therefore, trying to modify the paths of deposition to modify the solidification conditions to minimize the more possible stress concentrations or anisotropic properties in the piece [21,22].

1.4 LITERATURE REVIEW

The production of TRIP steel by Additive Manufacturing has never been investigated before and the goal of the fully dense material depends on the printing parameters. The printing parameters can affect several aspects of the pieces produced, and it is not easy to find the correct bunch of these. According to several authors [24–28], the Energy Input Density is the main value to take into consideration for the improvement of the production of this particular steel. The porosity of the pieces decreases with the increase of this parameter because the energy is enough to melt correctly the powder [21,22,29]. The trend is linear until it is reached a particular value where there is a variation and an inversion of the porosity. H. Chen et Al. [28] confirm the possibility of a declination of densification due to too high energy that acts on the powder. The increment of porosity in this work is correlated probably to

the formation of keyholes, which are formed by the vaporization of metal [21], producing gas pores. In general, the pores could be produced by gas entrapped into the powder during the process or by lack of fusion, and these are recognized by the shape of the defects [21]. Another problem found in the production regards the surfaces melted due to the high energy. The specimens with the lower porosity show a top area melted with a distortion of the geometrical shape. Taking into consideration these informations is fundamental to better know the behavior of this alloy under a different group of parameters. The hardness test is another important property that can give information about the process and the final result. Tolosa I. et Al [30] explain that the better representation of the hardness response of the material, it is necessary to do the test in a line scan with a high number of indentations positioned a few mm away. The micro-hardness test shows the variability of the results due to the presence of pores and defects in the piece produced by AM, but the mean value is similar to the value of the wrought material. The pores have the worst response to the indentation giving an HV lower than the expectations [30]. Therefore, the decrease in the porosity can provide indentation values more uniform on the surface. Analyzing the microstructure of "as-printed" and "heat-treated" material it is possible to evaluate the quality of the printing process. To obtain a bainitic microstructure it is necessary to follow an austempering treatment [1]. The bainite is formed by ferrite in a needle form and retained austenite in two morphologies: blocky and film [1,2,11]. The austenite has a fundamental role in this alloy to allow the TRIP effect, and its stability is necessary to have a better effect [2,11,17]. In the printed material, the obtained microstructure both in martensitic and bainitic form is the same compared to the wrought material, confirming the goodness of the AM process on this alloy. The XRD confirms the correctness of the printing process, showing volume fractions of two phases similar to the bulk and without big differences between every specimen. A particular behavior of the microstructure is obtained in the melt pool, where there is a variation between boundary and core. Dilip J. et Al [23] show that the boundary zone is subjected to a tempered heat treatment highlighted by different colors to the core. Zhao X. et Al [31] demonstrate that there is also a decarburization process, and a subsequent difference in carbon content between boundary and core, where the latter is higher. These phenomena are confirmed by a difference in the micro-hardness between the boundary and core of the melt pool, with a higher value in the center. The aim of this work is to analyze the first bunch of printing parameters. The complete characterization of specimens gives important informations, in order to better understand the behavior of the alloy under different parameters. Subsequently, the second part is about the improvement of the printing parameters to obtain a higher level of quality for the final product. The main focus is to evaluate if this alloy could be produced by additive manufacturing.

2 MATERIALS AND METHODS

This chapter briefly introduces the tools and methods used to investigate the quality of steel alloy samples produced by L-PBF in a cubic shape of dimensions 10x10x10 mm. In particular, the design of the experiment, sample preparation, pore and melt pool analysis, hardness, heat treatments, and microstructure analysis are described.

2.1 DESIGN OF EXPERIMENT

The experiment was designed to evaluate the quality of steel alloy samples printed by L-PBF, using several different printing parameters. In particular, a full characterization of cubic samples with dimensions 10 x 10 x 10 mm was done (Figure 2.1), and the results were evaluated to understand the possibility to produce this kind of alloy through additive manufacturing. After that, new parameters were chosen to reach the best condition to print this particular steel alloy. Firstly, the pore density of every sample was evaluated and it was done to find a possible trend connected to the parameter choices. The pore analysis gives the main information about the printing process because it is possible to understand the influences of the parameters on the material density. Moreover, this analysis gives an idea of the kind of defects, which affects the final quality of the samples. The melt pool analysis also gives important information about the parameters process. Secondly, the hardness test, which was carried out after the optical analysis of the surfaces, is necessary for the first evaluation of mechanical properties, and also for a comparison with the bulk material traditionally produced. Reaching a fully dense structure with mechanical properties similar, or better, than the bulk was the main goal of this study. The microstructures of the samples were evaluated before and after the heat treatments, and to do this different strategies such as SEM, XRD, EDS and EBSD were used. Each technique gives fundamental information about the microstructure on qualitative and quantitative levels, micro-segregation, and compositions of the samples. The final stage of this study was to use every information obtained for trying to improve the printing parameters to reach the perfect conditions, which allow to have the same or better properties compared to the traditional methods for the production of this kind of alloy.

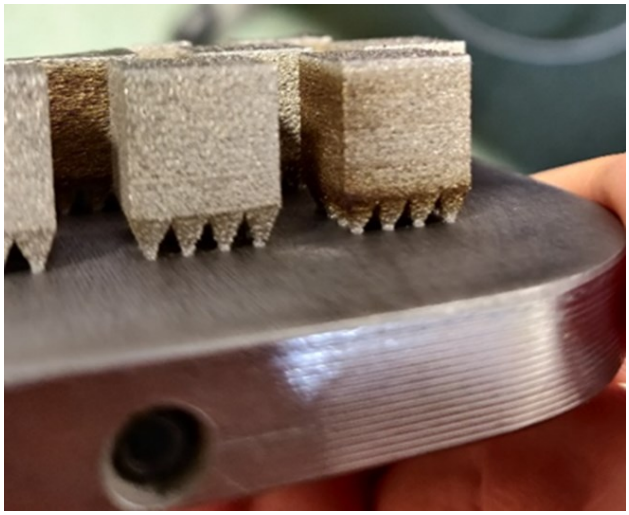

Figure 2.1 Cubic Sample on the platform after the printing process.

2.2 POWDER

2.2.1 Production

The production of metal powders can take place through different processes. In particular, the powder used in this study was produced by gas atomization. The atomization process (Figure 2.2) requires the use of a high-pressure fluid jet that breaks a stream of molten metal into very fine droplets. These droplets subsequently are quenched by the gaseous atmosphere in the chamber to solidify into particles with spherical or nearly spherical shapes. In gas atomization, the fluid used to obtain liquid droplets is usually an inert gas, for example, argon, to avoid oxidation. The dimension of the powders depends on parameters such as the surface tension of the molten metal, the melting temperature, and the velocity of atomization gas. During the atomization, the dimension of the powders decreases with a decrease in surface tension, increasing the fusion temperature, or increasing the gas velocity.

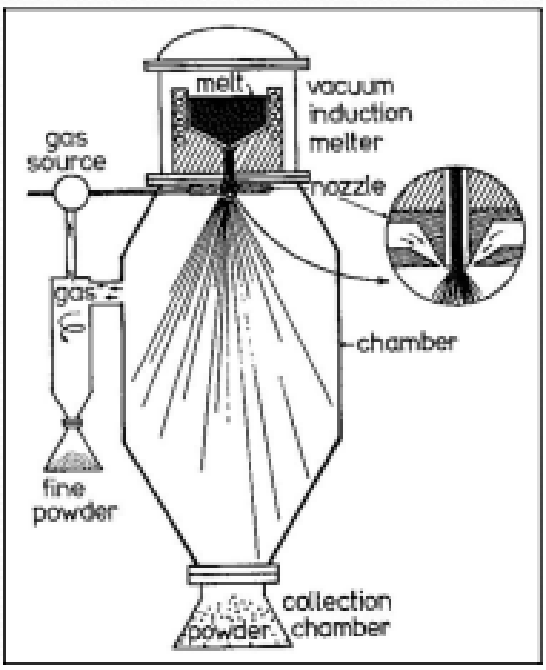

Figure 2.2 Gas Atomization scheme of the process.

There are several benefits of atomization: a huge number of metals can be processed, high purity alloys can be prepared to start from the melt, the particles are impurities-free, the size and the shape of particles can be controlled, and very high productivity.

2.2.2 Powder Characterization

Gas atomized powders of TRIP steel with a composition reported in Table 2.1 were used in this experiment. The range of the size of the powders was 15-53 µm with a median diameter of 31.2 µm, and 90% of the powder does not exceed the value of 47.4µm (Table 2.2). The SEM image of the powder in Figure 2.3 shows it has an almost spherical shape, with an apparent density of 4.13g/cm^3.

Element	C	Si	Mn	Al
Wt%	0.38	3.2	2.6	0.1

Table 2.1 Steel alloy composition.

Effective diameter D10 [µm]	Median dimeter D50 [µm]	Particle size D90 [µm]	Apparent density [g/cm^3]	Flowability [sec/50g]
20.4 ±0.8	31.2 ±1.1	47.4 ±2.2	4.13 ±0.03	13.9 ±0.6

Table 2.2 Powder Characterization. D10: the particle diameter corresponding to 10% cumulative undersize particle size distribution; D50: corresponding particle size when the cumulative percentage reaches 50%; D90: 90% of the total particles are smaller than this size.

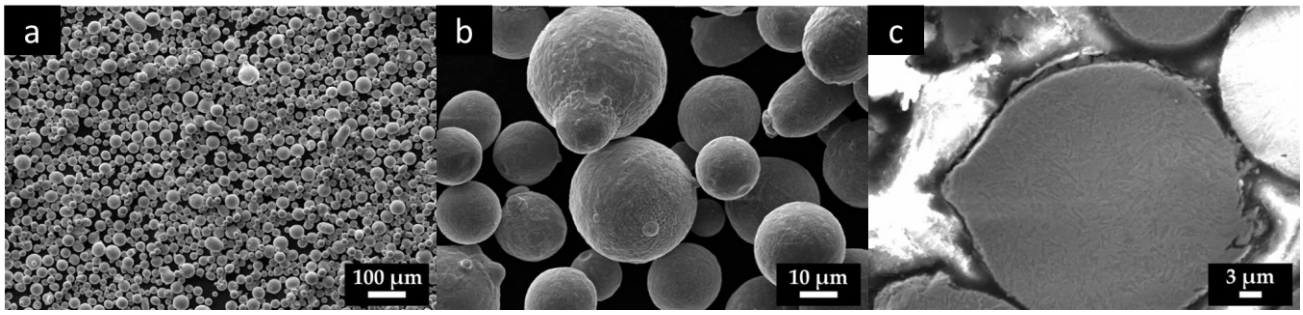

Figure 2.3 The SEM pictures of powder with different magnifications a, b, and c.

2.3 PRINTING PARAMETERS

The first set of parameters is shown in Table 2.3. This list of parameters was chosen based on literature results considering, due to lack of data regarding carbon steels, parameters for high-Si ferrous alloy and 316L stainless steel. In particular, the optimum energy density to obtain full dense samples were combined with the suggested parameter to obtain full dense 316 L samples from the L-PBF facilities supplier.

Sample	Power [W]	Distanza Punti	Tempo di Permanenza	Speed [m/s]	Hatch [um]	Layer Dist [um]	Energy Density [J/mm^3]
1	220	30	60	0,5	110	60	66.7
2	195	45	60	0,75	110	60	39.4
3	220	45	60	0,75	110	60	44.4
4	170	30	60	0,5	110	60	51.5
5	270	45	60	0,75	110	60	54.5
6	295	30	60	0,5	110	60	89.4
7	245	30	60	0,5	110	60	74.2

Table 2.3 Printing Parameters of the first set.

2.4 PORE ANALYSIS

The pore analysis is one of the most important parts of this study. Thanks to this evaluation it is possible to understand what kind of pores and defects are inside the material, and how the parameters affect the final density. To do this, pictures were taken with the optical microscope, and a quantitative measurement was done with the support of the software ImageJ [32]. In the beginning, the first pore analysis was evaluated on the surface of three external faces for every cubic sample. Specimen was prepared according to standard metallographic preparation: grinding with SiC papers (from 500 to 1200 grit) and after were sonicated in acetone. Then, polycrystalline diamond suspensions of 6,3, and 1 μm was utilized to polish the surface. Now, the sample was ready for the optical microscope, which was used to acquire images of the interested area. To evaluate the pore density and for correct analysis (for good statistics), it was necessary to take a fair number of surface photos. Ten micrograph were taken with a magnification of 5X and 10X, for every external face of the cube. Subsequently, the pictures were processes with ImageJ, which allows a numerical evaluation of the number and area of the pores. These data were subsequently transferred on Origin [33], which is a software that can evaluate different parameters, and it can allow for an estimation of the dimensional distribution of the pores. Thanks to "pore mean" and "pore interquartile" given by Origin, it was possible to take into consideration the average dimension and the kind of pores. Interquartile and Mean are useful for evaluating the connection between the printing parameters and the obtained results. For example, a big interquartile or mean means the presence of pores given by a lake of fusion. On the other hand, a small value of these means a bigger presence of gas pores. These two kinds of pores are mainly addicted to the laser power and energy input density of the print. After that, the quantification of the pore density was carried out for every sample. To do this, it is necessary to apply the formula:

$$Pore\ Density\ (\%) = \frac{Sum\ of\ the\ pore\ area}{Total\ surface\ of\ pics} * 100$$

where the "sum of the pore area" is given by Origin, the "Total surface of pics" is calculated using ImageJ and multiplying the area of a pic with the number of analyzed pics.

Nevertheless, this part was not satisfying for comparison because the porosity was very high, and it changed a lot for every layer deeper, so it was too variable. Therefore, further analysis at the core of the specimens. A slice of 3 mm was cut from the corner with a micro-cutter machine Brillant 210A (Figure 2.4), and it was evaluated the pore density inside. 10 pictures were taken of the area with 3 different magnifications: 5X, 10X, and 20X. The strategy of polishing and pore analysis was the same as the surface. At this point, the values of Energy Input Density were calculated for every sample using the formula in chapter 1. This data is useful for a better understanding of the behaviour of the

printed materials under different printing parameters, and it is also possible to find a trend between pore density and energy density. All the images were acquire with optical microscope Leica (Figure 2.5).

Figure 2.4 Micro-Cutter Brillant 210A

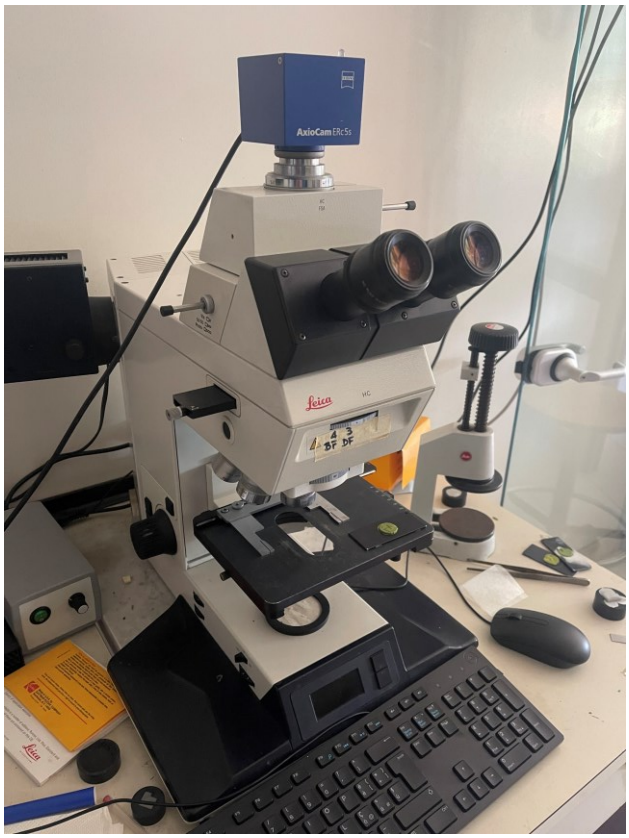

Figure 2.5 Optical Microscope Leica.

2.5 MELT POOL ANALYSIS

The melt pool analysis can give different information about the printing and the parameters that are chosen. Melt pools were revealed after standard metallographyc preparation and etching with Nital 2 (2% nitric acid and 98% ethanol). Ten micrographs were taken with each magnification (5X and 10X). The high was calculated from the bottom of a layer to the top because the melt pools were quite flat. For every pic, 10 measurements were taken of different melt pools. After that, Origin was used to analyze the data, finding the "Height Mean" and the "Height Interquartile".

2.6 HARDNESS

The hardness test gives a first evaluation of the mechanical properties of the sample compared to the bulk formed by traditional methods. This is one of the first terms of comparison between the two process methods, and it can give information about the performance of the as printed samples. This is done by a load in a normal direction of the surface, which generates a localized compression. There are different scales to measure the hardness: Brinell, Vickers, and Rockwell. The Vickers hardness test (Figure 2.6) is the most precise measurement in terms of precision and repeatability, and was

adopted in this work. It is a static hardness test method used for macro and microhardness testing. It is an optical method of testing where the size of the indentation done by the indenter is measured to determine the hardness value. For the hardness, 66 indentations were done with a weight of 300g, which were divided into 33 verticals and 33 horizontals along a straight line for every sample (Figure 2.7). Subsequently, the 2 diagonals of the cubic indentation were measured, and the average of these values was calculated. After that, a proper conversion table was utilized to express the hardness in HV. The final stage in this step is to take the average value of the 66 indentation for every sample. This strategy was applied on the as-printed samples. The measurements were done by a microdurometer Leitz Wetzlar Germany 721 464 in Figure 2.8.

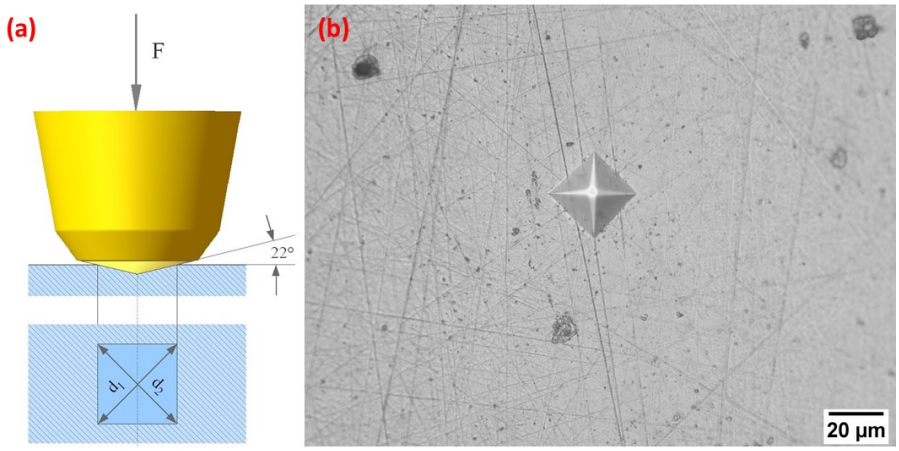

Figure 2.6 Hardness test scheme. a) representation of the scheme; b) example of indentation.

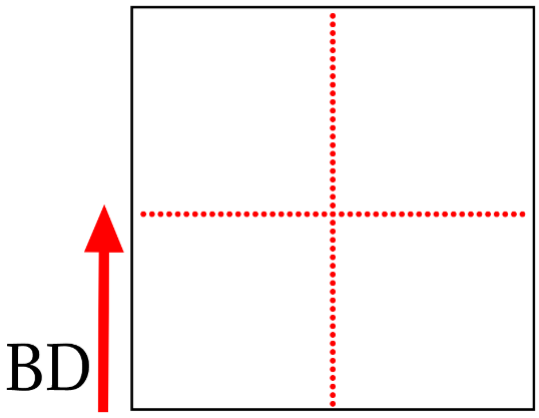

Figure 2.7 Imprint strategy for the hardness test. BD: built direction.

Figure 2.8 Microdurometer Leitz

2.7 SEM

"Scanning Electron Microscope" (SEM) is a microscope that does not use visible light but an electron beam, in order to observe the samples, generated by an electron source. The beam is moved on the surface of the specimen by series of scanning coils, and it is focused and condensated by electromagnetic lenses. An accelerating voltage is also applied to modify energy and wavelength of the electrons. The SEM operates in vacuum to protect the electron source and control the beam. The different signals, deriving from the interaction between the electron beam and the investigated specimens, are manipulated by dedicated detectors and converted into electrical impulses sent to a monitor in real time. The result is an image in grey scale with high resolution at high magnifications (Figure 2.9). Thanks to this technology it is possible to analyze the sample microstructures with high precision and capture particulars that are impossible to see with an optical microscope. SEM micrographs of samples as printed and heat-treated were taken to investigate the microstructure with different magnifications before and after the treatment. In this work a SEM Zeiss EVO MA10 (Figure 2.10), equipped with a LaB6 filaments, was used to analyse the microstructures.

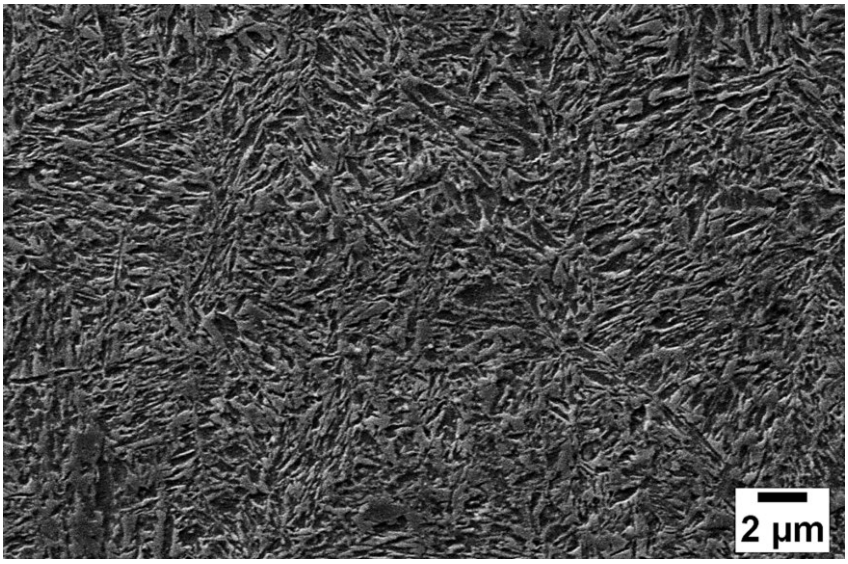

Figure 2.9 SEM image of martensitic microstructure.

Figure 2.10 SEM Zeiss EVO M A10.

2.8 EDX

"Energy Dispersive X-ray Spectoscopy" is a technique that gives information about the chemical composition, both qualitative and semi-quantitative [34]. EDX is used in combination with SEM. The electron beam interacts with the surface of the sample, causing X-rays to emit from the material, and the emission energy depends on the material examined and discriminate depending on their characteristics energy [34]. Through this analysis it is possible to obtain local information but also

mapping the area knowing the element distribution. In this way, it is possible to produce an image (Figure 2.11) of each elements in the sample [34].

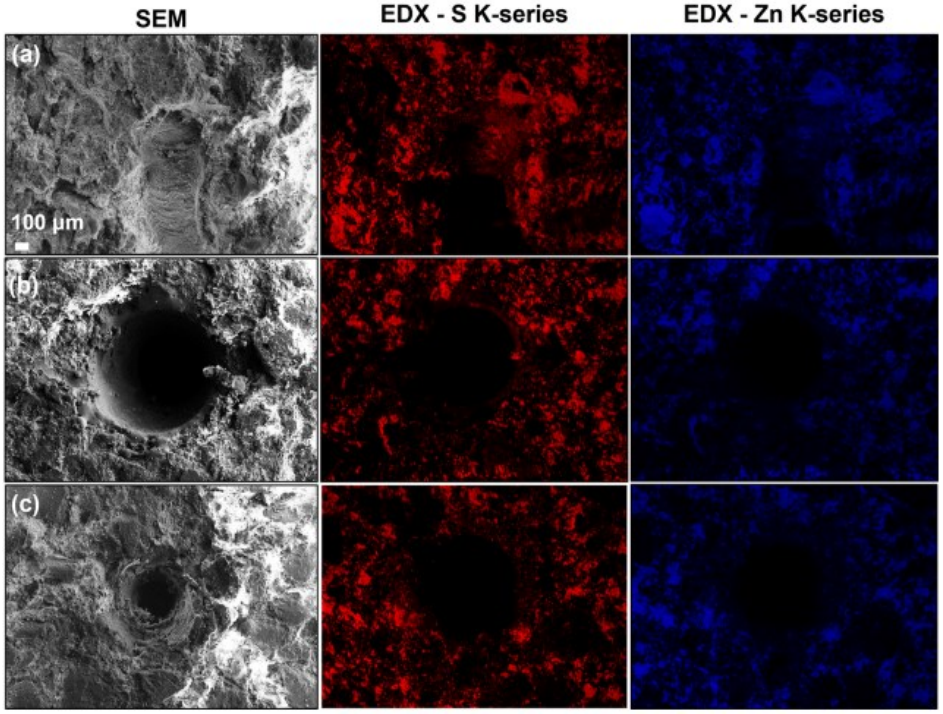

Figure 2.11 Example of EDX analysis maps [35].

2.9 XRD

"X-Ray Diffractometion" (XRD) is a technique for analysing the atomic structures of materials. It is a non-destructive and it uses X-rays generated byradiation tube. X-rays scatter from a material with a structure on this scale, causing interferences. As Figure 2.12 shows, this results in a pattern of different intensities (lower and higher) due to the constructive and destructive interferences according to Braggs Law [36]. The interaction of the incident rays with the atomic planes of the sample (Figure 2.13) produces constructive interaction when Bragg's condition [36] is satisfied:

$$m\lambda = 2dsin\theta \qquad (m = 1,2,3 \dots)$$

where λ is the wavelength, d is the distance between atomic planes, θ is the diffraction angle of radiation, and m number of wavelengths.

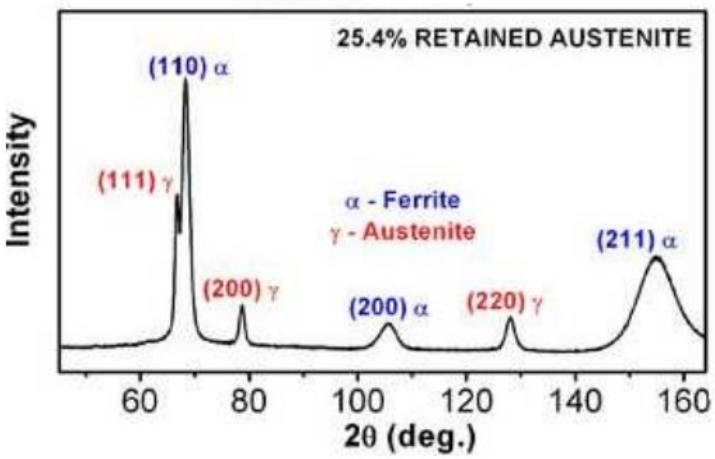

Figure 2.12 Example of XRD spectrum.

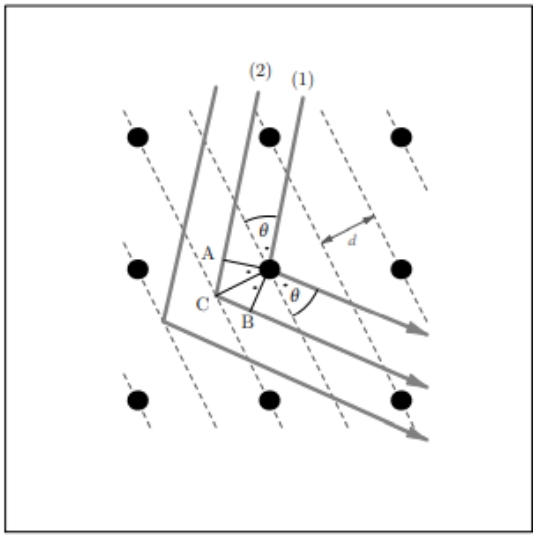

Figure 2.13 Phenomena of X-Rays diffraction due to the interaction with atomic planes [36].

Knowing the wavelength and measuring the angle θ, it is possible to obtain a full characterization of the geometric structure of a crystal. Therefore, this experiment allows to obtain information about the present phases (Figure 2.12) in the microstructure, and it is also possible to evaluate quantitatively the amount of them. XRD gives information about the lattice parameters and the geometries of the unit cells. In particular, in this study, XRD difractometer (Siemens D500), Cu – Kα lamp and detector monochromator (Figure 2.13) is used to investigate the number of different phases in the samples as printed, and in samples modified by subsequent heat treatment. The setup for the analysis is reported in Table 2.4.

XRD SETUP	
2θ	40 – 105°
Step Scan	0.025°
Acquisition Time	3 (sec)

Table 2.4 Setup XRD.

Figure 2.14 Difractometer Siemens D500.

2.10 HEAT TREATMENT

The heat treatments are fundamental to obtaining the desired structure and correct properties of the specimens. Heat treatment is a process divided into three main stages: heating, isothermal holding periods, and cooling [8]. In this study, it is necessary to obtain a bainitic structure from printed alloy steel. To achieve this particular microstructure is necessary to follow an austempering process [8] (Figure 2.15). The samples are heated at a temperature of 950°C (above A_{c3}) for 10 minutes to reach a complete austenitic microstructure (austenitization). After that, the samples are cooled down with in air rapidly, to avoid reconstructive transformation, until a temperature of 325°C and held at that temperature for 3 hours for bainitic transformation. Specimen temperature was constantly monitored with a k-thermocouple. At the end of the 3 hours, the pieces are quenched in water. The other heat

treatment used in this study is the annealing (Figure 2.16), which consist in a heating to 900°C for 15 minutes and subsequently cooled inside the furnace until room temperature.

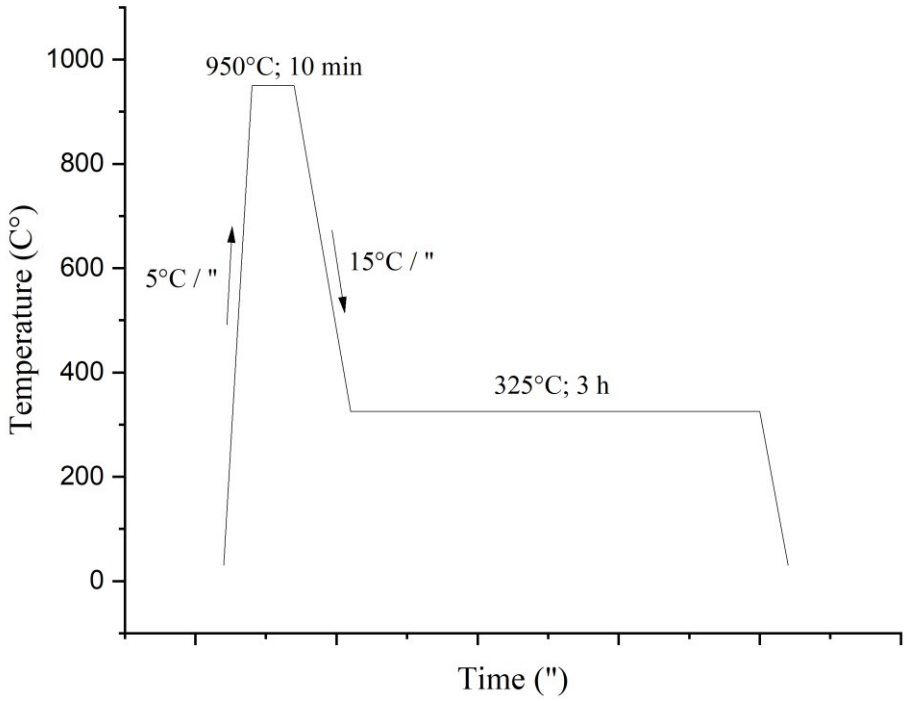

Figure 2.15 Heat Treatments: Austempering.

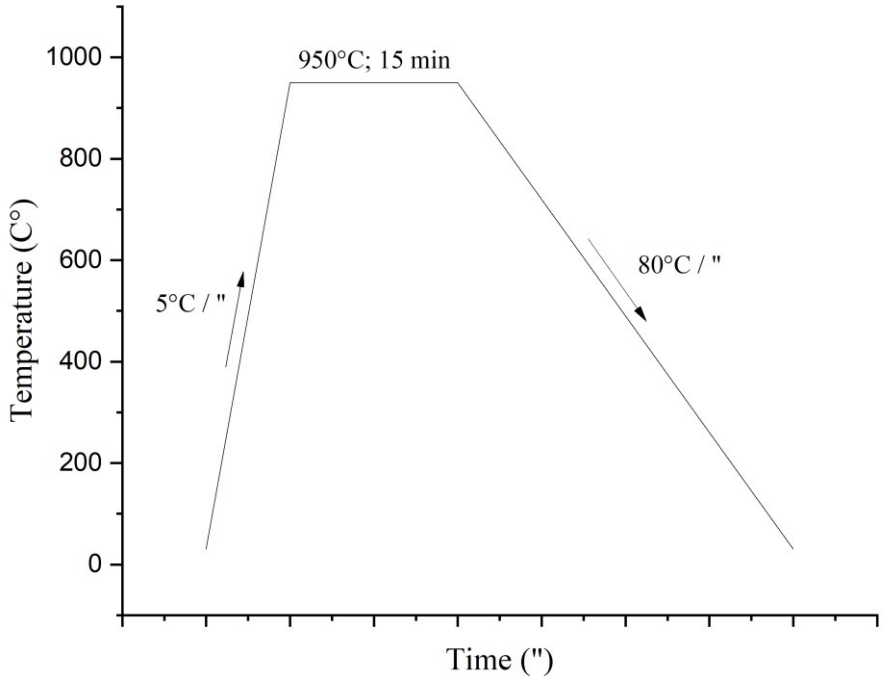

Figure 2.16 Heat Treatment: Annealing.

2.11EBSD

The "Electron Backscatter Diffraction" (EBSD) is a technique used to study local crystallographic orientation in the microstructure. The data collected with EBSD are distributed and can be represented in maps and images, enabling an examination of localized features in samples. The modern commercial system are capable of different numbers of diffraction patterns every second. This makes it possible to scan with different spatial resolutions across the surface of a sample and to collect all the data for a full characterization of the microstructure. EBSD provides several information about the crystallographic nature of the sample. EBSD works with a stationary electron beam that interacts with an inclined crystalline sample, and the diffracted electrons form a pattern detected by a fluorescent screen. The diffraction pattern is representative of the crystal structure and orientation at the area where the samples interact with the electron beam. Therefore, the diffraction pattern allows to determine the crystal orientations, grain boundaries, grain morphologies, and crystallographically different phases. In this study, the EBSD maps were utilized to have an idea of the microstructure of the samples produced by L-PBF. EBSD measurements were performed on selected samples with a FEI QUANTA 250 FEG-SEM (Thermo Fisher Scientific, Hillsboro, OR, USA) operating at 20 kV, equipped with an AMETEK EBSD (AMETEK BV, Tilburg, The Netherlands) system and OIM Analysis™ software. 70 x 100 µm2 areas were scanned along the specimen's longitudinal direction.

The procedure for EBSD measurements included etching-polishing cycles and final steps with 200 nm and 50 nm colloidal silica suspension.

2.11.1 EBSD Maps

In the EBSD analysis, there are three different kinds of maps: Pattern Quality Maps, Phase Maps, and Orientation Maps. The Pattern Quality Map shows the quality of the pattern highlighting the poorer and the higher quality (Figure 2.17) by a grayscale. The quality is influenced by several factors: orientation, contamination, sample preparation, etc.

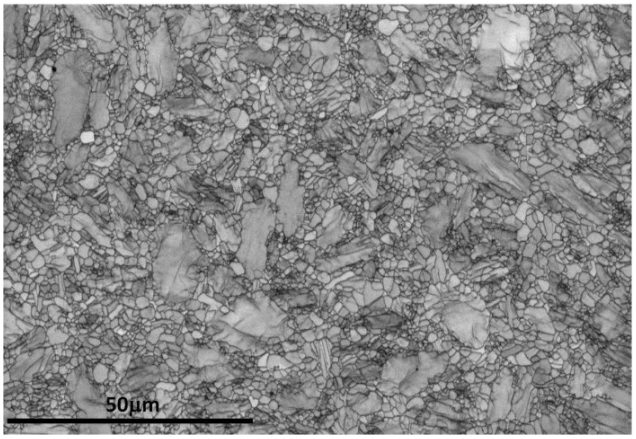

Figure 2.17 Quality Map shows the high and poor quality of the pattern using a grayscale.

This map reveals features invisible in the electron image such as grain boundaries, internal grain structure, and surface damages. The Phase Map (Figure 2.18) identifies the different phases. These can be represented with different colors, highlighting their distribution into the material.

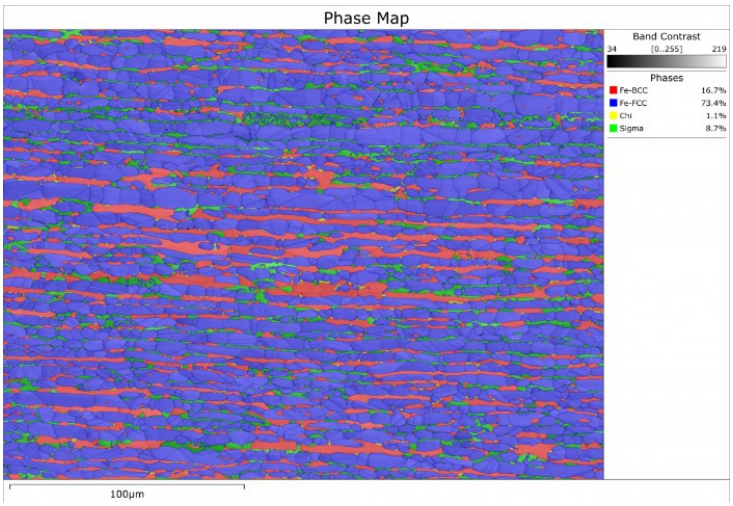

Figure 2.18 Phase Map shows the different phases using different colors.

The Orientation Maps collect orientation data (Figure 2.19). This map uses colors to identify the orientation of the grains in a microstructure.

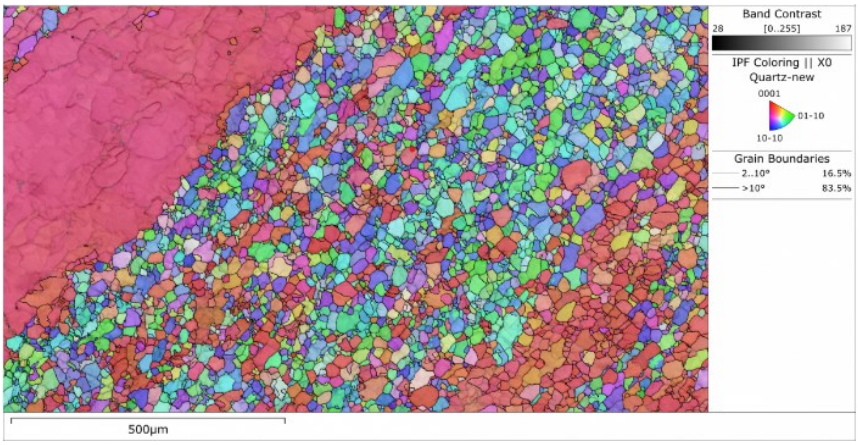

Figure 2.19 Orientation Map shows different orientations of the grain pattern using different colors.

3 RESULTS

This chapter presents the data and the results obtained from the methods and evaluations made in the previous chapter. In particular, the chapter is divided into two parts: the first is about the results from the first set of parameters; while, the second one regards the results from the second set, which are the optimized parameters.

3.1 SURFACE POROSITY

The first analysis is focused to observe and analyze the surface of three sample faces, in order to have a starting idea about the quality of the L-PBF printing. The same schedule was done for every sample, taking photos after the polishing. In Figure 3.1, it is clearly represented the situation on the surface of every sample. In particular, it is possible to detect the difference in the pore density and the difference in the kind of pores based on the printing parameters. The pore density seems to be huge and this is not good for an industrial application. High porosity can strongly affect in a negative way the mechanical properties of the pieces. Thanks to the use of ImageJ and Origin, it was possible to quantify and analyze these data, in order to obtain a better comprehension of what is visible from the photos. The results are collected in the graph in Figure 3.2 and Figure 3.3, where it is shown the "pore mean" and the "pore interquartile" of every sample. Considering the behavior of each specimen, the mean area of the pore is in the range of 150-990μm^2 which is huge; while the values of interquartile fluctuate between 40 and 220μm^2. These values show a big oscillation between every specimen and there isn't a detectable trend, but it seems to be casual and not correlated to the printing parameters. As it is explained in the previous chapter (2.4), these data are useful and interesting to better understand the evolution of the porosity of the samples. Another important data is the pore density (Figure 3.4), which gives a numerical evaluation of the porosity in every piece. The value of pore density is in the range of 8-13%, and this bad porosity is probably related to problems during the printing process, solidification, and heat transfer. The analysis in this part is not useful for the comparison between the samples and the evaluation of parameters because the data and the pictures are not representative of the real situation and the real behavior under different parameters.

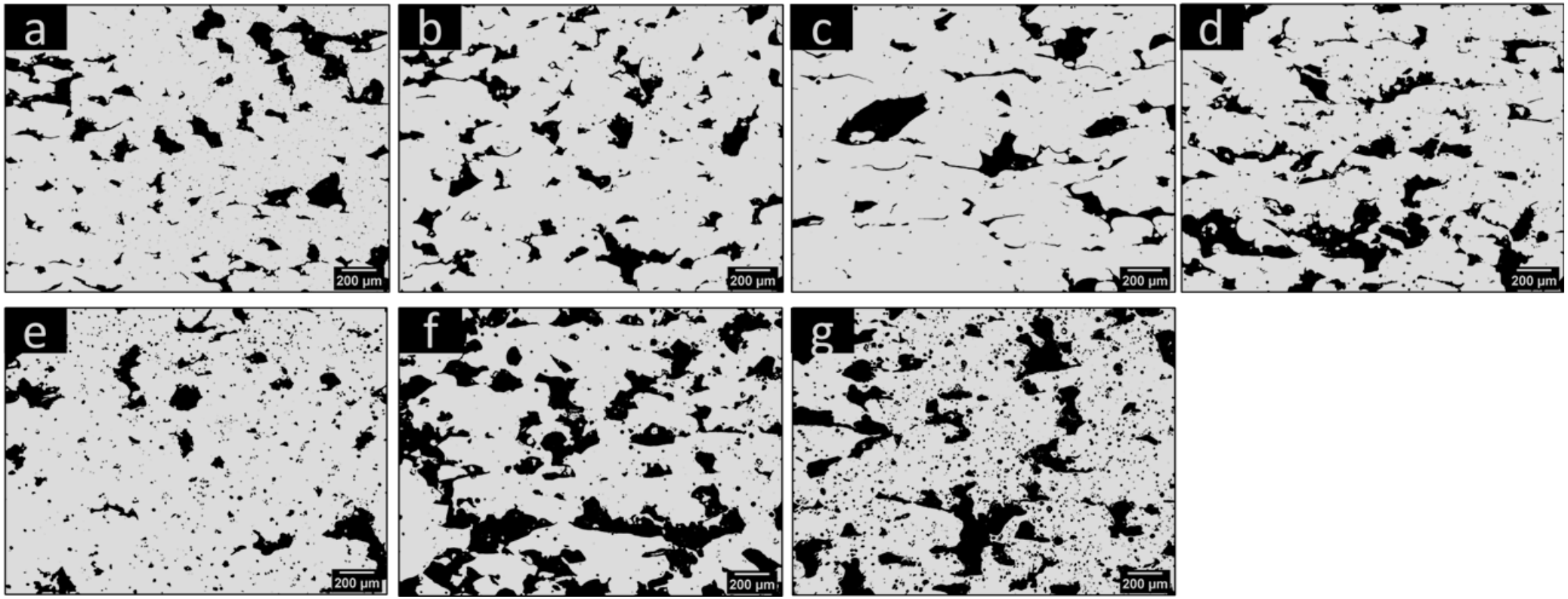

Figure 3.1 Surface Porosity of every sample: (a) sample 1, (b) sample 2, (c) sample 3, (d) sample 5, (e) sample 6, (f) sample 7, and (g) sample 9

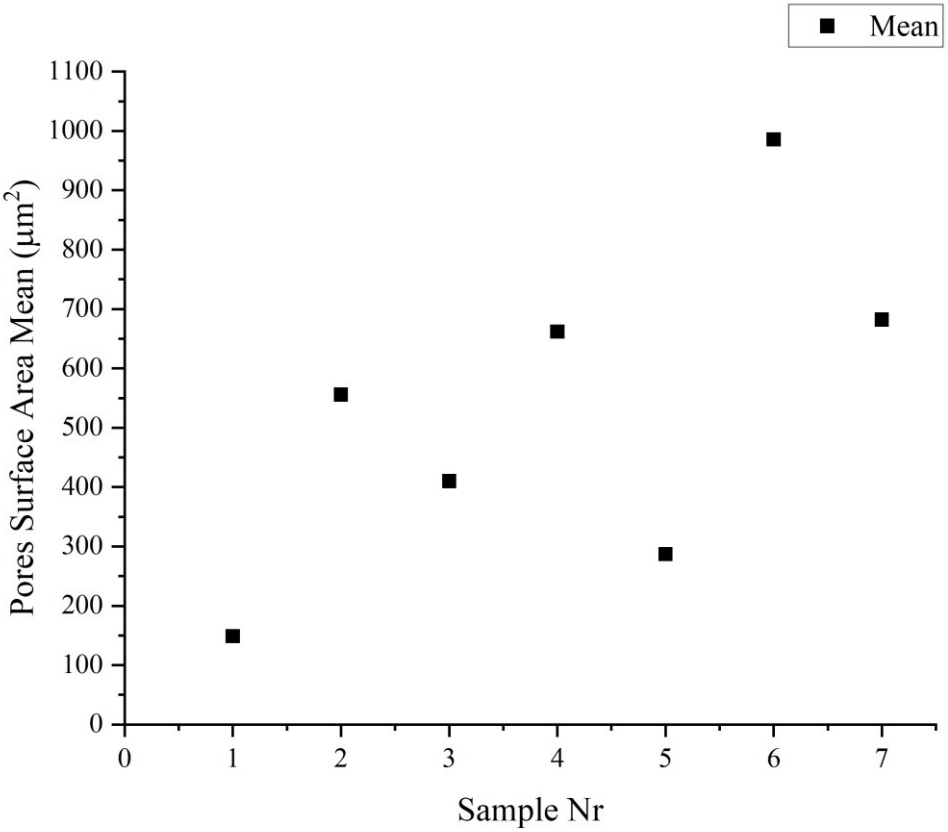

Figure 3.2 Graph of the Pore Mean. Trend variation of mean area of the pore vs samples.

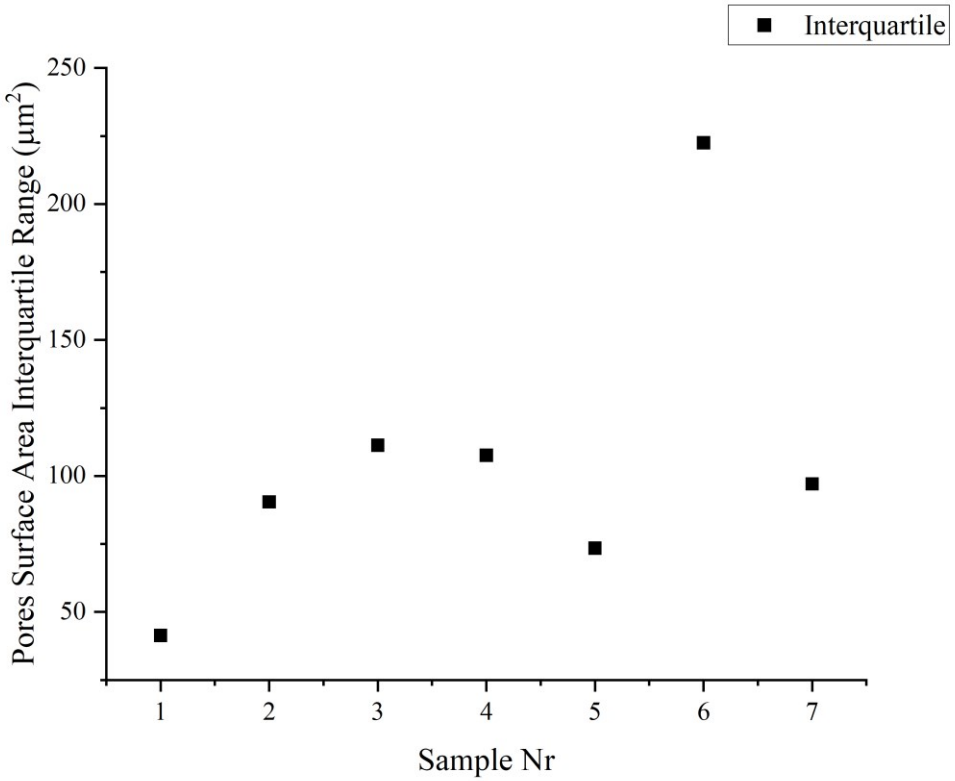

Figure 3.3 Graph of the Pore Interquartile. Variation of the pore interquartile for every sample.

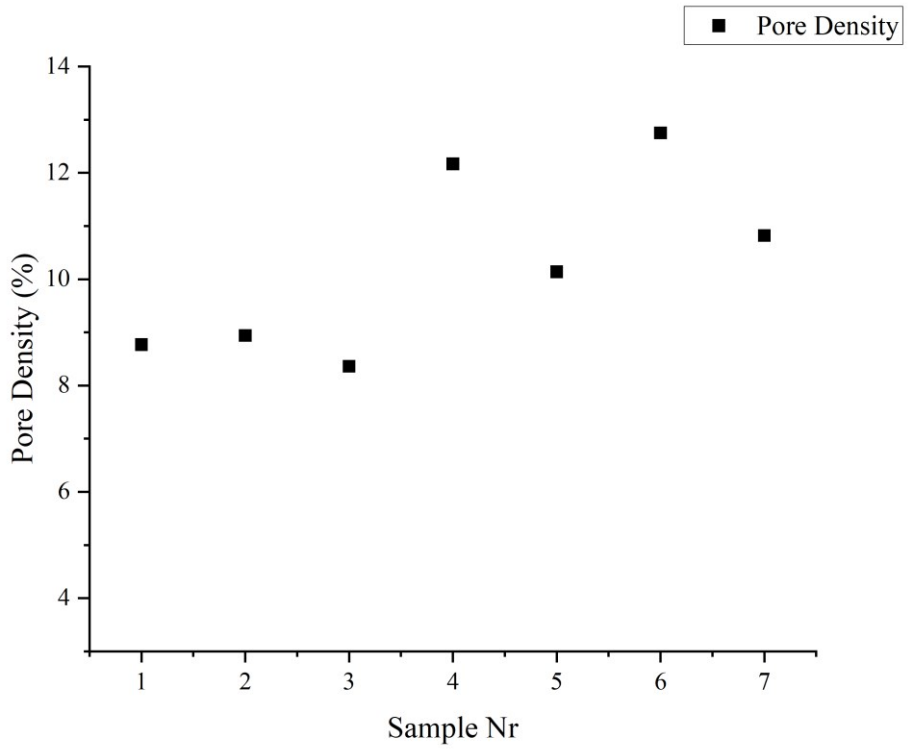

Figure 3.4 Trend of Pore Density of every sample.

3.2 CENTER POROSITY

The second part of pore analysis intends to consider solely the center of the specimens, in order to avoid the defective part with high porosity staying far from the corners of the specimens. Thanks to this strategy, good results were achieved that can represent in a better way the behavior of the sample under different printing parameters. As shown in Figure 3.10, the quality of the surface increase, and the number of pores decrease a lot with a significant improvement in the final results. Figure 3.11b, c, and d show an increase in porosity and defects compared to the other pictures; while in Figure 3.11a, e, f, and g the pores decrease, meaning an improvement of the sample density and consequently of the mechanical properties. Observing the images of the center, it is clear that the main type of pore are gas porosity and lack of fusion; but there are also some small cracks that start (Figure 3.5) from the supporting strucutre at the bottom layer. The data analyzed with ImageJ and Origin showed good and encouraging results. Compared to the "surface porosity", the Pore Mean (Figure 3.6) and Pore Interquartile (Figure 3.7) decrease a lot, confirming the trend detected by the pictures. The two ranges are respectively 30 -160 μm^2, and 20-45 μm^2. Moreover, the Pore Density (Figure 3.8) is improved with values in a range between 0,2-2% more or less, data very close to the full density reaching with the traditional production. As expected and reported in the graph of the pore mean, samples 1, 5, 6, and 7 have a smaller area of the pore than the other, and this is directly correlated to the better pore density of these. In addition, it is useful for the complete characterization and comprehension of the influence of the printing parameters to show the relation between the Energy Density and the pores of the samples. In Figure 3.9 and Figure 3.10 there is a clear visible trend with a decrease in the number of pores and an increase in the density of the pieces with an increase in the energy until sample 7. The number of pores starts from about 6500 and decreases until about 3500 according to the Pore Density. After sample 7, the number of pores of sample 6 increases a lot reaching a value of about 6500 similar to sample 2. However, there is a big difference in the porosity between these two samples, where one has 0,41% and the other 2.15% as it is observed in Figure 3.10. The graphs represent correctly the situation and the visible variation of the porosity between the specimens.

Furthermore, observing the center surface, a particular situation is detectable in sample 1. Inside the sample, there is a huge crack (Figure 3.12) from one corner to the other in the bottom layer, visible without a microscope. Sample 1 has also a very curious behavior because it is very evident the presence of a worse zone. The whole area close to the corners of the pieces and close to the top and the bottom corners is very porous. In particular, the first and the last layer, and also the whole zone into about 2µm starting from the corners (Figure 3.13) are very critical. In sample 1 the central zone is incredibly better than the boundary where the porosity is enormous.

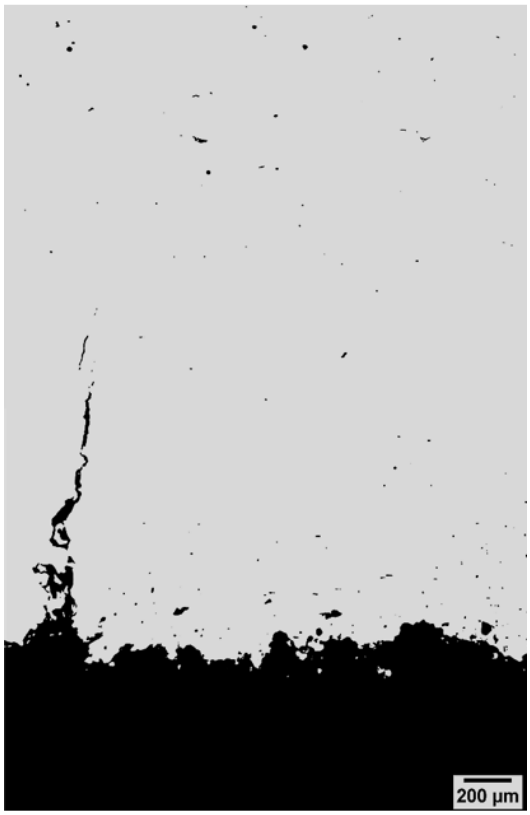

Figure 3.5 Crack that start from the bottom.

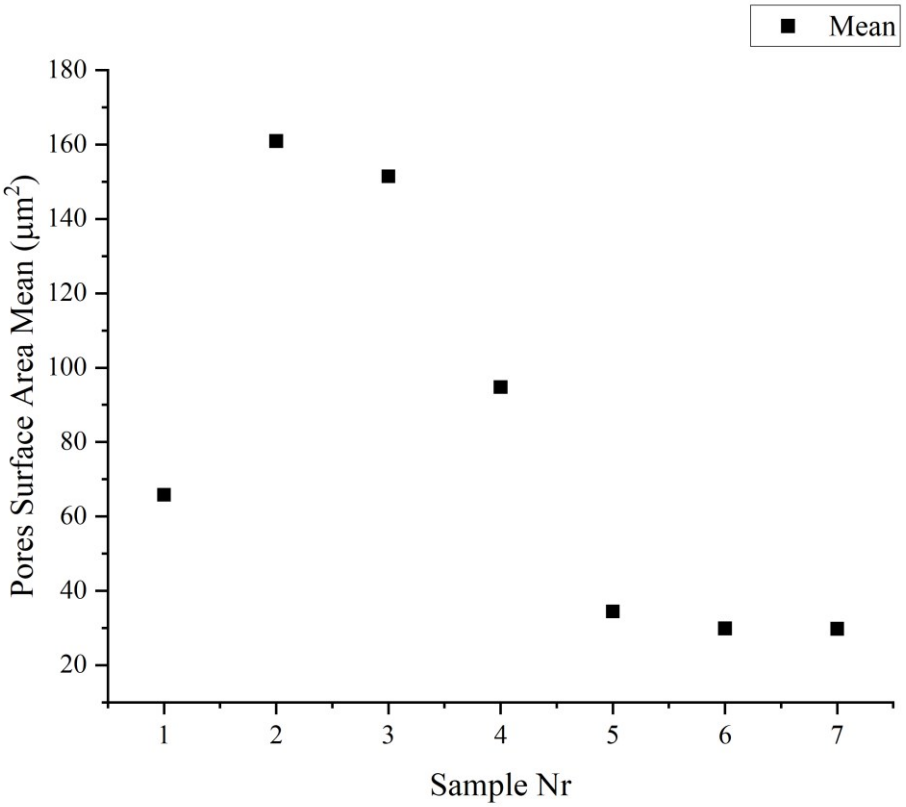

Figure 3.6 Pore Mean graph. Relation between pore size mean and sample number.

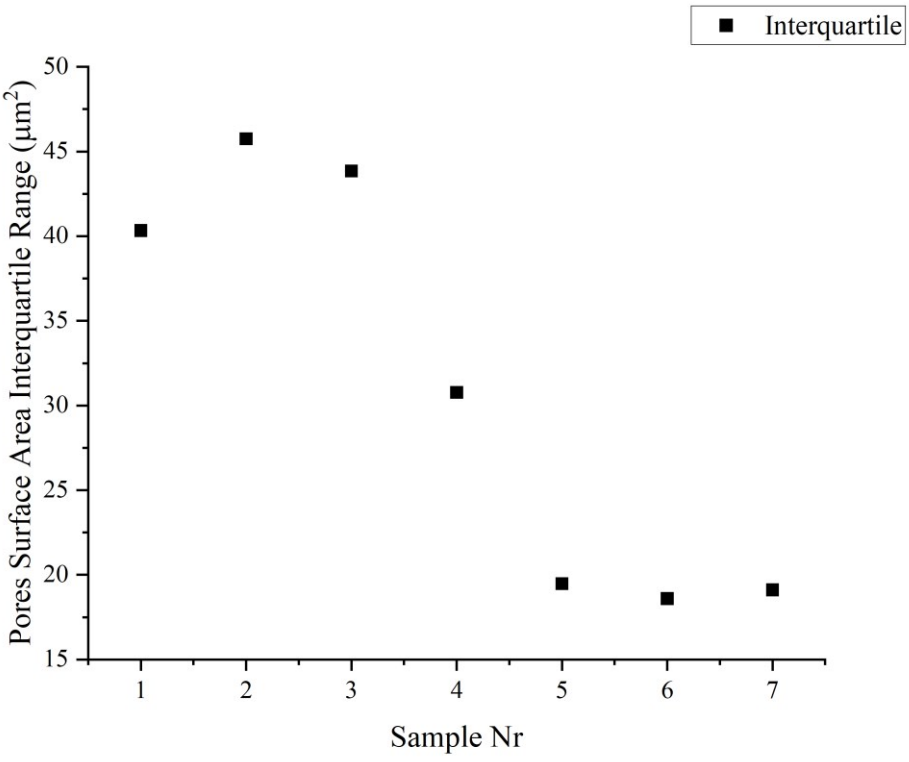

Figure 3.7 Pore Interquartile graph. Relation between pore size interquartile and sample number.

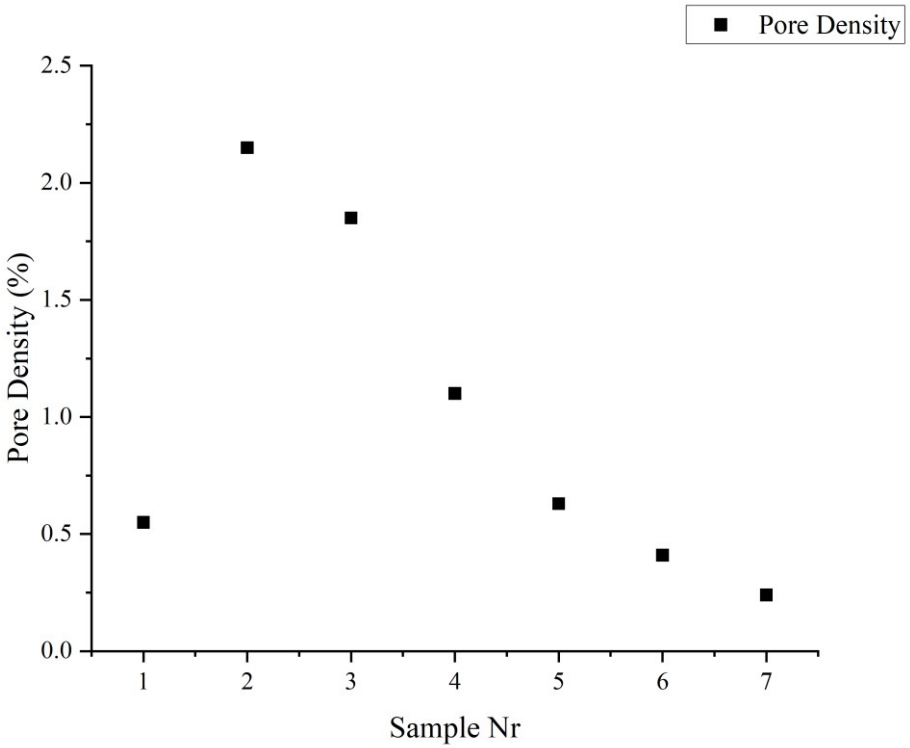

Figure 3.8 Pore Density graph. Relation between the pore density and sample number.

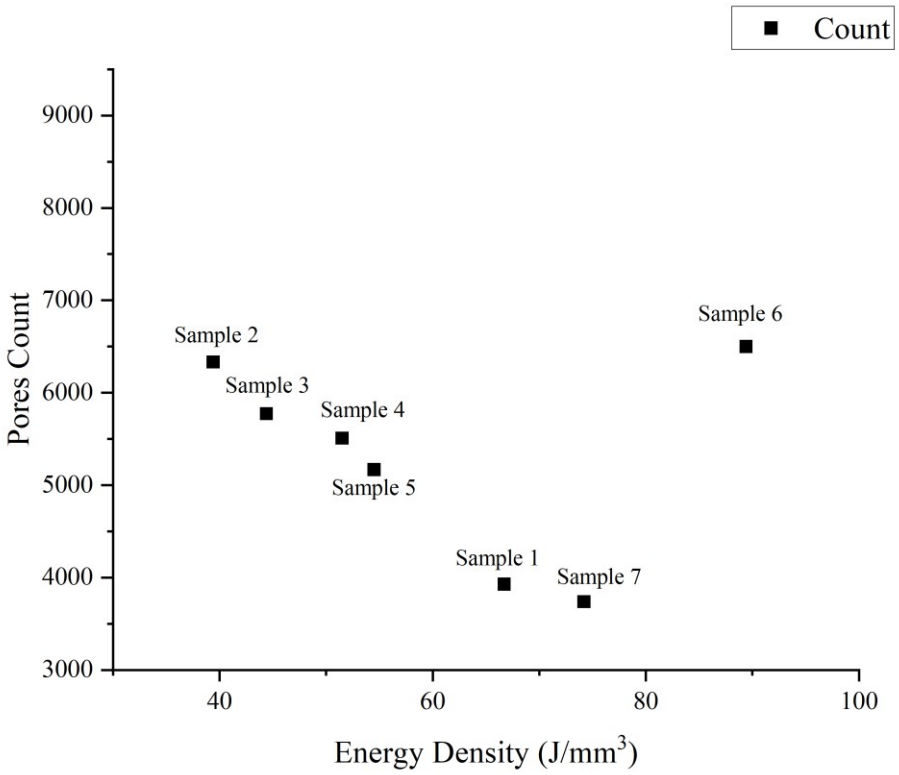

Figure 3.9 Relation between amount of pores and Energy Density.

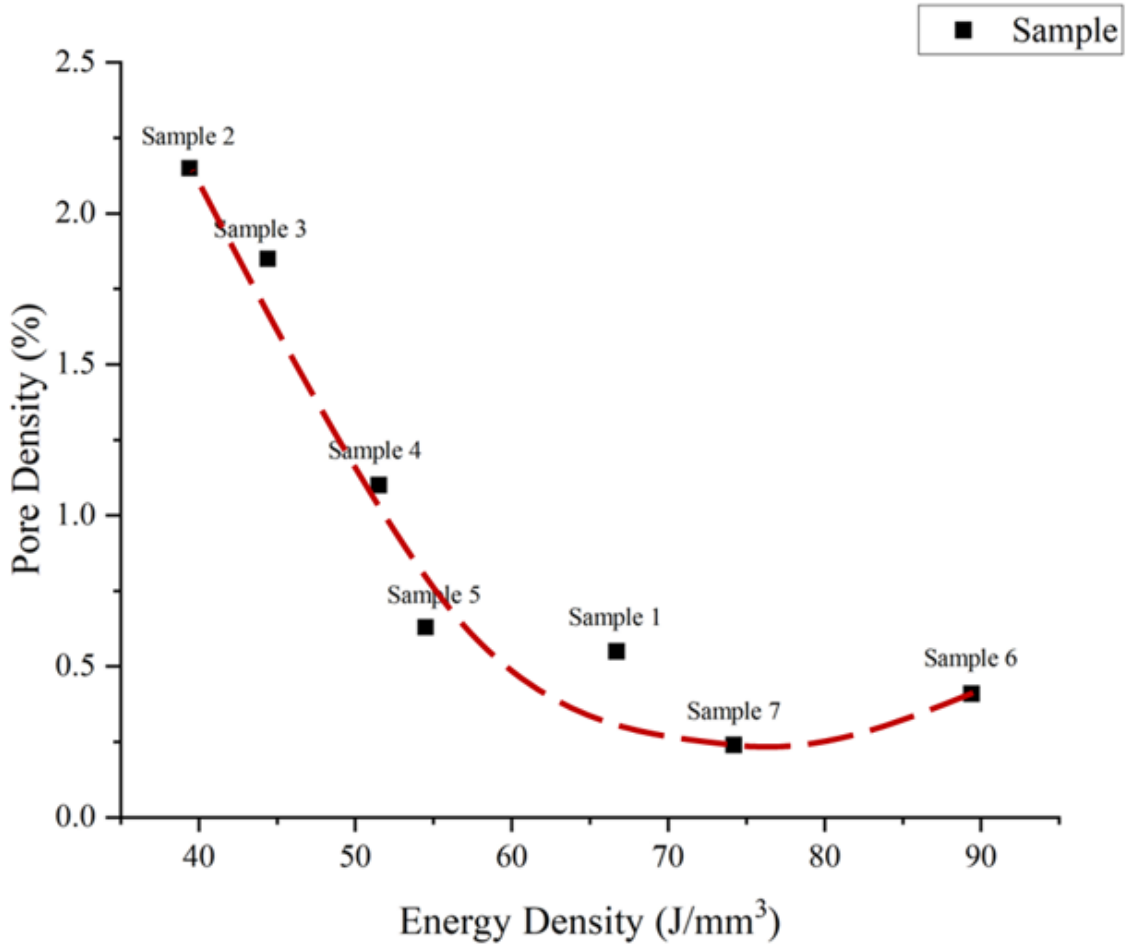

Figure 3.10 The graph shows the trend of the Pore Density compared to the Energy.

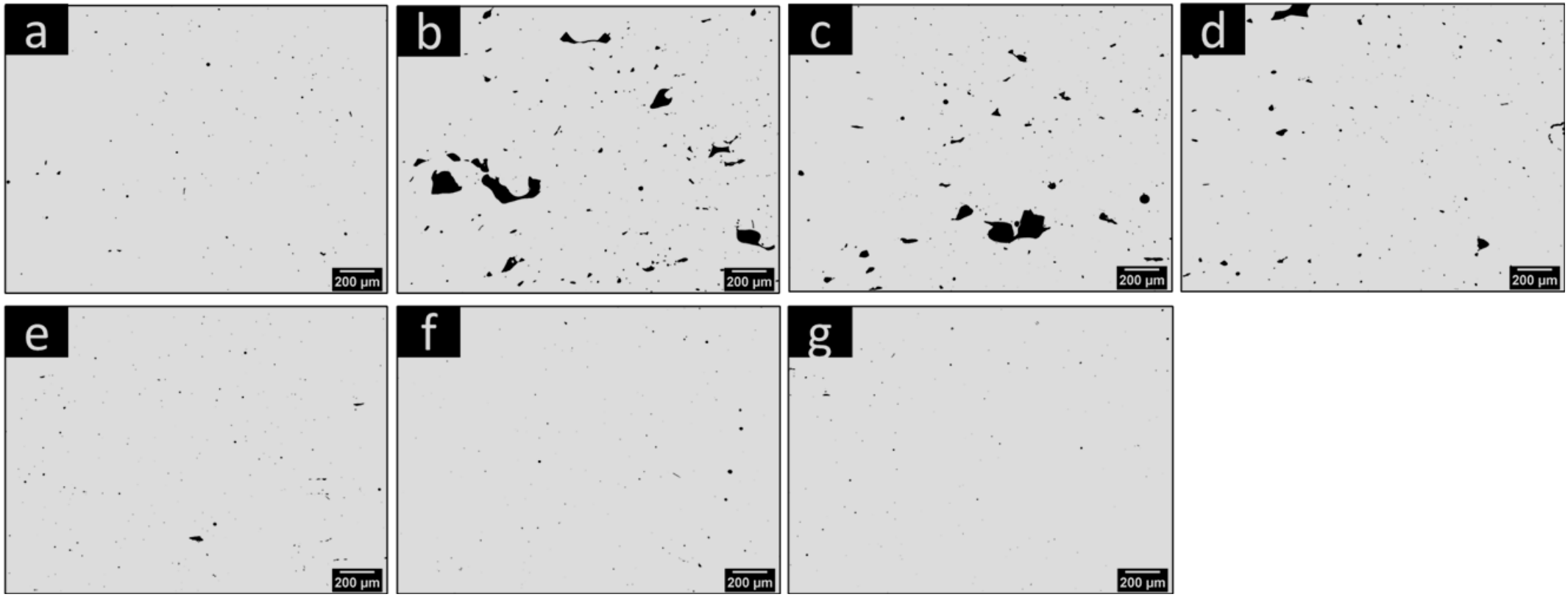

Figure 3.11 Center Porosity of every sample: (a) sample 1, (b) sample 2, (c) sample 3, (d) sample 4, (e) sample 5, (f) sample 6, and (g) sample 7.

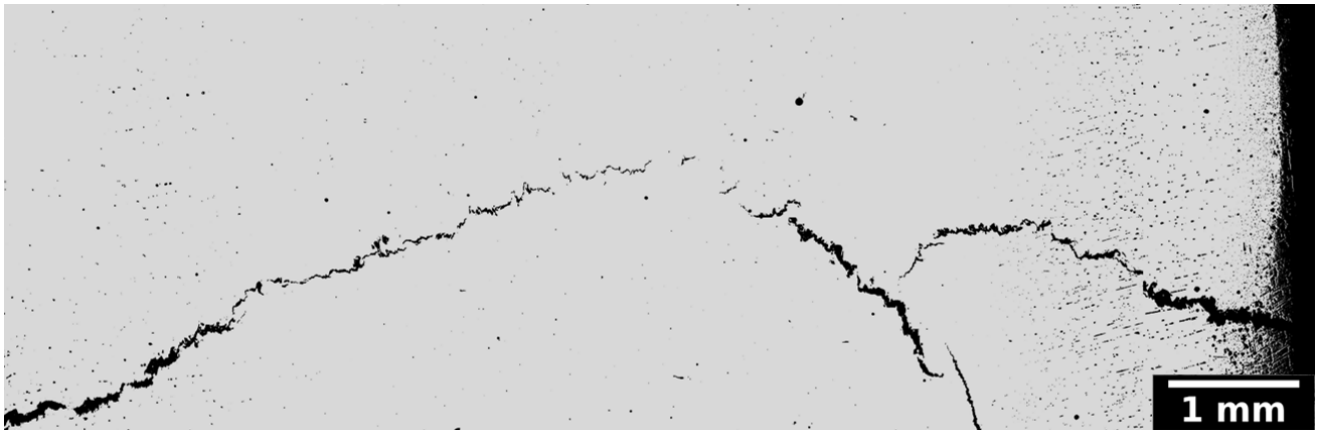

Figure 3.12 Collage of images to show the big crack in sample 1.

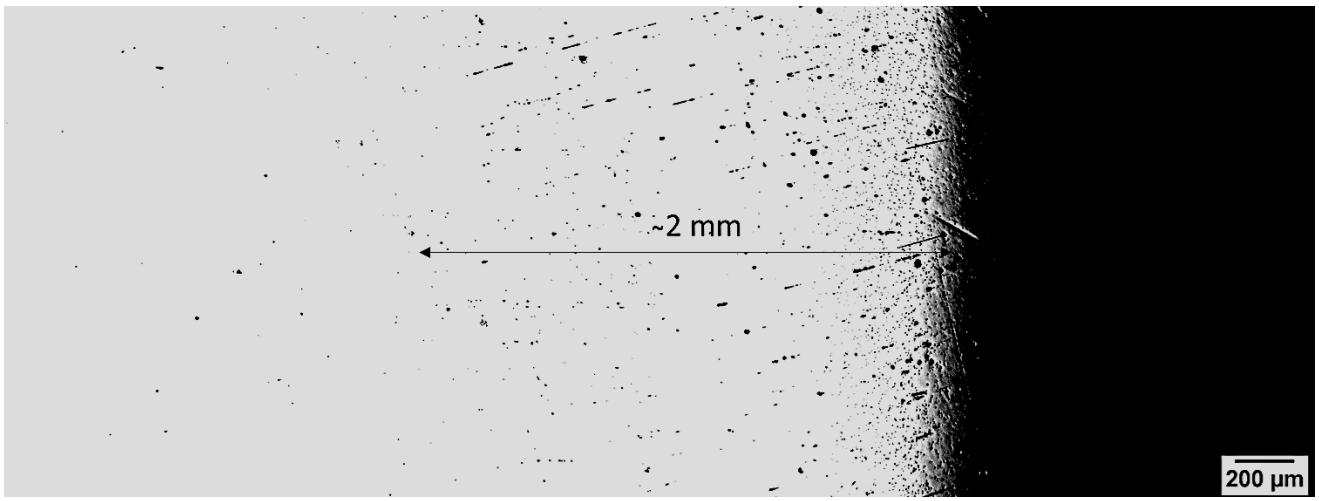

Figure 3.13 Representation of the bad zone close to the corner in sample 1.

3.3 MELT POOL

The analysis of the melt pool is another fundamental part to completely analyzing something printed, in order to try to find a correlation between parameters and shape or dimensions of the melt pools. In every sample, the melt pools are more or less the same. In particular, it is possible to see in Figure 3.16 the slight differences between every picture. Moreover, it is also clear that there is not a definite shape, but the melt pools are huge and quite flat. In some cases, it is also difficult to find the boundary of the melt pool and to identify the peak, which is characteristic of the laser passage during the printing. The characteristics of the melt pools change from one specimen to another. The clearest tracks are shown in Figure 3.16a, b, c, and d; while in e, f, and g, the boundaries are slighter and difficult to detect. There is a difference in the coloration of the center and the boundary of every melt pool. The height of the melt pools and the thickness of the layers change a lot during the printing process. There are variations from one layer to another, and this behavior is probably due to the power of the laser beam that remelts the previously deposited powder. Analyzing the graph in Figure 3.14 the value of height mean in a range of 60-90µm without big variation between the specimens. In addition, also the Interquartile shows in the graph of Figure 3.15 a similar trend in the melt pool height. Every specimen has a distribution of the values of the melt pool height in a range between 20 and 40µm. Only sample 1 is out of range with a major number of melt pools with a height of about 55µm.

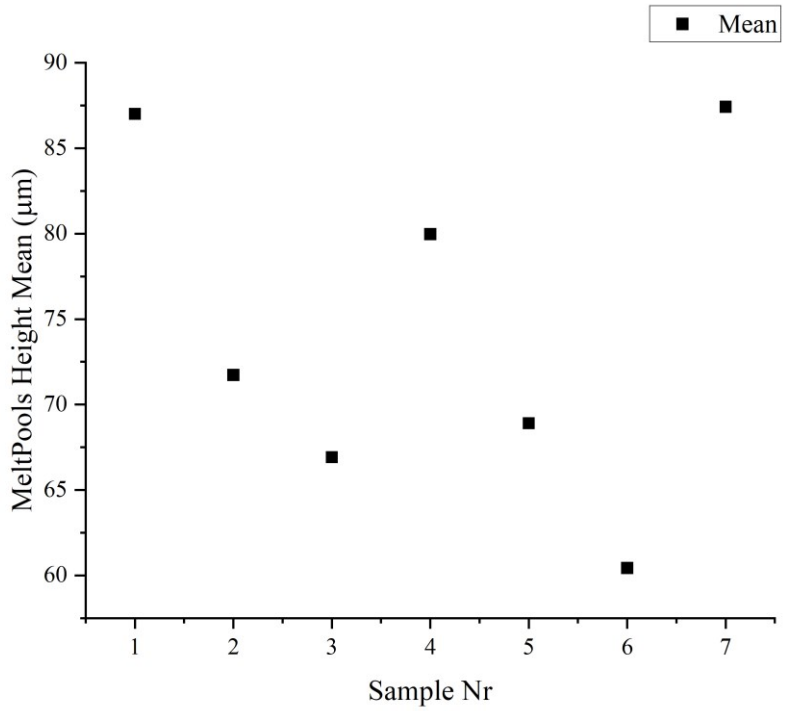

Figure 3.14 Pore Mean graph. Relation between pore size mean and sample number

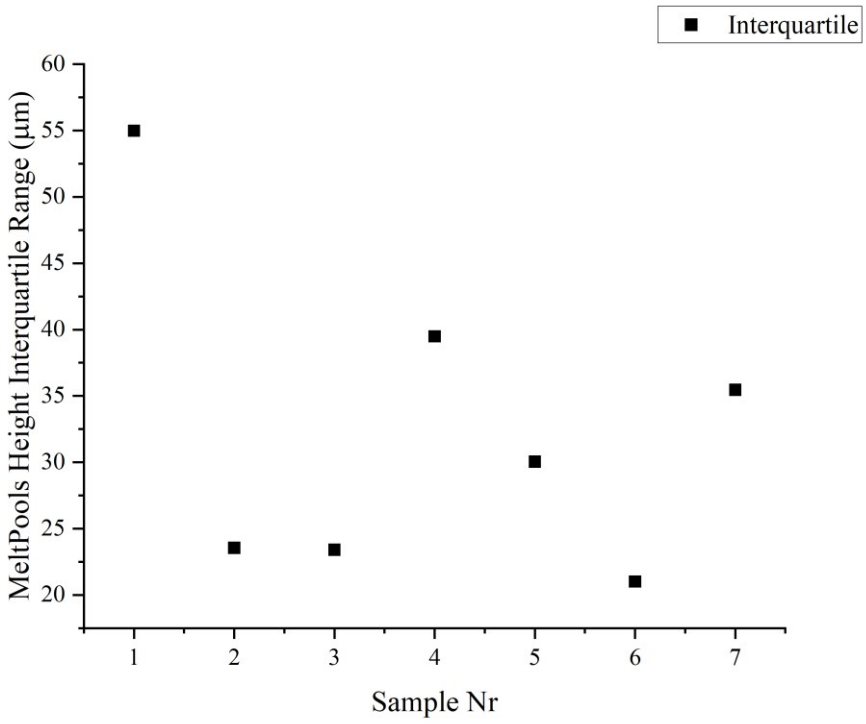

Figure 3.15 Pore Interquartile graph. Relation between pore size interquartile and sample number.

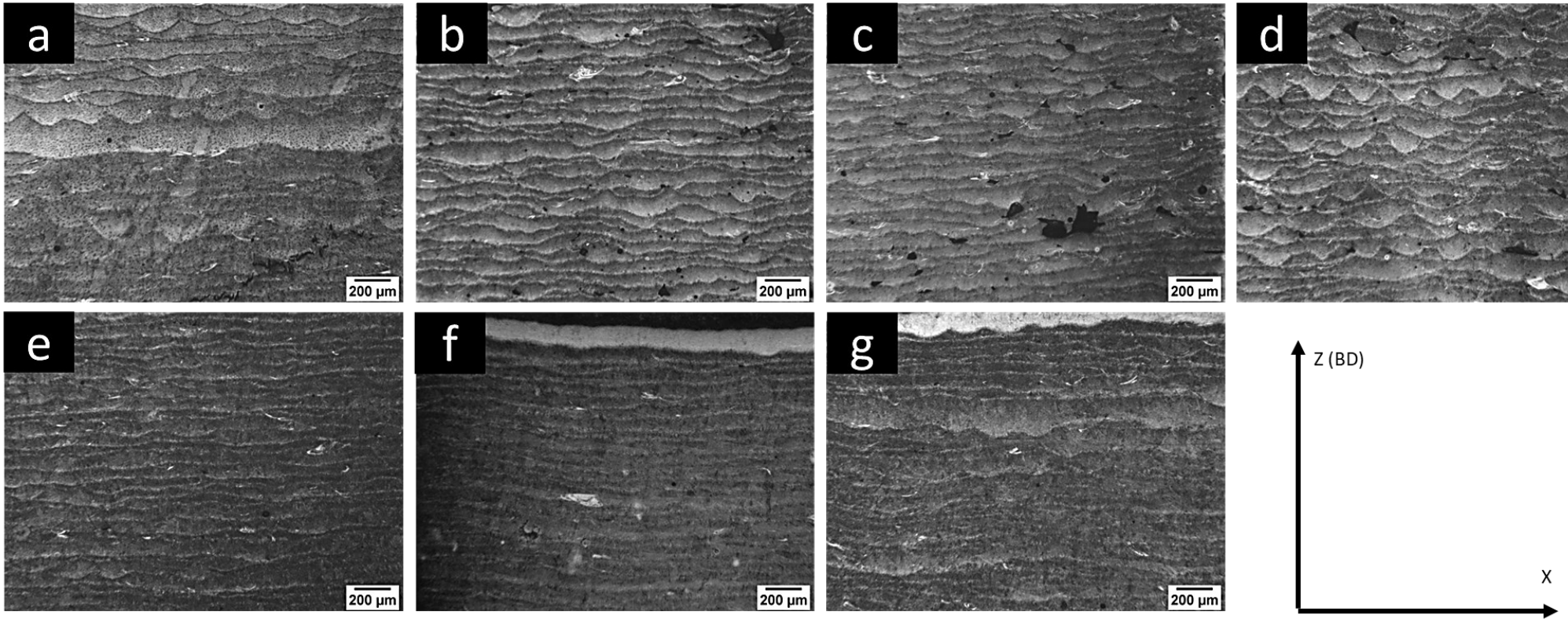

Figure 3.16 Melt Pool in trasversal section parallel to built direction of every sample: (a) sample 1, (b) sample 2, (c) sample 3, (d) sample 4, (e) sample 5, (f) sample 6, and (g) sample 7.

3.4 HARDNESS

The hardness test was done across the section of the sample with two line scans, one horizontal and the other vertical, every 0,3mm. For every specimen, the results are reported in the graphs (Figure 3.17) that represent the hardness behavior. In every measurement, there is an oscillation of the values, and this is probably due to several factors connected to printing parameters, scan strategy, heat transfers during the printing and the solidification, and porosity in the samples. Moreover, the influence of the boundary and the center of the melt pools could be a factor to take into consideration because, as it will be explained subsequently, there is a difference in the microhardness. From the graphs reported, it is possible to do some considerations about the behavior of the specimens. The hardness values fluctuate in a range of measurements because, at every point where the indentation is done, there is a different condition that affects the result. This test is useful to find a median value of the hardness for each specimen, in order to have a number to compare the as printed with the bulk. In Table 3.1, sample 1 has the higher value of hardness with a median of 546 HV; while the worst is sample 6 with 473 HV. Specimen 1 is unique with a hardness "out of range" because the others are more or less in the same range, even if samples 2 and 4 are a little bit above this interval with respectively 508 and 509,5 HV. Anyway, every tested specimen has a hardness value lower than the bulk at the same condition, which has an hardness of 670 HV.

In addition, another interesting thing is the trend shown in Figure 3.18, where the value of every single indentation becomes more compact and close to a common result along the entire line of scan when the porosity decreases. There is a closing of the range of values during the test becoming more uniform and constant, reaching a situation more stable, with fewer oscillations.

Sample	N° Total	Mean [HV]	Median [HV]
1	66	539.1	546
2	66	501.4	508
3	66	484.5	490
4	66	503.1	509.5
5	66	484.6	479.5
6	66	465.0	473
7	66	478.1	482.5
Bulk	-	670	670

Table 3.1 Mean and Median values from the whole measurement.

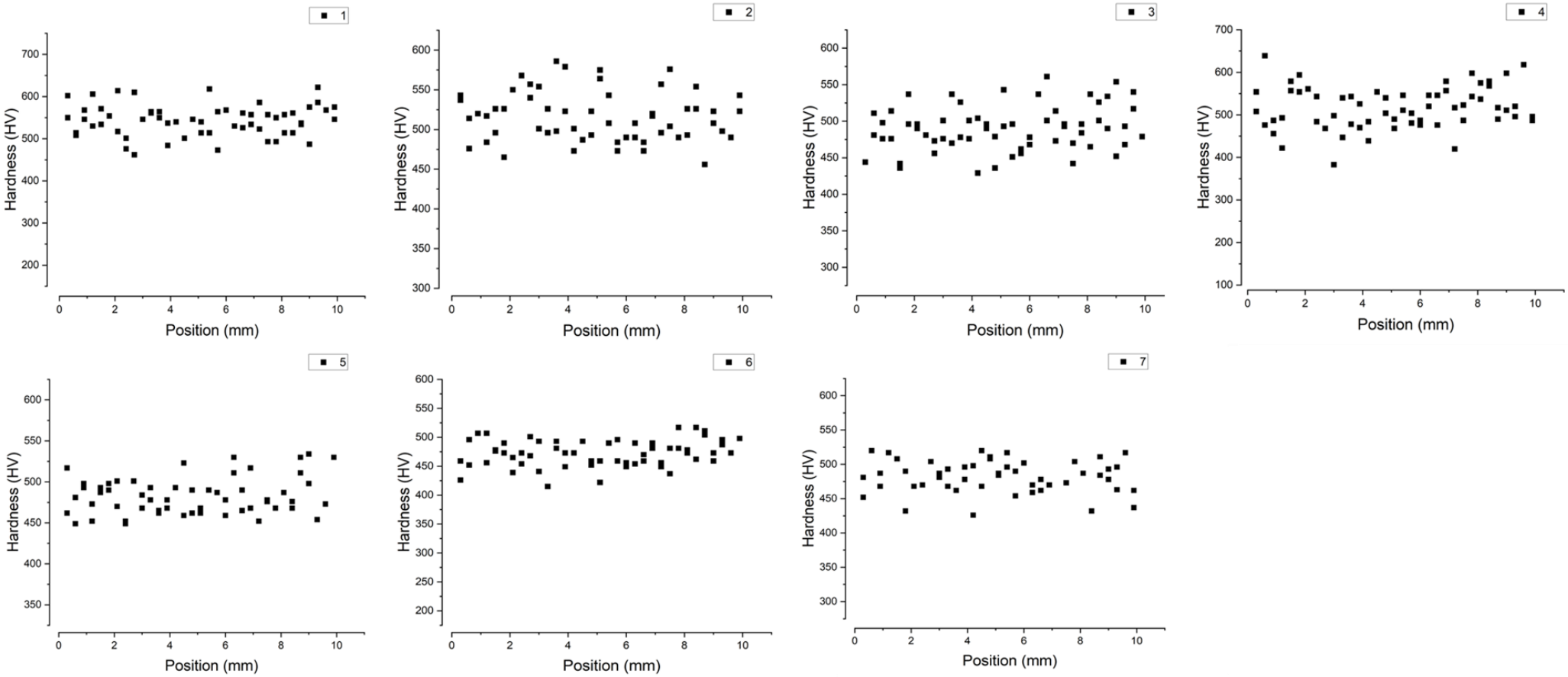

Figure 3.17 Summary of the hardness test.

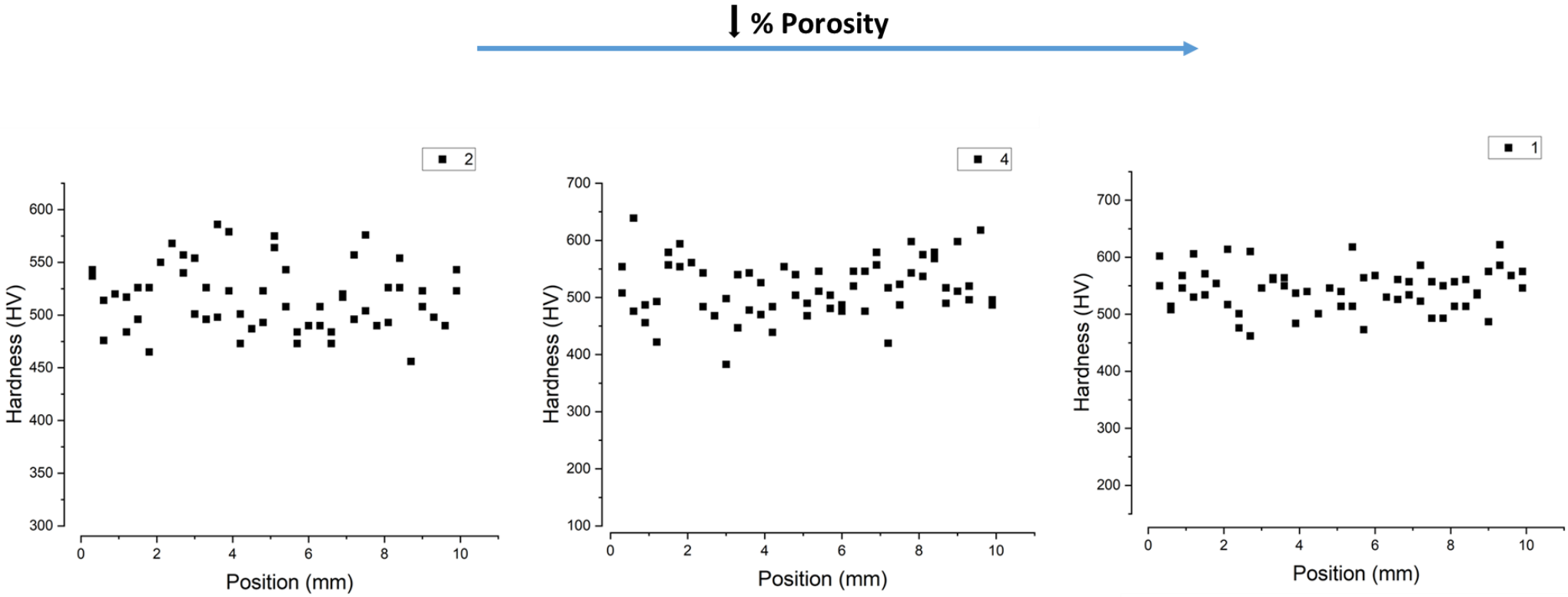

Figure 3.18 Behavior of the oscillation of the hardness test with the decreasing of porosity.

3.5 MICROSTRUCTURE AS PRINTED

The microstructure of a material is another important part of the characterization, and it can give information about the process and the mechanical properties. Firstly, it was observed the microstructure of specimens as printed to analyze if there were differences, segregations, or presence of impurities that could affect the final result. The SEM micrographs in Figure 3.19 provide insights into the microstructural feature of the specimens, showing a martensitic morphology due to the high cooling rate after the printing process. Observing the images it is also clear that the microstructures are similar highlighting that there is no visible inhomogeneity during the solidification. This analysis is exclusive visual based on a check of every specimen with the SEM, and this confirms that there are no substantial differences detected between printed steel and the bulk. Nevertheless, during the printing process happens decarburization in the regions circumscribed to the boundary of the melt pools. The SEM micrograph in Figure 3.20 detects two different zones, one darker (CZ) and one lighter (BZ), which are representative of a variation in carbon concentration. This condition will be supported also with other evidence in the next chapter. Finally, another interesting aspect is the presence of columnar grains highlighted by a special etching with fluoric acid (Figure 3.21). These grains were formed during the solidification and they have divided into a group with parallel orientation, distributed randomly in the microstructure with different slopes.

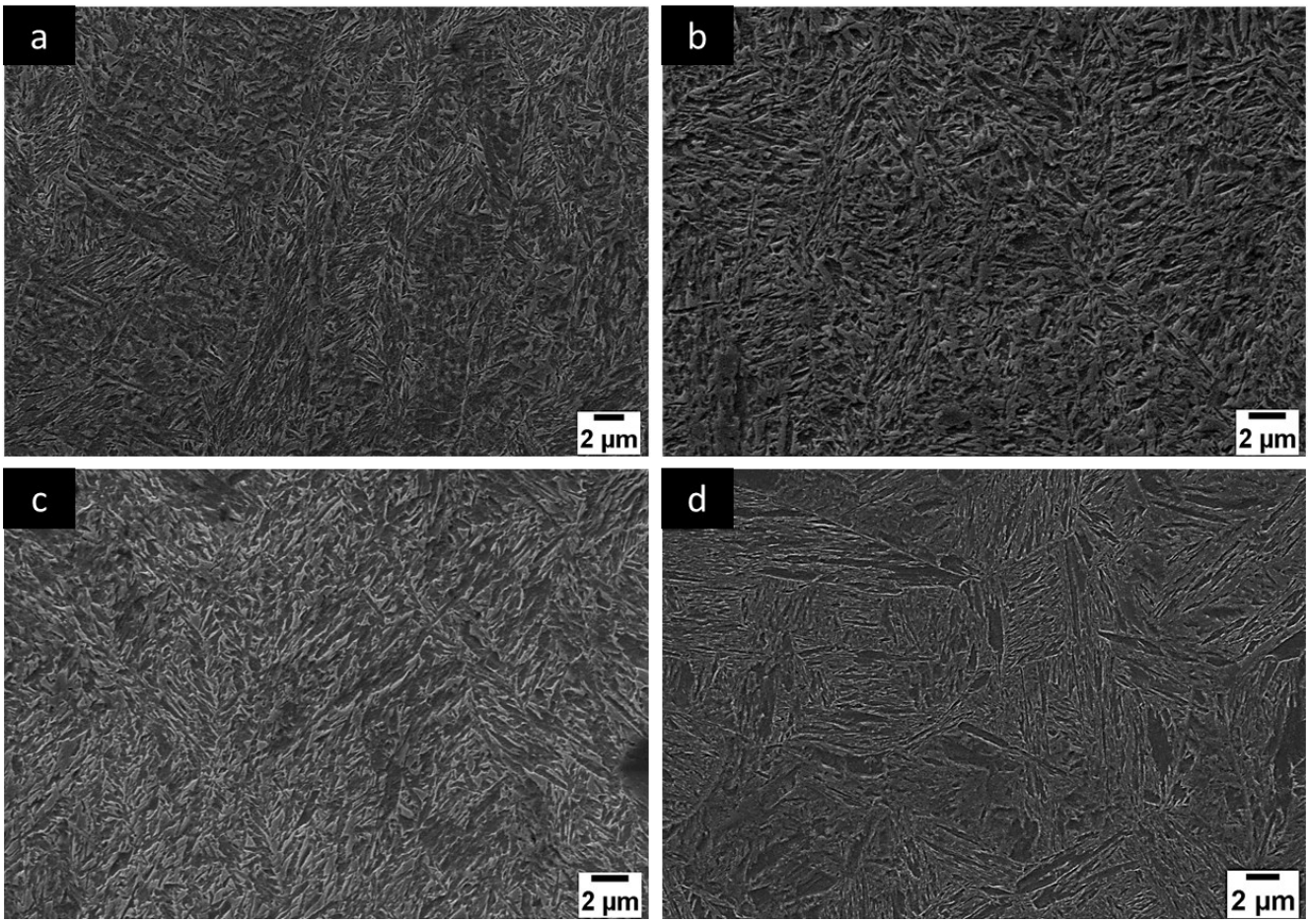

Figure 3.19 The SEM micrographs of martensitic microstructure. a) sample 2, b) sample 6, c) sample 7, and d) bulk.

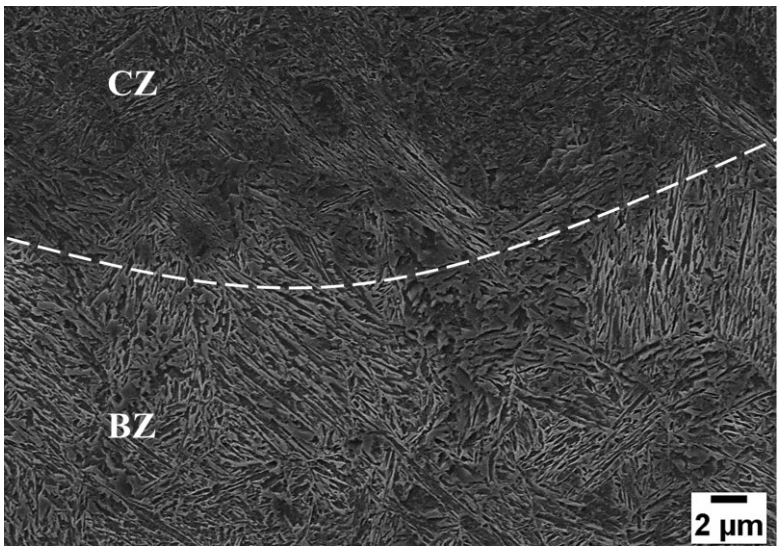

Figure 3.20 SEM micrograph of a melt pool. (CZ) central zone, and (BZ) boundary zone.

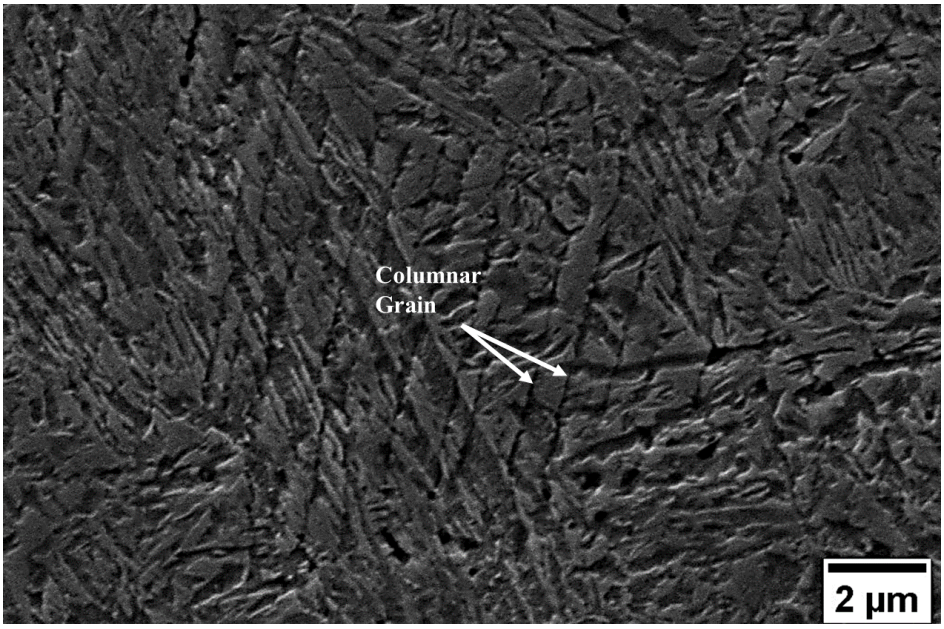

Figure 3.21 SEM micrograph of the columnar grains in a martensitic microstructure.

3.6 EDX MAPS

In Figure 3.22 is reported the results of the EDX maps done on the specimens, in order to better understand the microstructure and the full characterization. The results are practically the same in every specimen, and there are no significant differences or variations in the element compositions. The elements do not change from zone to zone, showing a situation of uniformity without difference between the as printed and the traditional material. In Figure 3.22, it is also visible that the presence of the defect observed in the EDX of the Fe, which is the more present element in the alloy. Considering the maps in Figure 3.23 of the printed material after the heat treatment, the results are uniform with the expectations, without difference or segregation, and the elements are uniformly distributed in the lattice.

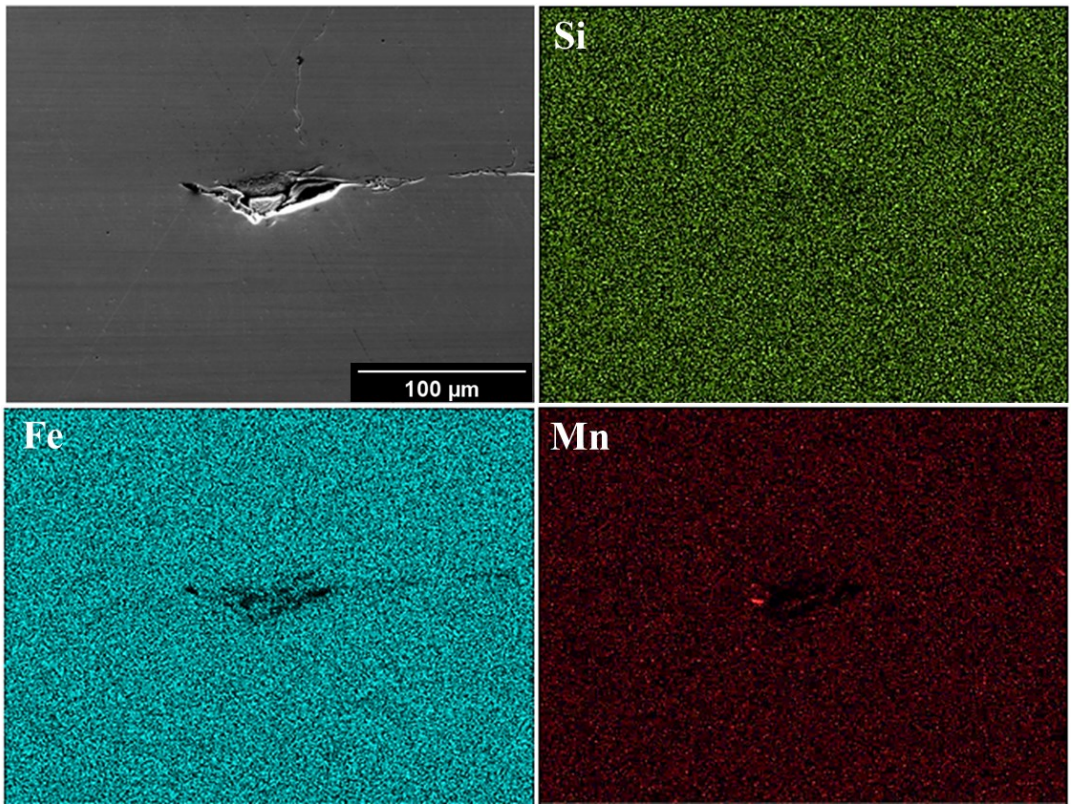

Figure 3.22 EDX Maps of the elements in the as printed material.

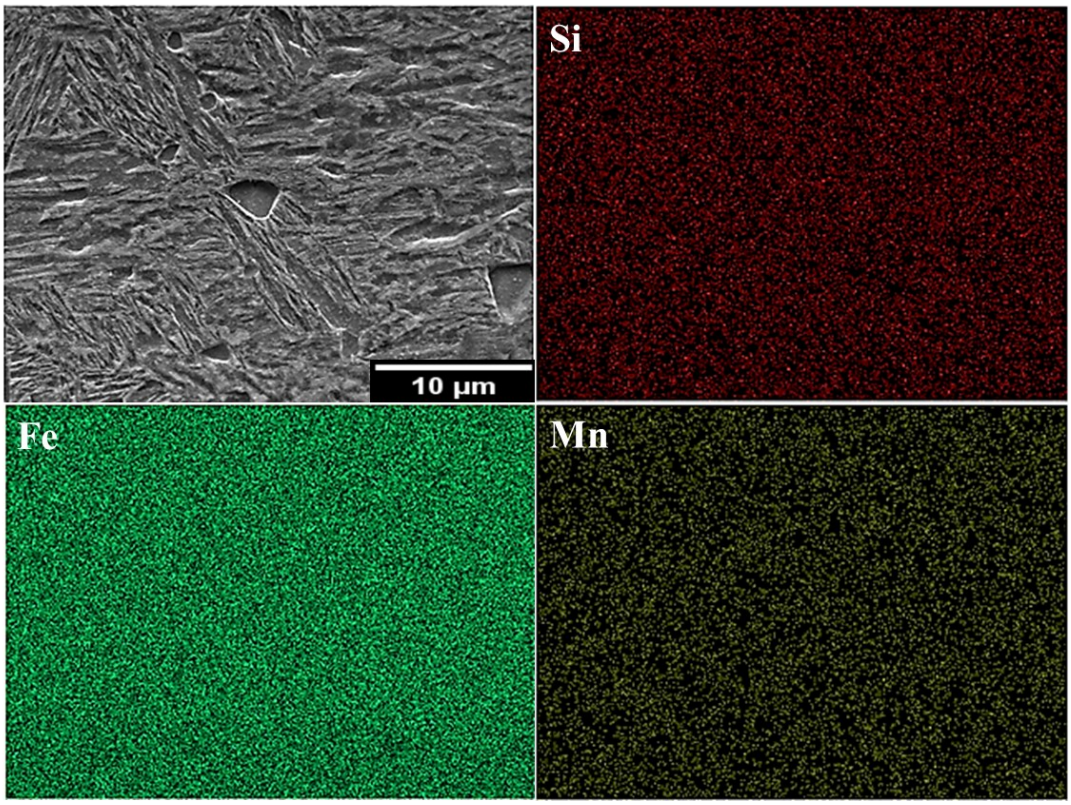

Figure 3.23 EDX Maps of the elements in the heat treated material.

3.7 HEAT TREATMENTS

During this study, several heat treatments were done to better understand the behavior of the specimens, and also to observe if there are inhomogeneities with the bulk and the classical strategy. The SEM micrograph in Figure 3.24 shows the bainitic microstructure after the heat treatment detectable in every specimen. Observing the image, the microstructure is very similar and finer than that reported in Figure 1.6, where the two morphologies of austenite and the ferrite plates are visible. This result allows to confirm that the behavior of a printed alloy is the same as that wrought under the same conditions of heat treatment. There are not huge differences and the microstructure is for the most part homogeneous. However, Figure 3.25 is reported a special case in which the behavior of the specimen is altered. The microstructure is not homogeneous, and there are singular zones where the ferrite becomes more rounded, a different shape from a ferrite plate. This behavior is also observable in a sample after annealing treatment (Figure 3.26), where it is clearly visible an area where the perlite is not formed.

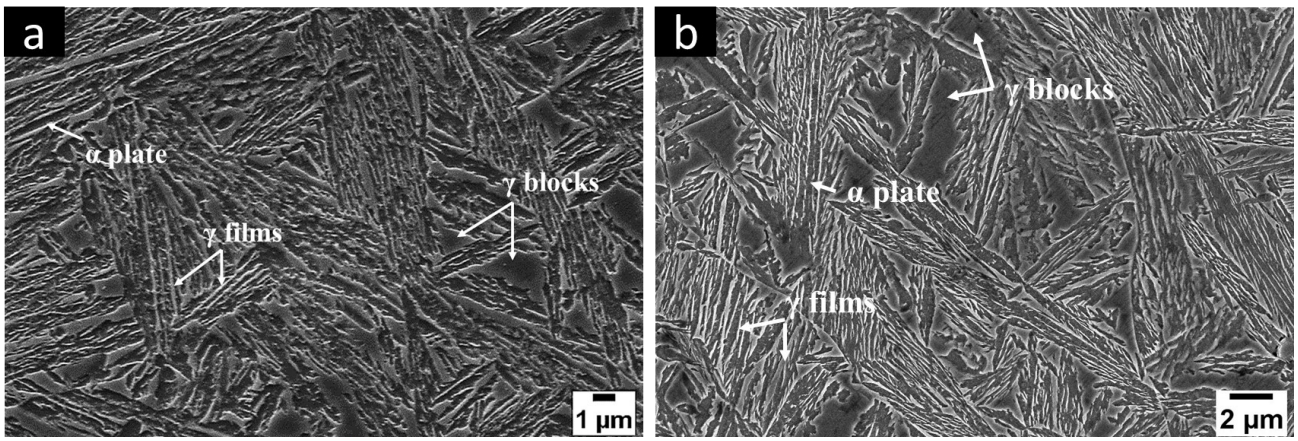

Figure 3.24 The SEM images of bainitic structure in every treated sample. a) printed material; b) bulk material.

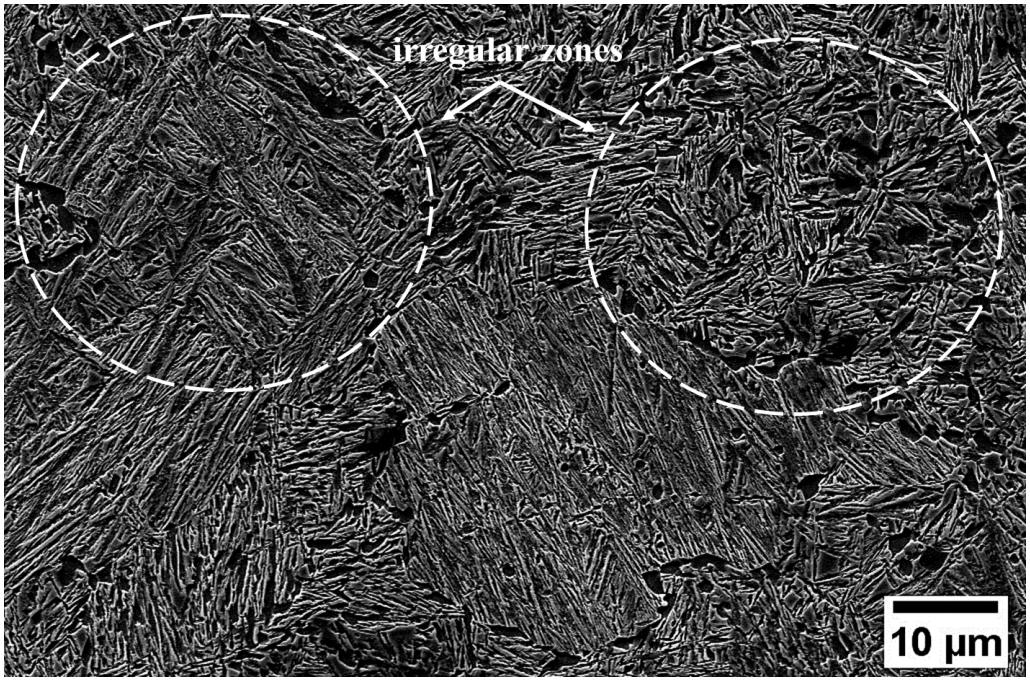

Figure 3.25 SEM micrograph of irregular zones.

Figure 3.26 Irregular zones in an annealed specimen.

3.8 DEFECTS

During the characterization of the specimens, several classical defects were found in the printed materials:

- Lack of fusion (Figure 3.27): voids and pores with the presence of distinguishable particles of powders don't melt.

- Gas Porosity (Figure 3.28): pores formed by gas entrapped into the melted material and these leave pores during the solidification.
- Decarburization and subsequent worsening of the heat-treated microstructure (Figure 3.25 and Figure 3.26): zone with different morphology concerning the correct heat-treated microstructure.
- Cracks (Figure 3.5 and Figure 3.12): the cracks should be of different dimensions and orientations, and they can start in random positions with a major probability in the bottom with a vertical direction. These are formed by shrinkages during solidification.

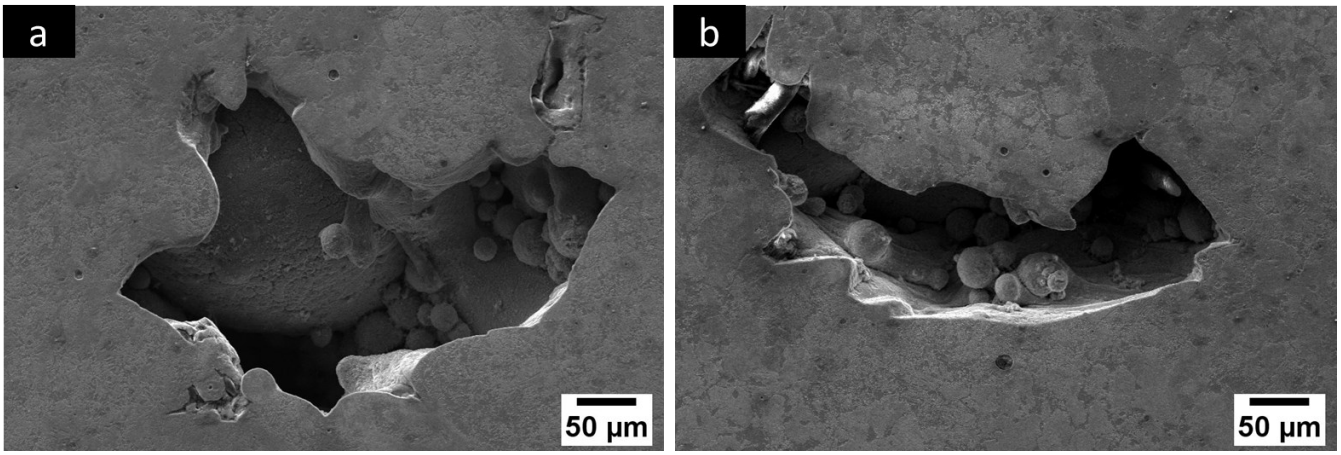

Figure 3.27 SEM images of two different lacks of fusion.

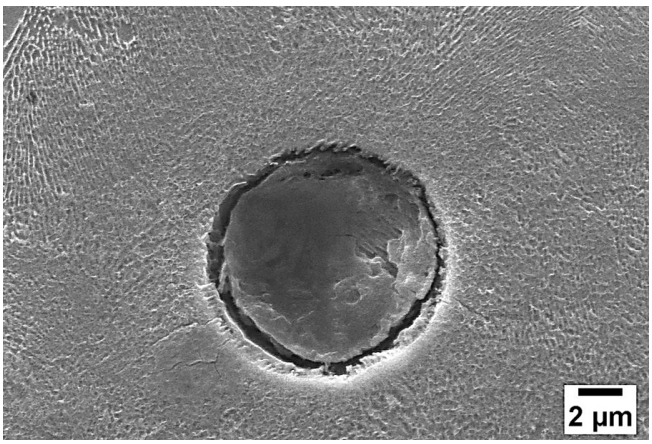

Figure 3.28 SEM image of an example of gas porosity.

3.9 XRD

Results of XRD analysis are reported in Table 3.2. As shown by the Rietveld refinement in Figure 3.29, both for the conventionally fabricated material and the LPBF fabricated, the microstructure consists of bainitic ferrite and carbon retained austenite, confirming the microstructural observations previously reported. In particular, about the conventional material, the presented carbon content is an average value, that considers both the filmy morphology and block morphology; in fact, during refinement, they were not distinguished. Concerning bainitic ferrite, Rietveld refinement leads to the demonstration of tetragonality and carbon supersaturation, at a level larger than those at the equilibrium, in agreement with Caballero et al. [37].

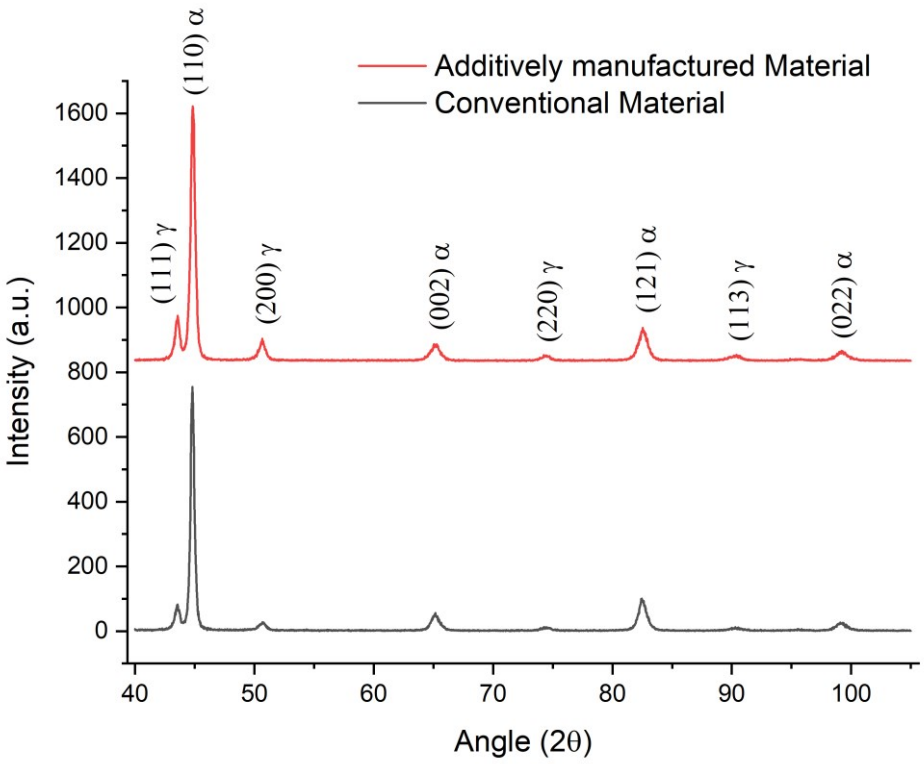

Figure 3.29 XRD diffraction of the conventional material and the L-PBF material after heat treatment.

Sample	Vγ (%)	Vb (%)
Conventionally fabricated material	25 ±3	75±3
LPBF fabricated	21±3	79±3

Table 3.2 Result of Rietveld x-ray diffraction pattern refinement.

The results reported in Figure 3.30 show a uniform behavior of every specimen as printed under the same conditions of the XRD test. The trend of the curves is more or less the same between every sample, highlighting that there are no critical differences between the piece formed by different printing parameters. Results of this XRD analysis are reported in Table 3.3. As shown by the Rietveld refinement, for every sample the percentage between ferrite and austenite is more or less the same with slight variations, with a value of about 15 ± 3% of retained austenite, and about 85 ± 3% of martensite.

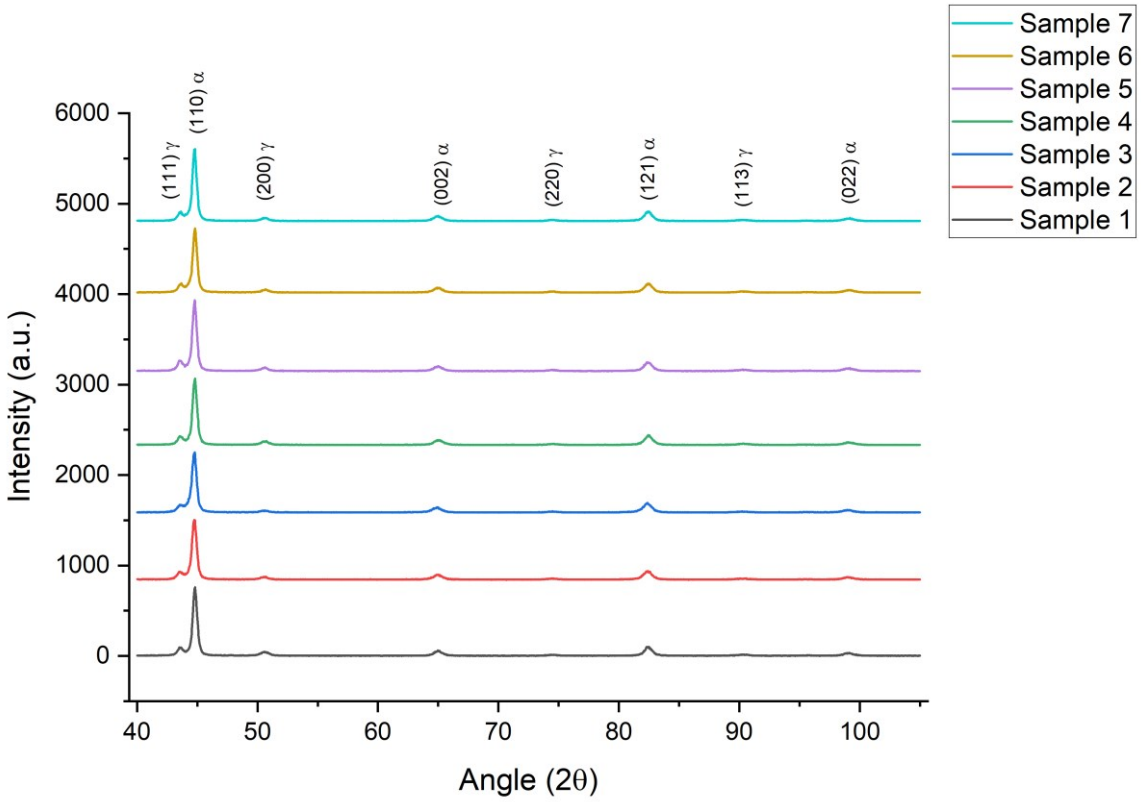

Figure 3.30 XRD diffractions of every specimen as printed.

Sample	V_γ (%)	V_α (%)
1	17.5 ± 3	82.5 ± 3
2	15.9 ± 3	84.1 ± 3
3	13.6 ± 3	86.4 ± 3
4	15.6 ± 3	84.4 ± 3
5	15 ± 3	85 ± 3
6	14.6 ± 3	85.4 ± 3
7	15.1 ± 3	84.9 ± 3

Table 3.3 Result of Rietveld x-ray diffraction pattern refinement. As printed materials.

3.10 EBSD

In Figure 3.31 are reported the two EBSD maps, respectively divided into the phases map on the left, and the orientations map on the right. These two are done on the transversal surface of the sample as printed, and the results confirm the previous data. In the phases map, there are represented two phases, alfa in red and gamma in blue, which are respectively the martensite and the retained austenite. The data from the XRD (Table 3.3) show a big difference between the phases, and the red color confirms this trend with an extensive presence in the detected area. Instead, the blu color is very low validating the 15% of retained austenite found with the XRD analysis. In the orientations map, it is visible the presence of different colors randomly distributed. This characteristic can suggest that the grains formed by the cooling of a printed part are equiaxial. There are no zones with the presence of grains with a directional growth or elongated along one single direction.

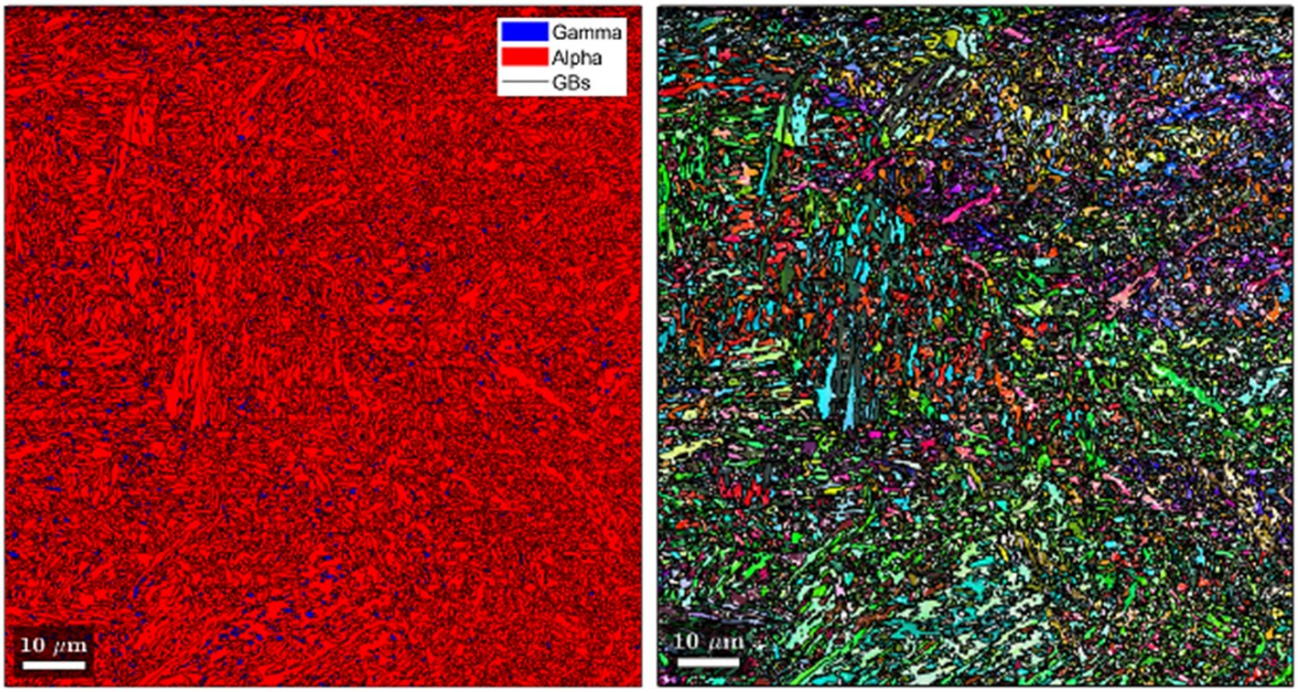

Figure 3.31 EBSD maps: Phases map on the left, and Orientations map on the right.

4 DISCUSSIONS

This chapter explains the data of the characterization of the specimens shown before. In particular, the discussion aim is the description and clarification of the obtained results, trying to understand the behavior of the samples under different printing parameters. This part is fundamental to connecting concrete data obtained during the experiments and the theory behind metal phase transformation, heat treatments, laser fusion, and solidification. Finding out possible theories is necessary to improve printing and achieve better results.

4.1 SURFACE POROSITY

As it is reported in chapter 3.1, the analysis of the surfaces is not useful for understanding correctly the situation and the behavior of every specimen under particular printing parameters. The variation of the pore density is strongly affected by the heat transfers and temperature gradients that are formed during the printing process and subsequent solidification. The external surfaces are variable and not representative. During the solidification, the heat transfer near the corner is different and higher than the center and the cooling is not uniformly distributed into the pieces. For this reason, the external surface seems to be more porous because the melted material does not have much time to aggregate and solidify more densely. Another probable reason for this behavior could be the printing process. The laser path is not able to melt correctly the powder near the corner, creating a structure with a huge number of pores and defects, which affect the density and the surface quality of the specimens. Therefore, it is necessary to not consider this part for the evaluation of the results given by the printing parameters. In fact, as reported in several papers [24–27,38], every specimen was cut and studied in the internal part to avoid the altered surface.

4.2 CENTER POROSITY

As it is possible to see in the figures of chapter 3.2, the situation of the pores is very different from the surface to the center, and this represents better the real behavior of every specimen under different printing parameters. In the center, the heat transfers and the temperature gradients are more uniform, and this allows for a denser area than the surface. This behavior is clearly visible in sample 1 as reported in Figure 3.13, where there is a zone near the boundary in which the porosity is bigger, decreasing going away from the corner. In addition, also Figure 3.12 shows a defect, a huge crack that is formed by a probably different solidification rate between the bottom and the center. The inhomogeneous cooling between the center and the surface during the whole printing process creates

shrinkages that generate cracks and other kinds of defects. In fact, in all specimens, there is a crack that starts from the bottom near the supports (Figure 3.5).

Analyzing the data obtained by the experiments and characterization of the specimens, it is possible to detect a trend between Energy Input Density, Pores Count, and Pores Density (Figure 3.9 and Figure 3.10). Increasing the Energy, there is a decrease in the number of pores and in the pore density due to probably a better melting of the steel powder. These behaviors coincide with the trend observed in other papers [23,24,28,38]. There is a strong relationship between these two parameters, and it is useful to use the Energy Density for enhancing the quality and the density of the specimens. The densification of the material is improved because the power is enough to reach a good level of powder fusion, decreasing the presence of lacks of fusion and gas pores that affect the final count [21,22,29]. However, there is a behavior detected in the experiment data and in the previously cited papers, in which there is a point of trend inversion. Above a particular value of energy, the pore density starts to increase. This phenomenon is due to the too high energy density that could cause the vaporization of the low melting elements with the production of keyholes, which can get worse the porosity enhancing the number of pores [38]. Even if Sample 6 has the highest value of pores, the density of the piece is high and this is because keyholes cause the formation of gas pores which are smaller than the lacks of fusion observed in Sample 2 which has the same number of pores.

The printing parameters have an important role in the realization of a quality piece and changing a single value could modify the kind of porosity, density, and melting of powder. The defects observable in Figure 3.11 are addicted to the parameters chosen previously. When the Laser Power, and subsequently the Energy Density, is too low, increases the presence of defects such as lakes of fusion (Figure 3.11b, c, and d). The power of the laser is not sufficient to completely melt the material and there is the formation of voids with particles inside (Figure 3.25) [21]. Another parameter that can affect the printing process and the final result is the Scan Speed. It is fundamental to connect this with the other parameters in order to achieve the best quality of the piece. A velocity too high can create problems with the melting if the laser power is high enough, forming voids and not fused powders, with the formation of defects like lack of fusion; while there is the opposite effect in case of a speed too low, getting a melted surface due to the excessive fusion of the material and with the formation of keyholes [21,22]. In addition, observing the data from the graph in Figure 3.6 gives important information about the printing process and the parameters. Samples 1,5,6, and 7 have the lowest mean size of the pores, and this is due to the higher Energy Density than the other specimens. This trend is due to the fact that a high Energy Density can melt the powder in a better way avoiding void defects

such as lack of fusion, which are bigger than voids created by gas. This behavior is also confirmed by the pictures of the specimen's surfaces in Figure 3.11.

4.3 MELT POOL

The melt pools in Figure 3.16 have a classical scheme typical of an L-PBF process, where it is visible the laser path and the single layers for each pass. To analyze the melt pools it was necessary to use a diluted etching, less aggressive because the alloy does not resist in a corrosive environment with a high rate of corrosion and damage. The etching is useful to highlight the boundary of the single melt pools and study their dimensions. Firstly, it is visible that the melt pools have a shape different from the classical scheme observable in other printed materials [21,38–40]. These are flatter and larger, the peak of the melt pool boundaries are less marked, and in many of these, it is difficult to distinguish them (Figure 3.16f, g, and e). This behavior is probably due to the higher laser power that melts the material too much, and in every pass, it affects also the previously deposited layers decreasing the thickness and melting the surrounding zones. Secondly, analyzing the images in Figure 3.16, it is detectable in a situation where there is a difference between the center and the boundary of the melt pool. There is a variation in the color of the microstructure after the etching due to a different reaction of the zones. This behavior is due to multiple thermal cycling effects during a subsequent material deposition where the material is exposed to high temperature, leading to the formation of two zones [23]. The regions in the boundary of the melt pools are subjected to a heat treatment due to the laser pass, and this creates a tempered zone; while the region in the center is exposed to a high temperature above the critical point, generating an untempered zone [23]. In addition, there is also a probable difference between the center and boundary in the carbon concentration of the microstructure. During L-PBF the powder is quickly heated and molten, and the atoms of carbon are more reactive with oxygen atoms at higher temperature [41]. The reaction between these two atoms occurs in the boundary of the melt pool with the formation of CO(g), resulting in a gradient from the molten pool center to the boundary with a process of decarburization [41]. Therefore, at the end of the melting process there is a “carbon-depleted zone) in the boundary and a “carbon-rich zone” in the center [41], confirmed also by the SEM picture in Figure 3.20 with different brightness. This theory is also confirmed by the micro-hardness test performed on the different regions. The test shows a variation in local hardness (Table 4.1), with a higher value in the center and a lower value in the boundary as is also reported in the paper previously cited [23].

Boundary [HV]	Center [HV]
440	490
436	502
447	483
453	491

Table 4.1 Hardness Test on MeltPool boundary and center.

4.4 HARDNESS

The results obtained in Table 3.1 by the microhardness test are positive, but they reach a value much lower than the hardness of the wrought material with a martensitic microstructure (670 HV). This difference is attributed to possible heat treatments and decarburizations that can affect the microstructure during the printing, as explained before. In addition, also the porosity can modify and worst the hardness resistance of the specimens. For the comparison is considered the median of the measurements to better represents the behavior of every specimen, because it does not use the data too far from a similar range of values which can be caused by measurement errors. Sample 1 is the only specimen with a performance very different from the others with a microhardness median of 539 HV. This mechanical response could be due to the heat treatments during the printing process such as quenching, and the microstructure gives a response higher than the other specimens. The test was performed by in total 66 imprints every 0.3 mm in order to take into consideration also the pores and to obtain a true representation of the material hardness with a porosity higher than the fully dense material produced by classic methods [30,38]. The scan strategy followed two lines, vertical and horizontal as reported in Figure 2.5, to verify the behavior of a printed material [42]. The results show that the microhardness is directionally independent because the reported values in Figure 3.17 are the measurements altogether, and these are similar and quite uniform. In addition, analyzing the graphs in Figure 3.17, there isn't a clear trend between the evaluation of the porosity and the median of the microhardness, and the variations of microhardness seem to be independent of the porosity. Instead, observing the graphs in Figure 3.18 it is possible to see a trend in the microhardness values where there is a closing of the range of the reported data passing from a higher porosity to a lower. The reduction of the fluctuation of the values of every specimen is due to the decreasing of porosity and a denser e more uniform material. The pores can affect the measurements, leading to a greater variation in the results of every single indentation [30,38]. Decreasing the porosity of the specimens increases the uniformity of the data with values more stable due to a denser material with a better mechanical response.

4.5 MICROSTRUCTURE AS PRINTED

The microstructure is another fundamental term for the evaluation of the quality of the printed material concerning the wrought material. Ensuring a correct microstructure is the first important thing, and this can give information on the printing process. Analyzing directly the micrograph Figure 3.19 of the specimens as printed, it is possible to observe that the morphology is the same as the alloy realized classically. The microstructure is martensite due to the rapid cooling during the printing process, and the only slight difference is that seems to be finner. This behavior does not create complications and does not modify the properties as confirmed by the microhardness test. Analyzing Figure 3.21, the columnar grains are visible and representative of the printing process because the growth is directional and influenced by the built direction [21].

4.6 EDX MAPS

The analysis of the distribution of the elements using EDX has shown a uniform partition in the piece. There are no segregation or particular variations that can affect the material, and the quality is not altered by the printing process and the subsequent heat treatment. The main elements such as Fe, Mn, and Si do not change and this is a good result because there is no leak of these elements during the process and heat treatment. In Figure 3.22, the trace of the defect that represents a lack of fusion is characterized by a dark imprint due to the absence of the Fe in this zone. Instead, in Figure 3.23 the presence of zones where the bainitic microstructure is not perfectly uniform, with the presence of a ferrite island not formed, is not influenced by a inhomogeneity or a difference in the distribution as it is clear in the EDX maps.

4.7 HEAT TREATMENTS

The heat treatments are one of the main aspects to take into consideration because if the result is not satisfactory, the alloy is not useful for the achievement of the final purpose. Studying the behavior of the printed material under heat treatment can give also information about the quality of the printing process. The microstructure obtained in Figure 3.23 is perfect bainite, with classical morphology in which there are ferrite plates and retained austenite in form of film and block [1]. The final microstructure seems to be finer than that observed in every classical bainite [1], and so there is no drastic difference between the two processes. This confirms the good quality of the printing process and the possibility to realize pieces with this strategy, reaching good quality. The heat treatment is the same used on the bulk material, with the same timing and temperature. To fully analyze the behavior of the specimens, several heat treatments are processed on these, and the results are the same

for each one. Nevertheless, there are problems in the microstructure as it is possible to detect in Figure 3.23 and Figure 3.24. There are zones where the morphology is not uniform and different from the correct structure. It is impossible to observe the classical bainitic ferrite and the shape is completely different. In Figure 3.23 the microstructure is formed by zones of bainite and irregular zone, suggesting that there are complications during the heat treatment, and the microstructure does not respond correctly to the process. Trying also other treatments as in Figure 3.24, where annealing is performed, the microstructure presents the same behavior, forming irregular zone randomly localized in the piece. Analyzing this phenomenon, the main cause is probably the decarburization that happens during the printing process [41,43] as explained in the previous paragraph. In addition, decarburization can happen also during heat treatment because it is inevitable that the furnace atmosphere contains oxygen [44]. Therefore, due to the chemical potential of carbon, this will be removed from the steel by decarburization [44]. The depth of the decarburization depends on the duration of heat treatment, and it affects the microstructure of the external and adjacent layers as it is possible to see in Figure 4.1.

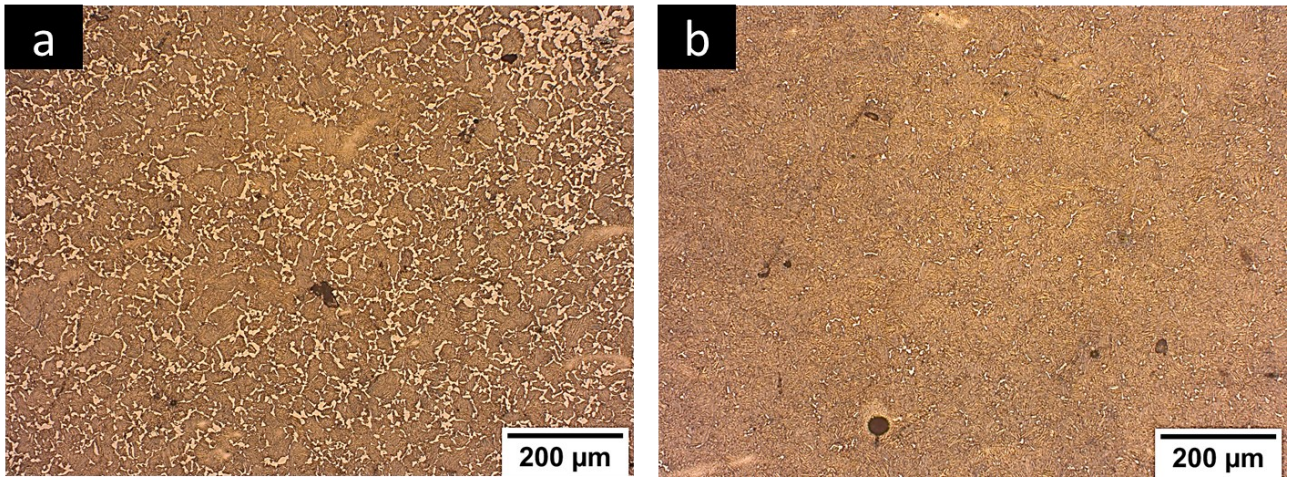

Figure 4.1 Images of a heat-treated sample with different levels of decarburization: a) layer more external; b) layer more internal.

In Figure 4.1a the level of decarburization is high because this layer is near the external surface, and it is exposed to oxygen during the heat treatment. Instead, in Figure 4.1b the decarburization is lower because this is a layer more internal and far from the action of the oxygen, and the carbon content is higher. This is clear by observing the white zones in the two images that represent the decarburization phenomenon [44].

4.8 XRD Analysis

The XRD analysis can give important information about the printing process and the heat treatment on the printed pieces. The data can show if the process, and so the result, is correct or not. In particular, the percentage of the phases is fundamental also for the correct behavior and the mechanical response

of the heat-treated materials. Firstly, observing the data from the XRD analysis (Table 3.3) of every sample as-print, it is clear that the results don't change with the variation of printing parameters. There are no big variations that suggest a possible trend, and the percentage of the phases is very similar between the specimens. About 85% of martensite suggests also that the cooling is fast enough. Finally, in Table 3.2 instead, there is the fundamental part with the comparison between the 3D printed material and the same alloy traditionally fabricated both subjected to heat treatment. The analysis shows that there are no variation in the percentage of bainitic ferrite and retained austenite. These results confirm the possibility to obtain a correct microstructure also in the LPBF fabricated material.

4.9 EBSD

The EBSD maps are useful to better understand the growth of the grains and the distribution of the phases into a surface area. The results shown in Figure 3.31 confirm the good fabrication of this alloy through additive manufacturing. The phases are equally distributed on the surface without segregation, with the retained austenite randomly distributed in the ferritic phase. Instead, the grains are oriented without a specific direction as it is possible to see in other papers about LPBF [23–25]. Most grains detected through the EBSD analysis are equiaxial, suggesting that this L-PBF strategy can give a non-directional growth of the grains during the cooling. This could be good for the final mechanical properties because seems that there isn't a predominant direction.

4.10 NEW PARAMETERS

After the complete analysis and the full characterization of the samples, in the subsequent part, the main aim is to enhance these results and find new printing parameters Table 4.2. The choice of these parameters is a fundamental part of the development of the printing process of this alloy. As confirmed in several papers [23,24,26–28,45] the main parameter to consider for better densification of the piece is the Energy Input Density (1.4). There is a trend addicted to this value where the porosity decreases with an increase in Energy Density as shown in Figure 3.10. Therefore, to reach a better quality and an improvement in the properties, it is necessary to act in order to decrease it. Observing the graph in Figure 3.10, it is also visible that there is a change in the trend of the curve, suggesting that after a certain value of energy the porosity starts to increase. So, there is a delimited boundary given by sample 7 which represents the minimum value of porosity detected. However, there is a problem with sample 7, because even if its parameters are the best for the densification, the too high Energy Density causes a surface melt with a leak of dimensional geometry affecting the final result. In light of these considerations, to improve the printing process and the first bunch of printing

parameters, it is reasonable to modify the parameters in order to move Energy Input Density in the range between sample 1, which is the denser without superficial damages, and sample 7 in the graph in Figure 3.10. Once outlined the main value, it is necessary to act on the parameters that affect it such as Laser Power, Scan Speed, Layer Thickness, and Hatch Spacing. Considering that in the first group the last two parameters are equal, the consideration is done on the other two. By modifying the Power and the Speed it is possible to move the Energy Density in the range previously selected, and the second group is chosen in this way, with a couple of parameters that respect this constraint. Using this strategy in the second group, it is possible to better understand the behavior of the alloy and improve the quality by reducing the porosity.

Sample	Power [W]	Distanza Punti	Tempo di Permanenza	Speed [m/s]	Hatch [um]	Layer Dist [um]	Energy Density [J/mm^3]
A	230	30	60	0,5	110	60	69.7
B	235	30	60	0,5	110	60	71.2
C	240	30	60	0,5	110	60	72.7
D	245	33	60	0,55	110	60	67.5
E	250	33	60	0,55	110	60	68.9
F	255	33	60	0,55	110	60	70.2
G	260	33	60	0,55	110	60	71.6
H	270	36	60	0,6	110	60	68.2
I	275	36	60	0,6	110	60	69.4
L	280	48	60	0,8	110	60	53.0
M	190	24	60	0,4	110	60	72.0
N	220	30	60	0,5	110	60	66.7

Table 4.2 Printing Parameters of second group

5 CONCLUSIONS

L-PBF is a technology with a huge potential for present and future applications, allowing for improving the design of the parts and reaching higher performance. The aim of this work was to investigate the possibility to produce a steel bainitic alloy, with medium carbon content and high silicon and manganese content, through additive manufacturing. This focus was not easy because it is difficult to find the perfect printing parameters that can realize the perfect piece. Analyzing every result obtained during the study, it is possible to summarize every data in Table 5.1, making a comparison between the "Conventionally Fabricated Alloy" and the " L-PBF Fabricated Alloy". The *Density* is one of the main results to take into consideration for evaluating the quality and the possibility of the process. the alloy fabricated with AM reaches a value of about 99.5% which is a very good result. It is possible to increase the densification of the specimen aging on the printing parameters, as seen in the graph in figure 3.10. Anyway, a value like this is a great starting point for future improvements. The *Hardness* was evaluated for the "as-print" and compared to the bulk in the same conditions. The value of 490 HV is lower than 670 HV with a big difference. This result can be affected by the presence of pores and defects which decrease the mechanical resistance of the printed material. The hardness changes a lot in every position of the specimen surface due to the presence of imperfections. Moreover, the L-PBF parts can be subjected to heat treatments during the printing process, such as tempering, due to the produced heat by the laser passing on the subsequent layers. In addition, the decarburization can affect the final hardness of the pieces with a martensitic microstructure because the carbon content is fundamental for the mechanical response of the alloy. After the austempering heat treatment, which is an important point for the validation of the possibility of printing this alloy, the obtained microstructures are very similar. L-PBF fabricated alloy shows the classical morphology with plates of ferritic bainite divided by films and blocky retained austenite. The unique difference is due to the presence of a ferrite island randomly distributed. The goodness of the bainitic microstructure is confirmed also by the *Volume Fraction of the Phases.* The EDX maps confirm a correct distribution of the alloy elements in the printed parts with no macro *Composition Differences* in the analyzed surface. Nevertheless, as said before, there are localized zones with lower carbon content. Observing the images of the core of the specimens shows different defects that are the classical present in additive manufacturing.

	Conventionally Fabricated Alloy	**L-PBF Fabricated Alloy**
Density	100%	~99,5%
Hardness	670 HV	~490 HV
Bainitic Microstructure	- Yes - Austempering 325°C, 3h	- Yes, with the island of ferrite randomly distributed - Austempering 325°C, 3h
Composition Differences	No	No, but there is a slight decarburization
Volume Fraction of Phases	V_b: 75±3 % V_γ: 25±3 %	V_b: 79±3 % V_γ: 21±3 %
Geometrical Design	Geometrical constraints due to the traditional production	- No geometrical constraints and design freedom. - Respected geometries.
Defects	No particular defects	- Pores - Lack of fusion - Cracks

Table 5.1 Comparison between the L-PBF fabricated and the Conventionally fabricated alloy.

In conclusion, analyzing every result and every aspect of the printed material it is possible to assert that the bainitic alloy with this composition is suitable for printing through additive manufacturing techniques, in particular with L-PBF. This is a very significant point to continue to improve this fabrication way, in order to reach a higher level of quality. There are a lot of aspects to take into consideration, and they require attention and improvement to achieve the perfect result. Additive manufacturing is one of the frontiers of modern engineering. It is the way to improve performance, geometries, and final use of every kind of component, allowing the human being to overtake the actual limits and reach increasingly distant destinations.

Acknowledgments

I want to thank all the people who have been close to me and who have supported and endured me during my graduation journey. In particular, I want to thank my family, my friends, and the people who love me because they have always believed in me, pushing me to improve, and never giving up. Furthermore, I would like to thank Mattia and Arshad, my two co-supervisors, Luca, and all the guys from the laboratory of the University of Padua who are always present and ready to help me.

Bibliography

1. Bhadeshia, H.K.D.H. *Bainite in Steels: Theory and Practice*; Maney Publishing, 2006; Vol. 19; ISBN 9781909662742.

2. Bhadeshia, H.K.D.H.; Edmonds, D.V. The Mechanism of Bainite Transformation in Steels. *Acta Metallurgica* 1980, *28*, 1265–1273.

3. Garcia-Mateo, C.; Caballero, F.G. Understanding the Mechanical Properties of Nanostructured Bainite. *Handbook of Mechanical Nanostructuring* **2015**, *1*, 35–65, doi:10.1002/9783527674947.ch3.

4. Caballero, F.G.; Bhadeshia, H.K.D.H.; Mawella, K.J.A.; Jones, D.G.; Brown, P. Very Strong Low Temperature Bainite. *Materials Science and Technology* **2002**, *18*, 279–284, doi:10.1179/026708301225000725.

5. Bhadeshia, H.K.D.H.D.V.E. Bainite in Silicon Steels: New Composition-Property Approach Part 2. *Metal Science* 1983, *17*, 420–425.

6. Eres-Castellanos, A.; Morales-Rivas, L.; Latz, A.; Caballero, F.G.; Garcia-Mateo, C. Effect of Ausforming on the Anisotropy of Low Temperature Bainitic Transformation. *Mater Charact* **2018**, *145*, 371–380, doi:10.1016/j.matchar.2018.08.062.

7. Eres-Castellanos, A.; Toda-Caraballo, I.; Latz, A.; Caballero, F.G.; Garcia-Mateo, C. An Integrated-Model for Austenite Yield Strength Considering the Influence of Temperature and Strain Rate in Lean Steels. *Mater Des* **2020**, *188*, doi:10.1016/j.matdes.2019.108435.

8. Paolucci, G.M. Lezioni Di Metallurgia per La Laurea in Ingegneria Meccanica Vol.2.

9. Caballero, F.G.; Miller, M.K.; Babu, S.S.; Garcia-Mateo, C. Atomic Scale Observations of Bainite Transformation in a High Carbon High Silicon Steel. *Acta Mater* **2007**, *55*, 381–390, doi:10.1016/j.actamat.2006.08.033.

10. Bhadeshia, H.K.D.H.; Load, M.; Svensson, L. Silicon-Rich Bainitic Steel Welds. *Transactions of the JWRI* **2003**, 43–52.

11. Caballero, F.G.; Garcıa-Mateo, C. The Role of Retained Austenite on Tensile Properties of Steels with Bainitic Microstructures. *Mater Trans* **2005**, *46*, 1839–1846.

12. Kyung Sung, H.; Ho Lee, D.; Yong Shin, S.; Lee, S.; Yong Yoo, J.; Hwang, B. Effect of Finish Cooling Temperature on Microstructure and Mechanical Properties of High-Strength Bainitic Steels Containing Cr, Mo, and B. *Materials Science and Engineering A* **2015**, *624*, 14–22, doi:10.1016/j.msea.2014.11.035.

13. Morales-Rivas, L.; Garcia-Mateo, C.; Sourmail, T.; Kuntz, M.; Rementeria, R.; Caballero, F.G. Ductility of Nanostructured Bainite. *Metals (Basel)* **2016**, *6*, doi:10.3390/met6120302.

14. San-Martin, D.; Kuntz, M.; Caballero, F.G.; Garcia-Mateo, C. A New Systematic Approach Based on Dilatometric Analysis to Track Bainite Transformation Kinetics and the Influence of the Prior Austenite Grain Size. *Metals (Basel)* **2021**, *11*, 1–13, doi:10.3390/met11020324.

15. Hu, F.; Hodgson, P.D.; Wu, K.M. Acceleration of the Super Bainite Transformation through a Coarse Austenite Grain Size. *Mater Lett* **2014**, *122*, 240–243, doi:10.1016/j.matlet.2014.02.051.

16. Matsuzaki, A.; Bhadeshia, H.K.D.H. Effect of Austenite Grain Size and Bainite Morphology on Overall Kinetics of Bainite Transformation in Steels. *Materials Science and Technology* **1999**, *15*, 518–522, doi:10.1179/026708399101506210.

17. Garcıa-Mateo, C.; Caballero, F.G. Ultra-High–Strength Bainitic Steels. **2005**, *45*, 1736–1740.

18. Zenji Nishiyama Martensitic Transformation. **1978**.

19. Leary, M. Powder Bed Fusion. In *Design for Additive Manufacturing*; Elsevier, 2020; pp. 295–319.

20. Spears, T.G.; Gold, S.A. In-Process Sensing in Selective Laser Melting (SLM) Additive Manufacturing. *Integr Mater Manuf Innov* 2016, *5*, 16–40.

21. Prevorovsky, Z.; Krofta, J.; Kober, J. *NDT in Additive Manufacturing of Metals*; 2017; Vol. 2017-Octob; ISBN 9788087012635.

22. Linkan Bian, N.S. and J.M.U. *Laser-Based Additive Manufacturing of Metal Parts: Modeling, Optimization, and Control of Mechanical Properties*; 2018; ISBN 9781498739986.

23. Dilip, J.J.S.; Ram, G.D.J.; Starr, T.L.; Stucker, B. Selective Laser Melting of HY100 Steel: Process Parameters, Microstructure and Mechanical Properties. *Addit Manuf* **2017**, *13*, 49–60, doi:10.1016/j.addma.2016.11.003.

24. Garibaldi, M.; Ashcroft, I.; Simonelli, M.; Hague, R. Metallurgy of High-Silicon Steel Parts Produced Using Selective Laser Melting. *Acta Mater* **2016**, *110*, 207–216, doi:10.1016/j.actamat.2016.03.037.

25. Lemke, J.N.; Simonelli, M.; Garibaldi, M.; Ashcroft, I.; Hague, R.; Vedani, M.; Wildman, R.; Tuck, C. Calorimetric Study and Microstructure Analysis of the Order-Disorder Phase Transformation in Silicon Steel Built by SLM. *J Alloys Compd* **2017**, *722*, 293–301, doi:10.1016/j.jallcom.2017.06.085.

26. Garibaldi, M.; Ashcroft, I.; Hillier, N.; Harmon, S.A.C.; Hague, R. Relationship between Laser Energy Input, Microstructures and Magnetic Properties of Selective Laser Melted Fe-6.9%wt Si Soft Magnets. *Mater Charact* **2018**, *143*, 144–151, doi:10.1016/j.matchar.2018.01.016.

27. Shen, X.; Meng, F.; Lau, K.B.; Wang, P.; Lee, C.H.T. Texture and Microstructure Characterizations of Fe-3.5wt%Si Soft Magnetic Alloy Fabricated via Laser Powder Bed Fusion. *Mater Charact* **2022**, *189*, doi:10.1016/j.matchar.2022.112012.

28. Chen, H.; Gu, D.; Dai, D.; Ma, C.; Xia, M. Microstructure and Composition Homogeneity, Tensile Property, and Underlying Thermal Physical Mechanism of Selective Laser Melting Tool Steel Parts. *Materials Science and Engineering A* **2017**, *682*, 279–289, doi:10.1016/j.msea.2016.11.047.

29. Wimpenny, D.I.; Pandey, P.M.; Jyothish Kumar, L. *Advances in 3D Printing & Additive Manufacturing Technologies*; 2016; ISBN 9789811008122.

30. Tolosa, I.; Garciandía, F.; Zubiri, F.; Zapirain, F.; Esnaola, A. Study of Mechanical Properties of AISI 316 Stainless Steel Processed by “Selective Laser Melting”, Following Different

Manufacturing Strategies. *International Journal of Advanced Manufacturing Technology* **2010**, *51*, 639–647, doi:10.1007/s00170-010-2631-5.

31. Zhao, X.; Song, B.; Zhang, Y.; Zhu, X.; Wei, Q.; Shi, Y. Decarburization of Stainless Steel during Selective Laser Melting and Its Influence on Young's Modulus, Hardness and Tensile Strength. *Materials Science and Engineering A* **2015**, *647*, 58–61, doi:10.1016/j.msea.2015.08.061.

32. Abramoff, M.D.; Magalhanes, P.J.; Ram, S.J. Image Processing with ImageJ. *Biophotonics International*.

33. *ITC Data Analysis in Origin ® Tutorial Guide Using Origin ® Scientific Plotting Software to Analyze Calorimetric Data from All MicroCal Isothermal Titration Calorimeters*;

34. Titus, D.; James Jebaseelan Samuel, E.; Roopan, S.M. Nanoparticle Characterization Techniques. In *Green Synthesis, Characterization and Applications of Nanoparticles*; Elsevier, 2019; pp. 303–319.

35. Gupta, S.; Omar, T.; Muzzio, F.J. SEM/EDX and Raman Chemical Imaging of Pharmaceutical Tablets: A Comparison of Tablet Surface Preparation and Analysis Methods. *Int J Pharm* **2022**, *611*, doi:10.1016/j.ijpharm.2021.121331.

36. Castro, A. *Proprietà Fisiche Della Materia*; Libreriauniversitaria.it, 2009; ISBN 9788862920087.

37. Caballero, F.G.; Miller, M.K.; Garcia-Mateo, C. Carbon Supersaturation of Ferrite in a Nanocrystalline Bainitic Steel. *Acta Mater* **2010**, *58*, 2338–2343, doi:10.1016/j.actamat.2009.12.020.

38. Cherry, J.A.; Davies, H.M.; Mehmood, S.; Lavery, N.P.; Brown, S.G.R.; Sienz, J. Investigation into the Effect of Process Parameters on Microstructural and Physical Properties of 316L Stainless Steel Parts by Selective Laser Melting. *International Journal of Advanced Manufacturing Technology* **2015**, *76*, 869–879, doi:10.1007/s00170-014-6297-2.

39. Yazdanpanah, A.; Lago, M.; Gennari, C.; Dabalà, M. Stress Corrosion Cracking Probability of Selective Laser Melted 316l Austenitic Stainless Steel under the Effect of Grinding Induced Residual Stresses. *Metals (Basel)* **2021**, *11*, 1–20, doi:10.3390/met11020327.

40. Yazdanpanah, A.; Franceschi, M.; Bergamo, G.; Bonesso, M.; Dabalà, M. On the Exceptional Stress Corrosion Cracking Susceptibility of Selective Laser Melted 316L Stainless Steel under the Individual Effect of Surface Residual Stresses. *Eng Fail Anal* **2022**, *136*, doi:10.1016/j.engfailanal.2022.106192.

41. Zhao, X.; Song, B.; Zhang, Y.; Zhu, X.; Wei, Q.; Shi, Y. Decarburization of Stainless Steel during Selective Laser Melting and Its Influence on Young's Modulus, Hardness and Tensile Strength. *Materials Science and Engineering A* **2015**, *647*, 58–61, doi:10.1016/j.msea.2015.08.061.

42. Hu, Z.; Zhu, H.; Zhang, H.; Zeng, X. Experimental Investigation on Selective Laser Melting of 17-4PH Stainless Steel. *Opt Laser Technol* **2017**, *87*, 17–25, doi:10.1016/j.optlastec.2016.07.012.

43. Maharjan, N.; Zhou, W.; Zhou, Y.; Wu, N. Decarburization during Laser Surface Processing of Steel. *Appl Phys A Mater Sci Process* **2018**, *124*, doi:10.1007/s00339-018-2104-5.

44. Cornell, R. and B.H.K.D.H. Decarburization of Steel. In; 2013.

45. Kang, N.; el Mansori, M.; Guittonneau, F.; Liao, H.; Fu, Y.; Aubry, E. Controllable Mesostructure, Magnetic Properties of Soft Magnetic Fe-Ni-Si by Using Selective Laser Melting from Nickel Coated High Silicon Steel Powder. *Appl Surf Sci* **2018**, *455*, 736–741, doi:10.1016/j.apsusc.2018.06.045.